SYNTHESIS OF SILVER DOPED ZINC OXIDE NANOPARTICLES USING *Citrus reticulata* PEEL EXTRACT AND THEIR CHARACTERIZATION FOR POTENTIAL APPLICATION IN SOLAR CELLS

Joan Jepngetich

A Thesis Submitted in Partial Fulfillment of the Requirements for the Degree of Master of Science in Chemistry of Murang'a University of Technology

July, 2025

DECLARATION

Student Declaration

I hereby declare that this Thesis is my original work and to the best of my knowledge has not been presented for a degree award in this or any other university. I understand what plagiarism is and I am aware of the University's policy in this regard. I understand that any false claim in respect of this work shall result in disciplinary action in accordance with the University Anti-Plagiarism Policy.

_____ _____

Joan Jepngetich Date

AS401/5817/2022

Supervisors' Approval

The undersigned certify that they have read and hereby recommended for acceptance of Murang'a University of Technology a thesis entitled "**Synthesis of Silver Doped Zinc Oxide Nanoparticles using *Citrus reticulata* Peel Extract and their Characterization for Potential Application in Solar Cells".**

_____ _____

Dr. Peter Waithaka Njoroge, Date

Department of Physical and Biological Science,

Murang'a University of Technology.

_____ _____

Prof. Sylvia Awino Opiyo, Date

Department of Physical and Biological Sciences,

Murang'a University of Technology.

_____ _____

Dr. Sharon Kiprotich, Date

Department of Physical and Biological Sciences,

Murang'a University of Technology.

DEDICATION

This research is dedicated to Eusilah Jepchirchir, Monica Maruu, and Justus Kipyego for their moral support, encouragement and inspiration. To my siblings, friends and classmates who have been my pillars of strength, companionship and motivation throughout this journey. This thesis is a statement of your unwavering support.

ACKNOWLEDGEMENT

To God am so grateful for the strength, knowledge, protection and providence throughout my studies. Without Him all this would not have been possible.

To my supervisors Dr. Peter Waithaka, Prof. Sylvia Opiyo and Dr. Sharon Kiprotich. I extend my sincerest acknowledgement for your supervision, motivation, guidance and support throughout my studies. I am eternally grateful for your enormous support. May God bless you all.

This project was successfully supported by the SG-NAPI award supported by the German Ministry of Education and Research, BMBF through UNESCO-TWAS. I am forever grateful for their financial support throughout my studies.

I am thankful to the Department of Physical and Biological Science at Murang'a University of Technology. I am grateful for the opportunity and granting me access to various laboratory equipment and technical assistance while working in the laboratory. To my research colleagues James, Bethwel, Collins, Simon, Vitalis, Nancy, Nimrod and Ayabei, I am thankful for your positive critics and support during my study period.

To my parents Justus, Eusilah and Monica, and my siblings Judy, Joyce, Jelafine, Jael, Shaila, Ryan, Noel and Roy, thank you for your support, prayers and encouragements. Your support and financial aid have been the driving force in my studies, and I am eternally grateful for that.

Finally, I will like to thank everyone who accommodated me, my extended family for their encouragement and prayers. Lastly, but not least I would like to thank myself for giving my best and being disciplined on this academic journey. Thank you all.

ABSTRACT

Nanoparticles (NPs) are materials ranging in size between 1-100 nm. The NPs are used in solar cells due to their unique properties. Solar cells have become an alternative lead to green energy but their application is limited by factors such as cost, efficiency and availability. In this study, silver-doped zinc oxide (Ag-ZnO) NPs were synthesized using *Citrus reticulata* peel extract. Effects of silver doping concentration on the structural and optical properties of ZnONPs were studied by varying the concentration of silver dopant at (0.1, 0.25, 0.5, 0.75, 1.0, 1.5, and 2.0 mol %). Effects of growth temperature on the structural and optical properties of ZnONPs was studied by varying the growth temperature of NPs at (25, 30, 40, 50, 60 and 70 ℃). The NPs were prepared via green synthesis method. The prepared and annealed Ag-ZnONPs were characterized using X-ray diffraction (XRD), Ultra-Violet visible (UV-vis), Fourier transmission infra-red (FT-IR) spectroscopy and photoluminescence spectroscopy (PL). The XRD pattern of *Citrus reticulata* capped ZnONPs displayed hexagonal wurtzite structure. The Debye Scherrer formula was used to calculate the crystal size of nanoparticles. All nanoparticles formed were in the range of 8-14 nm. The 0.1% Ag-ZnO had the highest intensity in XRD pattern at plane peak (101). The crystal size of nanoparticles ranged from 15.29-19.87 nm. At 0.5% Ag-ZnONPs, the XRD peak shifted to the higher 2 theta degrees compared to other doping concentrations. At varying growth temperature, the crystal size range from 15.54-17.87 nm. The FT-IR spectra of *Citrus reticulata* capped ZnO and Ag-ZnO nanoparticles showed absorption in both functional group and fingerprint regions. The stretching vibration of Zn-O was observed between 470-420 cm^{-1}. When concentration of Ag dopant was varied, the stretching vibration of metal oxide was observed 459-470 cm^{-1}. The PL results of the samples showed UV emission peaks at 350 to 450 nm. Increase in Ag concentration shift emission to a higher wavelength. The bandgap energies of nanoparticles were estimated using Tauc's plot. The bandgap energy increased from 3.00 to 3.29 when capped. When doped with different mol % of silver, the bandgap energies increase at lower concentrations from 3.30 for pure ZnONPs to 3.69 and 3.61 for 0.25 and 0.5 Ag-ZnONPs mol% respectively. At higher concentrations, the bandgap energy decreased to 3.03, 3.13, 3.10 and 3.17 eV for 2.0, 1.5, 1.0 and 0.75 mol% respectively. The bandgap energy decreased from 3.03 eV at 25 and 40 ℃ to 2.94 eV at 30, 60, and 70 ℃ and 2.85 eV at 50 ℃. The Ag-ZnONPs were successfully synthesized by the green synthesis method, and doping the ZnO with higher mol % of silver at a growth temperature of 50 ℃ presents good crystallization, good optical and luminescence properties that can be tested as a photoanode component in dye sensitized solar cells.

TABLE OF CONTENTS

DECLARATION ..... **ii**
DEDICATION ..... **iii**
ACKNOWLEDGEMENT ..... **iv**
ABSTRACT ..... **v**
LIST OF TABLES ..... **ix**
LIST OF FIGURES ..... **x**
ACRONYMS AND ABBREVIATIONS ..... **xii**
DEFINITION OF OPERATIONAL TERMS ..... **xiii**
CHAPTER ONE: INTRODUCTION **1**
1.1 Background Information 1
1.2 Statement of Problem 3
1.3 Significance of the Study 4
1.4. Objectives of the Study 4
1.4.1 General objectives of the Study 4
1.4.2 Specific Objectives 4
1.5 Research Questions 4
1.6 Scope and Limitation 5
1.7 Contributions of the Thesis 5
1.8 Organization of the Thesis 6
CHAPTER TWO: LITERATURE REVIEW **7**
2.1 General Introduction 7
2.2 Solar Cells 7
2.3 Electrical Properties of Solar Cells 9
2.4 Metal Oxides Nanoparticles and their Application in Solar Cells 10
2.5 Types of Dopants 11
2.6 Effects of Capping Agents 13
2.7. Structural Properties of Metal Oxides Nanoparticles 13
2.7.1 Nanowires 13
2.7.2 Nanotubes 13
2.7.3 Nanocones 13
2.7.4 Nanopillars 14
2.8 Optical Properties of Nanoparticles 15
2.9. General Properties of Zinc Oxide Nanoparticles 16
2.9.1 Electronic Properties 16
2.9.2 Crystal Structure 17
2.10. Doped Zinc Oxide Nanoparticles 17
2.11. Synthesis of Nanoparticles 20

2.11.1 Chemical Precipitation....20
2.11.2 Sol gel techniques....21
2.11.3 Biological/green Synthesis Method....21
2.12. Analytical Techniques used to Characterize Nanoparticles....22
2.12.1 Fourier Transform Infrared Spectroscopy....23
2.12.2 Ultra Violet Visible Spectroscopy....24
2.12.3 Photoluminescence Spectroscopy....25
2.12.4 The X-ray Diffraction....26
2.12.5 Microscopy Techniques....28
2.13 Summary....28
CHAPTER THREE: MATERIALS AND METHODS....30
3.1 Introduction....30
3.2 Materials....30
3.3 Preparation of *Citrus reticulata* peel extract....30
3.4 Synthesis of Zinc oxide (ZnO) nanoparticles using *Citrus reticulata* peel extract....30
3.5 Synthesis of Zinc oxide nanoparticles without *Citrus reticulata* peel extract....31
3.6 Synthesis of *Citrus reticulata* capped silver-doped zinc oxide nanoparticles....31
3.7 Synthesis of silver-doped zinc oxide nanoparticles without *Citrus reticulata*....31
3.8 Synthesis of different concentration of silver mol % doping concentration on the optical and structural properties of ZnO nanoparticles....32
3.9 Synthesis *Citrus reticulata* capped silver-doped zinc oxide nanoparticles at different growth temperature on the structural and optical properties of Ag-ZnO nanoparticles....32
3.10. Characterization of the synthesized nanoparticles....32
3.10.1 UV-Vis characterization....32
3.10.2 FT-IR Characterization....33
3.10.3 XRD Characterization....33
3.10.4 Morphological and EDS Characterization....33
3.10.5 PL Characterization....33
3.11 Validation....34
3.12 Research design....34
3.13 Summary....34
CHAPTER FOUR: RESULTS AND DISCUSSION....36
4.1 Introduction....36
4.2. Effects of *Citrus reticulata* peel extract on silver- doped zinc oxide nanoparticles....36
4.2.1 The FT-IR Analysis....36

4.2.2 The XRD analysis 38
4.2.3 Photoluminescence spectroscopy 45
4.2.4 UV-Vis Analysis 46
4.2.5 Morphology 49
4.2.6 Elemental and chemical analysis 50
4.3 Effects of Ag doping concentrations on structural and optical properties of *citrus reticulata* capped ZnO nanoparticles 51
4.3.1 The X-ray diffractions (XRD) analysis 51
4.3.2 The FT-IR analysis 58
4.3.3 Photoluminescence spectroscopy 59
4.3.4 Optical Properties 61
4.3.5 Morphology 63
4.4. Effects of growth temperature on *Citrus reticulata* capped Ag-ZnO nanoparticles 65
4.4.1 The XRD Analysis 65
4.4.2 FT-IR analysis 70
4.4.3 Photoluminescence spectroscopy 71
4.4.4 Optical properties 72
4.4.5 Morphological analysis 73
4.5 Summary 76
CHAPTER FIVE: CONCLUSION AND RECOMMENDATIONS 78
5.1 Conclusion 78
5.2. Recommendations 80
5.2.1 Recommendation for Policy 80
5.2.2 Recommendation for Future 80
REFERENCES 82
APPENDICES 99

LIST OF TABLES

Table 2.1: Synthesis techniques and morphology of non-metal doped ZnO 12
Table 2.2: Effects of pH on the band gap, particle size and crystal size of ZnO nanoparticles..... 14
Table 2.3: Effects of annealing temperature on structural size, band gap and crystal size. 15
Table 4.1: Calculated d-spacing and the standard JCPDS d-spacing of capped and uncapped ZnO with their FWHM. 40
Table 4.2: Calculated d-spacing and FWHM (Å) of Ag-ZnO nanoparticles. 41
Table 4.3: Calculated crystal sizes (D) of uncapped ZnO and capped ZnO & Ag-ZnO nanoparticles 41
Table 4.4: Dislocation density ($\times 10^{-3}$ nm^{-2}) of uncapped ZnO and capped ZnO & Ag-ZnO nanoparticles 44
Table 4.5: Calculated strain of uncapped Ag-ZnO nanoparticles 44
Table 4.6: Effects of different concentration of silver dopant on the d-spacing and lattice parameters a and c. 53
Table 4.7: Calculated crystal size (D) and obtained FWHM of varying mol % of silver dopant in Ag-ZnONPs. 54
Table 4.8: Variation of strain with concentration from W-H method 57
Table 4.9 Elemental analysis of 0.25 % Ag-ZnONPs 64
Table 4.10 Elemental analysis of 1.5 % Ag-ZnONPs 64
Table 4.11 Elemental analysis of 2.0 % Ag-ZnONPs 64
Table 4.12: Summarized calculated lattice parameters, crystal size and FWHM 68
Table 4.13 Elemental analysis of Ag-ZnONPs synthesized at a growth temperature of 30 ℃. 75
Table 4.14 Elemental analysis of Ag-ZnONPs synthesized at a growth temperature of 50 ℃. 75
Table 4.15 Elemental analysis of Ag-ZnONPs synthesized at a growth temperature of 30 ℃. 75

LIST OF FIGURES

Figure 1.1: Schematic diagram of photovoltaic solar cell 2
Figure 2.1: Structure of solar cell and effect of light 8
Figure 2.2: Schematic diagram of insulators, semiconductors and metals 8
Figure 2.3: Organic solar cell curve of current-voltage 9
Figure 2.4: Emission spectrum at (a) 330nm (b) 368nm and (c) 433 nm of ZnS 16
Figure 2.5: (a-e) SEM images of Ce-ZnO at different concentration of Ce loaded: (a) ZnO NPs, (b) 2.02 %, (c) 3.24 %, (d) 6.24 % and (e) 8.24 % 18
Figure 2.6: The XRD pattern of Ag-ZnO 19
Figure 2.7: Visible PL band for the ZnONPs with: (a) undoped (b) 0.5%, (c) 1.0%, and (d) 2.0% of Ag 20
Figure 2.8: Stages of sol-gel synthesis 21
Figure 2.9: Shimadzu IR spirit FT-IR model 23
Figure 2.10: Evolution one plus UV-Vis spectroscopy 24
Figure 2.11: SP-LF97 model PL spectroscopy 26
Figure 2.12: The ARL EQUINOX X-ray diffractometer 26
Figure 2.13: Geometrical condition for diffraction from lattice planes 27
Figure 3.1: The Ag-ZnONPs synthesized using green synthesis method 34
Figure 4.1: The FT-IR spectra of Plant extracts capped ZnONPs and uncapped ZnONPs nanoparticles 37
Figure 4.2: FT-IR spectra of ZnO and Ag-ZnO at (a) 400-4000 cm^{-1} and (b) 400-650 cm^{-1} 37
Figure 4.3:(a) XRD pattern of capped and uncapped ZnONPs and (b)peak (101) of capped and uncapped ZnONPs 38
Figure 4.4: The XRD pattern of capped and uncapped Ag-ZnO nanoparticles 39
Figure 4.5: The XRD pattern of annealed pure and Ag-ZnONPs at 450℃ 42
Figure 4.6: The XRD pattern of peak (101) 43
Figure 4.7: The PL spectra of pure and capped ZnO and Ag-ZnO nanoparticles 45
Figure 4.8: UV-vis spectra of pure and capped ZnO nanoparticles 46
Figure 4.9: Tauc's plot of pure and capped Ag-ZnO nanoparticles 47
Figure 4.10: Refractive index of capped and uncapped ZnO and Ag-ZnO nanoparticles 48
Figure 4.11: (a) Real and (b) Imaginary dielectric constant 49
Figure 4.12:The SEM images of pure and capped ZnONPs 50
Figure 4.13: SEM images of capped and uncapped Ag-ZnONPs 50
Figure 4.14: EDS spectra of capped and uncapped ZnO nanoparticles 51
Figure 4.15: XRD pattern of different mol % concentration Ag-doped ZnONPs 52
Figure 4.16: Variation of FWHM and crystal size of pure and doped Ag-ZnONPs ..55

Figure 4.17: (a) Enlargement image of diffraction plane [101] for pure ZnO and doped Ag- 55
Figure 4.18: Plots of $\beta_{hkl\cos\theta}$ versus 4sinθ for (a) 0.1% and (b) 0.25% Ag-ZnO 57
Figure 4.19: Plot showing the trend of crystal size (D) and strain of Ag-ZnONPs ... 58
Figure 4.20: FT-IR spectra of annealed and as prepared samples 58
Figure 4.21: PL emission spectra of varying concentration of Ag-ZnO nanoparticles 60
Figure 4.22: The PL emission spectra of Ag-ZnO at varying Ag % mol 61
Figure 4.23: UV-vis spectra of pure and doped Ag-ZnONPs 61
Figure 4.24: Tauc's plot showing estimated bandgap energies of pure and doped Ag-ZnONPs 62
Figure 4.25: SEM images of (a) 0.25, (b) 1.5 and (c) 2.0% Ag-ZnONPs 63
Figure 4.26: EDS spectra of 0.25, 1.5 and 2.0 Ag-ZnONPs 64
Figure 4.27: EDS layered images of 0.25, 1.5 and 2.0 % Ag-ZnONPs 65
Figure 4.28: XRD pattern of Ag-ZnO prepared at different temperatures 66
Figure 4.29: Enlarged image of diffraction plane [101] for capped Ag-ZnONPs prepared at different temperatures 66
Figure 4.30: Variation of crystal size with FWHM at a temperatures 69
Figure 4.31: Plot of crystal size and strain of capped Ag-ZnO nanoparticles prepared at different temperature 70
Figure 4.32: FT-IR spectra of Ag-ZnONPs at a growth temperature of (a) 30, 40, 50, 60, and 65 ℃ and (b) 25 and 70 ℃ 70
Figure 4.33: (a) PL spectra of Ag-ZnONPs (b) variation of PL FWHM and intensity at varying growth temperature 71
Figure 4.34: UV-vis spectra of Ag-ZnONPs prepared at different growth temperatures 72
Figure 4.35: Tauc's plot $(\alpha h\nu)^2$ versus Energy (eV) of Ag-ZnONPs at different growth temperatures 25, 30, 40, 50, 60 and 70 ℃ 73
Figure 4.36 SEM images of Ag-ZnONPS synthesized at a growth temperature of (a) 30 (b) 50 and (c) 70 ℃ 74
Figure 4.37: EDS spectra of synthesized Ag-ZnONPs at different growth temperature 75
Figure 4.38 EDS images of Ag-ZnONPs synthesized at different growth temperatures 76

ACRONYMS AND ABBREVIATIONS

3D	Three dimensional
Ag-ZnO	Silver doped zinc oxide
CB	Conduction band
CIS	Copper indium diselenide
DOPO	Dioctylphosphine oxide
DSSC	Dye sensitized solar cell
EDS	Energy dispersive spectroscopy
FT-IR	Fourier transform infrared spectroscopy
FWHM	Full width at half maximum
GHG	Green-house gases
ICDD	International centre for diffraction data
IEA	International energy agency
JCPDS	Joint committee on powder on powder diffraction standards
LED	Light emitting diodes
LSPR	Localized surface plasmon resonance
MONPs	Metal oxide nanoparticles
MPP	Maximum power point
NIR	Near infrared spectroscopy
NIRLSP	Near infrared localized surface plasmon
NPs	Nanoparticles
pH	Potential of hydrogen
PL	Photoluminescence
RPM	Revolution per minute
SEM	Scanning electron microscope
TEM	Transmission electron microscope
TOPO	Trioctylphosphine oxide
UV-Vis	Ultra violet visible spectroscopy
VB	Valence band
XRD	X-ray diffraction

DEFINITION OF OPERATIONAL TERMS

Annealing - The use of heat to treat material or compound at a high temperature and slowly cooled at a control rate to remove stress, or to alter its structural, chemical and physical properties of material.

Bandgap energy – This is the distance in energy level separating the valence band and the conduction band in metal, semiconductors and insulators.

Capping agents – they are molecules that inhibit overgrowth of nanoparticles and prevent coagulation during colloidal synthesis.

Characterize – The application of scientific methods such as microscopy to interpret the composition of material or compound.

Crystal size – is the physical dimension of individual crystal in material. It is used to describe the distribution of crystal in the material, and to analyze the physical, chemical and mechanical parameters of crystalline substances.

Doping – refers to the incorporation of foreign material into the lattice crystal of the host material to modify its structural, electrical, optical and morphological properties.

Photoanode – is a component of a solar cell responsible for the production of electrical energy from light energy.

Synthesis – It is a process of obtaining a compound, material or a substance by combining individual elements or molecules in a systematic manner.

CHAPTER ONE
INTRODUCTION

1.1 Background Information

Silicon solar cells use the sun for generation of energy and in the last decade they have received considerable attention. Silicon solar cells use solar energy to generate electricity. Despite using solar they are expensive and less efficient compared to fossil fuels. Global warming occurs as a result of emission of harmful gases like CO_2 from fossil fuel to atmosphere (Ebhota & Jen, 2020). Therefore, there is need to improve on solar cells efficiency and reduce the cost to reduce the use of fossil fuels is advocated.

When the amount of silicon used in the manufacture of solar cells is decreased, the solar cell cost will also decrease. Thin silicon wafers produced solar cells that have an efficiency of up to 26.81% (Lin *et al.*, 2023). When several solar cells are arranged in series and parallel such that they can produce a certain amount of power output referred to as solar panels. The main components of photovoltaic cells (PV) are solar panels, inverters and supercapacitors. The solar panels use the PV mechanism to produce electricity by absorbing then transforming the photon energy; supercapacitors are used on sunny days to deliver additional energy; and inverters are used to transform the generated direct current (DC) to alternating current (AC) mainly for domestic used (Arefeen & Dallas, 2021).

The main component of photovoltaic solar cell is the solar panel; this is where the electrical features such as voltage, resistance and current are located (Al-Ezzi & Ansari, 2022). Figure 1 shows how the PV operates. From the diagram when the photons of light strike the cell p-n junction, they generate the charge carriers. The photon energy given by ($E=hv$) is higher than the bandgap energy (E_g) of the doped semiconducting materials. Therefore the energy is used to move the electron from the valence band (E_v) to the conducting band (E_c), thus leaving a void in the valence band. Furthermore, the excess photon energy ($hv-hv_o$) gives the electron or the hole kinetic energy. The hv_o is the minimum energy required to generate the electron-hole. Any excess energy is released as heat (Zhang, 2014). The electrical current is extracted once the circuit is closed on an external load.

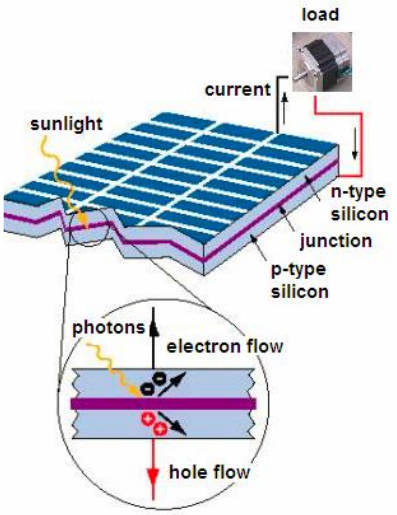


Figure 1.1: Schematic diagram of photovoltaic solar cell

Source: (Al-Ezzi & Ansari, 2022)

Scholars have tried to use nanotechnology to improve these demerits but solar cell efficiency remains low (Banin *et al.,* 2020). In solar cells, nanoparticles have the ability to reflect light many times within the device, enhancing photocurrent (Wang *et al.,* 2021). The unique characteristics of nanoparticles for example small size allow for innovative approach on light absorption to electron transfer in solar cell design (Yang *et al.,* 2024). The NPs are categorized into metals and metal oxides. The common metallic nanoparticles that have been successfully synthesized are silver, gold, copper, platinum, palladium, iron and nickel (Hasan, 2015).

Metal oxides with nanostructures include NiO, CuO, TiO_2 and ZnO. These metal oxides have potential application in the production of energy since they have wide and thin band gap based p and n type (Iqbal *et al*., 2019). The ZnO is a binary compound used in solar cell application as a result of its high electron affinity and excellent electron mobility (Wibowo *et al.,* 2020).

Pure ZnONP cannot be used as photocatalytic material since it does not meet the practical requirements; activating ZnO catalyst leads to a decrease in efficiency in the visible and near infrared thus necessitating high UV light (Yıldırım *et al.,* 2013). The photocatalytic activity of ZnONP is affected by rapid recombination of photo generated electron pair (Lee *et al.*, 2016).

To overcome these problems semiconductor combination is used to enhance the photocatalytic activity, transitional metal doping or noble metal deposition (Berehe *et al*., 2023). Dopants are expected to occupy the interstitial site of ZnO.

1.2 Statement of Problem

About 70% of the global carbon dioxide emission is caused by combustion of fossil fuels in urban mainly in transport and industry (Desa *et al*., 2014). Urbanization is expected to extend across all regions globally by 2050 with Africa and Asia leading compared to other regions. The projection of urbanization by 2050 in Africa is 56% while Asia is 64% (Desa, 2014). Energy production is the dominating source of CO_2 and other green house gases (GHG). According to global anthropogenic emissions, 70% of all emissions of greenhouse gases originate from the energy sector, with carbon dioxide emission from burning fossil fuels contributing the most (Ebhota & Jen, 2020). United Nation have pushed for clean energy, and urban energy is expected to emit low to zero CO_2 (Hepburn et al., 2021).

Alternative sources of energy will reduce consumption of fossil fuels, resulting in a decrease in the amount of GHG released into the atmosphere. Solar energy is one alternative source of green energy that can be used to replace fossil fuels. To harness the solar energy the solar cell is a requirement and its efficiency is paramount. Solar cells have low efficiency and can be improved using nanoparticles. Properties of nanoparticles used in solar cells are influenced by various components such as the synthetic method, pH, crystal shape and size of the nanoparticle synthesized. Green synthesis of nanoparticles for use in solar cell application is an alternative that is safe and utilizes materials that are not treated before being release to the environment. Nanoparticles have excellent optical properties which have been employed in solar cells due to their ability to convert the sun rays to photo current (Y. Chen et al., 2021). Doping is used to improve properties of MONP such as optical properties. When metal is used as dopant it lowers the activation energy thus reducing the working temperature and improving the sensing efficiency(Yoon *et al*., 2022). The concentration of dopant and temperature variation are key factors that influence the efficiency of solar cells (Javed *et al*., 2016).

1.3 Significance of the Study

The aim of the research was to synthesize and characterize silver doped zinc oxide nanoparticles using *Citrus reticulata* peel extract as capping agent. The synthesis method is referred to as green synthesis method since it uses less chemicals and most toxic chemicals are replaced with extract from plants which are naturally available and less harmful to environment. The nanoparticles obtained were characterized to determine their efficiency when used in solar cells. The results obtained from this project gave useful information in the manufacturing of solar cell and guide on how the nanoparticles can be obtained from environmentally friendly method. The research findings improve knowledge on the synthesis of nanoparticles and the importance of doping metal oxides for various application. It also form a basis on how to minimize the pollution during the synthesis of nanoparticles for various uses.

1.4. Objectives of the Study

1.4.1 General objectives of the Study

To synthesize and characterize silver-doped zinc oxide using *Citrus reticulata* peel extract for potential application in solar cells.

1.4.2 Specific Objectives

i. To synthesis and characterize silver- doped zinc oxide nanoparticles using *Citrus reticulata*
ii. To determine the effects of silver doping concentrations on the structural and optical properties of zinc oxide nanoparticles
iii. To determine the effects of temperature on the growth of *Citrus reticulata* capped silver-doped zinc oxide nanoparticles.

1.5 Research Questions

1. Is *Citrus reticulata* peel extract effective capping agent for synthesizing Ag-ZnONPs?
2. How does varying the concentration of silver affect structural and optical properties of ZnONPs?
3. Does varying growth temperature affect the structural and optical properties of citrus capped silver-doped zinc oxide nanoparticles?.

1.6 Scope and Limitation

The research entail synthesis and characterization of silver-doped zinc oxide nanoparticles capped with *Citrus reticulata* peel extract. Optimization of a growth temperature, mole % of Ag dopant used were done. *Citrus reticulata* peel extract was used as capping agent and reducing agent only. Only silver ions was used as dopant. The characterization techniques that were used include XRD, FT-IR, UV-vis, PL and SEM. Additionally, the metabolite of *Citrus reticulata* were not analyzed but used as extracted for the synthesis. The research study was limited to using only *Citrus reticulata* peel extract as a reducing and capping agent. Only silver ions were used as dopant. Optimization of growth temperature and concentration of dopant only were carried out.

1.7 Contributions of the Thesis

The contributions made by this study are highlighted below

i. Citrus reticulata capped ZnO and Ag-ZnO nanoparticles were successfully synthesized via green synthesis method and hexagonal wurtzite structure stretching vibration, confirmed by FT-IR analysis at 470 cm^{-1} wavenumber. The use of capping agent lead to a decrease in crystal size. PL analysis showed a shift in emission bands towards NBE when nanoparticles were doped. UV-Vis spectroscopy showed a slight increase in bandgap energy when nanoparticle was doped. Lastly, SEM analysis showed less porous compounds when capping agent was used and confirmed the decrease in crystal size.
ii. Different concentration of Ag was successfully doped to ZnONPs via green synthesis method. The XRD spectra showed an increase in crystallinity as doping concentration increase to optimum level and hexagonal wurtzite structure was maintained. The FT-IR analysis confirm stretching vibration at 466 cm^{-1} associated with Zn-O. The intensity of peaks and stretching vibration increased with increase in doping concentration. PL analysis confirms emission at 350-450 nm, with Ag-ZnO doped with 1.5% silver having the highest intensity. At higher silver concentration the optical properties were improved. UV-Vis analysis showed a decrease in bandgap energy with increase in dopant concentration. EDS confirms that only ZN, O and Ag were present in the sample and SEM images showed confirm an increased in particle size

with increase in concentration. The porosity of the material decreased with increased in silver concentration.

iii. Ag-ZnONPs were successfully synthesized via green synthesis method at a varying growth temperature. The sample prepared at 40 ℃ had the highest intensity in the plane (101) in XRD analysis which confirms better crystal structures. The crystal size of nanoparticles were large at higher temperature. The FT-IR analysis showed stretching vibration at 467 cm^{-1} which is associated with Zn-O and the intensity of the peaks were higher at 40 ℃. For optical analysis the PL analysis showed higher emission at 50 ℃ and the UV-Vis analysis showed a decrease in bandgap energy at this temperature. SEM images showed higher rate of agglomeration at 70 ℃ and an increased in crystal size.

1.8 Organization of the Thesis

The thesis has been arranged into five chapters, with chapter one having the background information of the study, statement of problem, objectives of the study, research questions, significance, scope and limitation of the study.

Chapter two discuss the literature information of the study that include, solar cells, nanoparticles, methods of synthesizing nanoparticles and characterization techniques.

Chapter three outline the materials and reagents that were used in the synthesis process and procedure of obtaining the nanoparticles for the study. It outline how each nanoparticle were obtained as per the objectives and the techniques that were used to characterized nanoparticles.

Chapter four discuss the results obtained from characterization of nanoparticles using XRD, UV-Vis, FT-IR, PL and SEM. The results are discussed as per the objectives order.

Chapter five highlights the summary and conclusions. It has been summarized based on the order of objectives. The recommendation from the study and recommendation for future work has been outlined

CHAPTER TWO
LITERATURE REVIEW

2.1 General Introduction

This chapter focus on scholarly findings on solar cells, nanoparticles and techniques used to synthesize nanoparticles. It mainly focuses on the properties of solar cell and how they can be modified to improve their efficiency using nanoparticles. It also explains the different methods that have been employed to synthesize nanoparticles and mainly focuses on the green synthesis techniques and why this technique is considered environmentally safer than physical and chemicals techniques that have been used in synthesis.

2.2 Solar Cells

Electrical energy is obtained from light energy via photovoltaic effects in solar cells, this phenomenon is both physical and chemical (Bagher *et al*., 2015). Edmond Becquerel in 1839 discovered this and is referred to as the photovoltaic effect. Solar cells are the major components of solar panels. The energy produced by the sun in one hour is more than what is consumed globally in one year (Brainly.com, 2022). The energy from the sun is in the category of electromagnetic radiation and consists of a wide spectrum of wavelength.

For a material to be a component of solar cell, they must be able to convert sun energy to electrical energy (Bagher *et al*., 2015).This occurs when an electron hole pair is created and photons corresponding to an energy similar to or greater are absorbed by the material as shown in Figure 2.1. The amount of light reaching the earth surface is reduced in the atmosphere via the air mass.

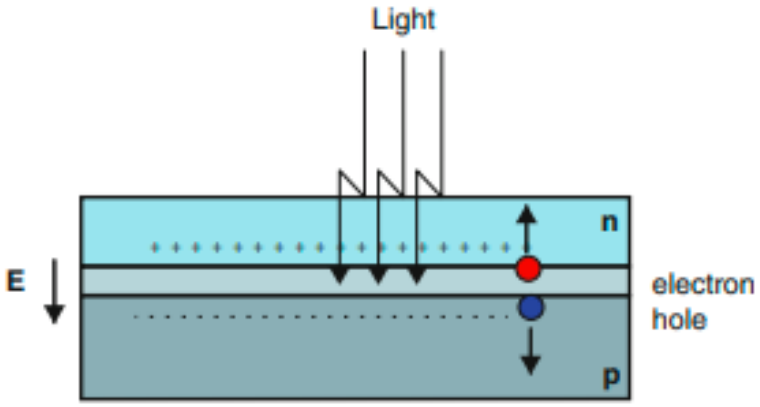


Figure 2.1: Structure of solar cell and effect of light

Source: (Bagher *et al*., 2015)

Solar cells consist of semiconducting materials for example silicon, gallium and indium. These materials have narrow band gap with quantized energy between the valence band and conduction band (Ranabhat *et al.*, 2016). Insulators have a large band gap, therefore need a large amount of energy to move an electrons to the conduction band (Chiang & Wager, 2017). Figure 2.2 demonstrate the difference between insulators, semiconductors and metal/conductors in terms of their band gap.

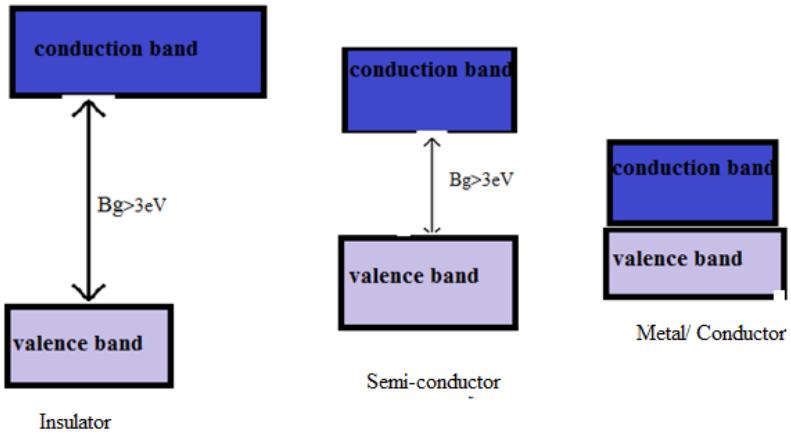


Figure 2.2: Schematic diagram of insulators, semiconductors and metals

Source: (Tian *et al*., 2017)

Insulators have large bandgaps and this prevents electron from gaining enough energy to move to conduction band making them immobile (Tian *et al*., 2017). Semiconductors have bandgap energies that are less than that of insulators and under certain conditions such as high temperature the electron can conduct electricity, they require less energy for excitation to conduction band (Makuła *et al*., 2018). In metals electron flow freely. The highest conduction band that electron occupy is the

conduction band and the lowest unoccupied energy state is the valence band (Endres *et al.*, 2016). Incident photons from sun are used to excite or move electrons from lower energy (valence band) to higher energy (conduction band).

2.3 Electrical Properties of Solar Cells

Figure 2.4 shows the amount of current versus voltage of solar cell in the dark and under illumination.

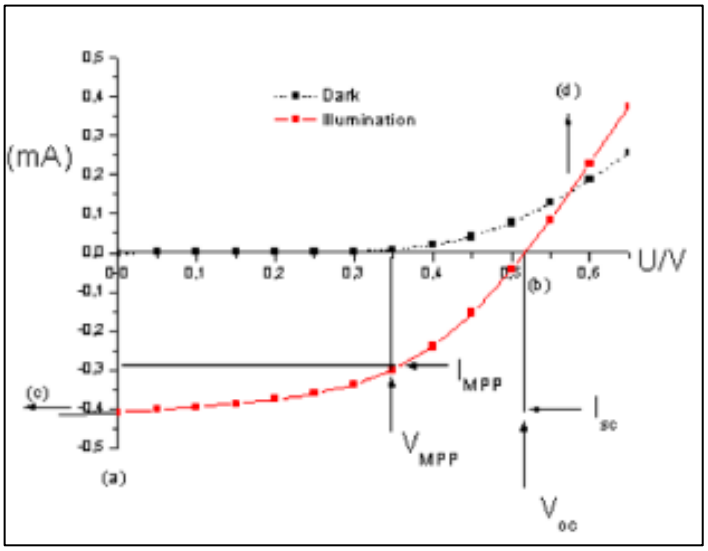


Figure 2.3: Organic solar cell curve of current-voltage

Source:(Leilaeioun, 2018)

There is minimal amount of current flowing in darkness unless the contact initiate significant injection at forward.The point at which the amount of voltage and current is at maximum determine the greatest power output. Fill factor is obtained by dividing power output by current-voltage product (Leilaeioun, 2018).

(a) Is the Maximum current generated flow at short-circuit current condition. (b) At flat band condition photo generated current is balance to zero. At maximum power point (MPP)(a-b) power is generated and the product of current voltage is at maximum (Leilaeioun, 2018). Equation 2.1 and 2.2 are used to obtain the efficiency at which photovoltaic power is converted in solar cell.

The conversion efficiency of photovoltaic power in solar cell is determined by:

$$\eta = \frac{V_{oc} I_{sc} FF}{P_{light}} \quad (2.1)$$

$$\boldsymbol{FF} = \frac{\boldsymbol{I_{mpp}V_{mpp}}}{\boldsymbol{I_{sc}} \times \boldsymbol{V_{oc}}} \quad (2.2)$$

where I_{SC} is short-circuit current, FF is the fill factor, V_{OC} is the open circuit voltage and P_{in} is the incident light power density standardized at 1000 W/m^2 for solar cell testing. The current (I_{mpp}) and voltage (V_{MPP}) at the maximum power point between a and b.

Wien's displacement law state that black body maximum shift towards higher wavelength with its temperature. This means solar cell with large energy band gap has high radiator temperature. Silicon solar cell has a band gap of 1.12 eV (Wagner, 2016).

2.4 Metal Oxides Nanoparticles and their Application in Solar Cells

Metal oxides haves been researched for decades in their advanced application field such as microelectronics and energy conversion (Augusto *et al*., 2017). The widely used manufactured nanomaterials include engineered MONPs (Chavali & Nikolova, 2019). The distinct properties of these NP's are highly ductile at high temperature, behave like super magnet and very selective (Alarcon *et al*., 2016). Bulk materials have higher melting point compared to Nano sized materials.

These distinctive properties of MONP's stem from denser and fewer size of corners and edges of the surface(Chavali & Nikolova, 2019). Alteration of cell structure, such as in NPs of CuO, AgO, CeO_2, ZnO&TiO_2. Structural perturbation occurs as a result of an increase in number of interface atoms due to decrease in size of NPs (Cojocaru *et al*., 2017). Size of nanoparticles alters the properties such as the electronic and magnetic (Jo *et al.*, 2015). Reduced size nanoparticles enhance reactivity.

CuO nanoparticles are extensively used in several fields such as redox catalyst, irradiation process in microwave and photo thermal application (Sreeju *et al.,* 2016). MgO nanoparticles are used in chemical industries as scrubbers to eliminate pollutants that are gaseous such as CO_2& SO_X and in organic synthesis as a catalyst (S. Li *et al*., 2024). ZrO_2 nanoparticles have been used in structural ceramics, solid electrolyte, catalyst and gas sensing material (Dziubaniuk *et al.,* 2024). TiO_2 nanoparticles are applied in solar cell and material science it is also applied in industries related to photo

catalysis of pollutants (Mahlambi *et al.,* 2015). The ZnO is considered to be potential alternative to TiO_2 since they both have a band gap of (3.2eV) and their photocatalytic efficiencies are high (Dorraj, 2018).

The ZnO has a wide band gap that have been exploited for specific properties such as intrinsic, they have few industrial applications such as sunscreen cream in lotion and in solar cells (Sharma *et al.*, 2022). Photo chemist had demonstrated that effective dye uptake can be realized with ZnO nano crystallites (Umar *et al*., 2015).

2.5 Types of Dopants

Doping involves the addition of new material into the crystal structure of the metal oxide (not originally present in the starting material (Carofiglio *et al*., 2020). It is a way of controlling metal oxide nanoparticle properties for example electrical conductivity and oxygen vacancies(Yoon *et al*., 2022). Metal oxides are doped to enhance their properties. The structure of nanoparticles is affected by dopants like Ni, Ag, Co and Mn are used (Türkyılmaz *et al*., 2017). When metal oxides are doped with rare earth metal, they readily combine with functional groups due to the vacant 4f. Some MONP have been doped with both metal and non-metal dopants for solar cells application. In visible regions nitrogen doped titanium oxide have extensive absorption spectrum, this is important in solar cell application since it make use of large part of solar spectrum. Other non-metals used to dope metal oxides for solar cell applications include carbon, sulphur and phosphorus (Marschall & Wang, 2014). In the non-metal doping, carbon and nitrogen are dominant dopant. Zhang *et al.* (2015) detect a decline in band gap upon C-doping. Highest absorption in visible light was 30% carbon doped sample. Table 2.1 shows examples of non-metal dopant used with ZnO (Patil., *et al.* 2023).

Table 2.1: **Synthesis techniques and morphology of non-metal doped ZnO (Patil., *et al.* 2023).**

Dopant	Precursors	Synthesis method	Morphology/particle size	Binding energy (eV)
S	Thiourea (0.25g and 0.5 g) and ZnO	Solid state reaction	Rectangular and square shape	3.07-3.09
N	Guanidine nitrate and ZnO	Micro-emulsion method	Spherical/particle size 15-60 nm	2.40
P	Zinc acetate dihydrate, methanol, ammonium dihydrogen phosphate (2, 4, 6 and 8%)	Sol-gel method	Hexagonal to spherical/particle size 22-40 nm	3.31-3.27
C	$Zn(Ac)_2.2H_2O$,	Co-precipitation	Sandwich structure/particle size 5-14 nm	3.26-3.31

When MONP are doped with metals they show different optical and structural properties compared with undoped MONP. (Abass *et al.*, 2018) doped copper in ZnO for solar cell application and found out that the band gap range for undoped ZnO (3.61 eV) was higher than that of ZnO doped with copper nanoparticles (3.53eV). Shalan *et al*. (2013) found out that M-doped TiO_2 shift spectrum to conduction band and that the dopants occupy the interstitial sites of TiO_2. When the conductivity properties of cobalt doped nickel oxide nanoparticles were analyzed. Kaneko *et al*. (2019) observed that the conductivity improved from 3.83×10^{-6} to 6×10^{-6} S cm^{-}. Another metal that has been widely used as dopant is silver, which has been used as dopant with several oxides of metal such as Fe_2O_3, CeO_2 and ZnO (Sivaranjani *et al*., 2024). Despite being doped to all these materials, it is commonly doped to ZnO because of its ability to enhance photocatalytic activity, electrical conductivity and tunable properties (Wibowo *et al.,* 2020).

2.6 Effects of Capping Agents

Growth rate, shape & stability of nanoparticles formed depend on the type of capping molecule used to synthesize (Javed *et al.*, 2020). The capping molecules prevent excessive size of nanoparticles during colloid synthesis and stop aggregation from taking place (Javed *et al*., 2020). They are amphiphobic with non-polar tail and polar head. The polar and non-polar interact with metal atom and surrounding medium respectively (Gulati *et al*., 2018). Some of the capping agents that have been successfully used to synthesize nanoparticles are polymers such as polyethylene glycol and polyethylene oxides, acetic and oleic acids (Radini *et al*., 2018). Jin & Jin (2019) synthesized ZnONPs using tea, oleic acid and thioglycerol. The nanoparticles of tea and oleic acid had low luminescence intensity compared to that of thioglycerol.

2.7. Structural Properties of Metal Oxides Nanoparticles

Nanoparticles exist in various forms such as nanowires, nanotubes, Nanocones, nanopillars, nanobelts, nanocombs and nanorods (Alshammari *et al*., 2023).

2.7.1 Nanowires

Nanowires- they are structures with diameter of order of nanometer and extensive surface area causing length to ratio of equal or more than 1000. In fluorescent MRI magnetic and fluorescent nanowires are used (Nana *et al*., 2019).

2.7.2 Nanotubes

Nanotubes- they have distinct properties because they rely on geometry and their composition (Schulz *et al*., 2014). TiO_2 are used in dye sensitized solar cell as photoanode because of its shape that allow large surface area to volume ratio and greater electron mobility (Sengupta *et al.*, 2016).

2.7.3 Nanocones

Nanocones- nanocones have high absorption compared to nanowires because they have smaller tip, the reduced tip size leads to less reflection of incident light resulting to improve absorption (Magdi *et al.*, 2018).

2.7.4 Nanopillars

Nanopillars are grouped in the lattice and have pillar shaped structures with diameter of about 10 nm (Valiei *et al.,* 2022). These structures are extensively used in solar panels.

The study of form comprising of appearance, construction and dimension is referred to as morphology. The nanomaterials optical, chemical and structural properties are influenced by morphology; thus, morphology determines the various applications of material. The morphology of nanoparticles is analyzed using scanning or transmission electron microscopes. The morphology of nanoparticles is affected by; quantity and strength of surfactant which passivate the surface, dioctylphosphine oxide (DOPO) is a weak surfactant used to make CIS wires (TOPO) (Van Embden *et al.*, 2015). Surfactants have lengthy hydrocarbon chains which play a significant function in controlling particles size (Song *et al*., 2021). The pH affects the sol gel synthesis, the morphology of MONPs relies mainly on the H^+ or OH^-concentration on the sol, the ions determined the bond between oxygen and metal (Arya *et al.*, 2021). The Table 2.2 shows how pH affects the size of nanoparticles and the energy band gap *(*Alias *et al*., 2010).

Table 2.2: Effects of pH on the band gap, particle size and crystal size of ZnO nanoparticles *(*Alias *et al*., 2010).

Item	**pH values**				**Observation**
	8.0	9.0	10.0	11.0	
Size of particle (nm)	48.97	48.31	38.32	36.65	Inversely proportional
Crystallite size (nm)	24.96	25.36	21.87	18.37	Inversely proportional
Band gap energy (eV)	3.25	3.24	3.23	3.14	Inversely proportional

Post treatment annealing, suitable growth temperatures and accumulation of particular dopant control the morphology of nanoparticle (Hui *et al*., 2017; Mohar *et al*., 2016). Table 2.3 shows how annealing temperature affect the morphology of nanoparticle (Kayani *et al*., 2015).

Table 2.3: **Effects of annealing temperature on structural size, band gap and crystal size (Kayani *et al*., 2015).**

Annealing temperature (℃)	**Ambient temperature**	**300**	**500**	**650**	**700**	**Observation at increasing temp**
Crystal size (nm)	20.0	27.9	28.4	28.9	32.6	Direct proportional
Structural size (nm)	28.0	31.4	46.0	48.0	54.0	Direct proportional
Energy of band gap (eV)	3.00	3.10	3.13	-	3.20	Direct proportional

2.8 Optical Properties of Nanoparticles

In photocatalytic applications, to uncover the mechanism of photochemical process photo chemist have develop a strong understanding since these techniques are used to determine the optical characteristics of nanoparticles (Khan & Khan, 2019). Optical characterization is based on beers-lambert law & light principles (Hassan & El-mallul, 2025). The techniques convey information on nanoparticles such as absorbance, luminescence, band gap and reflectance. Light can be absorbed or scattered when it is incident on nanoparticle depending on size of nanoparticles (Carvalho *et al.*, 2018). At a diameter less than 20 nm nanoparticles experience both scattering and absorptions. The diameter of nanoparticles is obtained from SEM. SEM is a reference analytical technique for dimensional properties of nanoparticles. The measurement properties are obtained from secondary electrons. The diameter of NP can be calculated using equation 2.3 (Crouzier, Delvallee, et al., 2019)

$$\boldsymbol{u(p1) = u(p2)} \quad (2.3)$$

Where p1 and p2 are the position of the pixels and a is the pixel size set as 1nm. Equation 2.4 shows uncertainty associated with Deq measurement on u (Deq)

$$\boldsymbol{u(Deq) = \sqrt{u(p1)^2 + u(p2)^2}} \quad (2.4)$$

Where Deq correspond to the distance between pixels (Crouzier, *et al*., 2019)

The UV-vis is fully equipped device which can measure reflectance and transmittance of NP. It is mainly applicable in measuring the bandgap of NPs and nanomaterials. Band gap of materials determines its conductance and photo activity. Liu *et al.*, (2015) concluded that the photo ability of carbon Nano dot-carbon nitride is closely linked with the band gap value 2.70-2.80 eV, it was obtained from UV-vis spectroscopy. This technique is also used to observe the effect of dopant on the absorption shift.

Semiconductors NP have various application such as luminescent materials, optoelectronic lasers (Hossain *et al*., 2023), light emitting diodes white. Aguilar Jáuregui *et al.* (2022) obtained photoluminescence spectra of pure and doped nanoparticle of ZnS, with excitation wavelength of 330 nm and the transmission wavelength in the blue was 368 nm for the pure nanoparticles. When doped with Ce^{+3} the wavelength shifted towards blue at 447 nm with two times luminescence intensity than pure nanoparticles (Aguilar *et al.,* 2022). Figure 2.4 shows the emission spectra obtained by Aguilar *et al.,* when ZnO was doped with Ce.

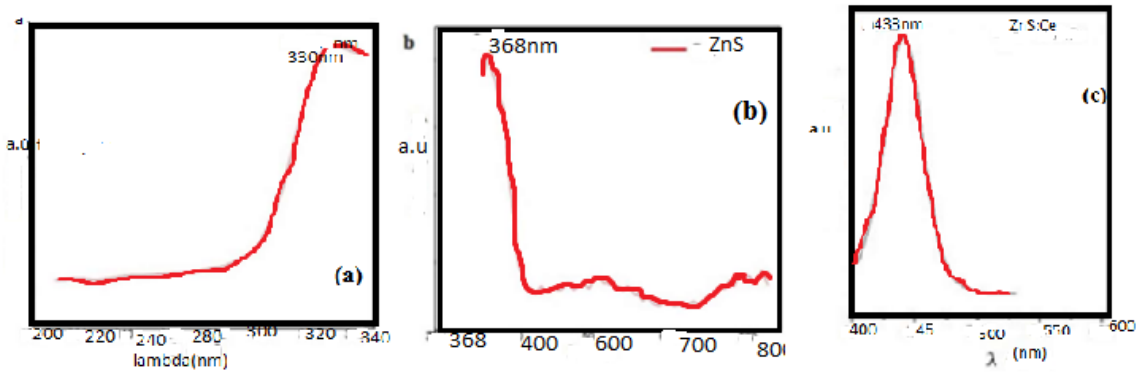


Figure 2.4: Emission spectrum at (a) 330nm (b) 368nm and (c) 433 nm of ZnS

Source: (Aguilar et al., 2022)

2.9 General Properties of Zinc Oxide Nanoparticles

2.9.1 Electronic Properties

Semiconductors in group II–VI are used in solar cell (De Melo, 2023). (Pieniążek *et al.*, 2016) reported that the excitation radius of bulk ZnO is 2.24 nm. This is similar to confinement note able effect, ZnO particles of less than 4 nm can be observed in

solution phase synthesis as a result of small effective mass of ZnO , $m_e = 0.26m_o$, $m_h = 0.59m_o$ and (m_o) free electron mass (S. Singh et al., 2024). The ZnO particles have high electron mobility making it an excellent material for photo anode application in solar cell, the mobility of bulk and nanorod ZnO are 205-300 and 1000 $cm^2\ v^{-1}\ s^{-1}$respectively (Pan *et al*., 2016).

(Ahmad et al., 2018) reported that electron diffusion coefficient of ZnO nanoparticles is 1.7 and that of bulk is 5.2 $cm^2\ v^{-1}s^{-1}$. Conversely, the electron diffusion coefficient for TiO_2 nanoparticles and bulk is 10^{-8} -10^{-4} and 0.5 $cm^2\ v^{-1}s^{-1}$ respectively (Mugambi *et al.*, 2023). The structure of ZnO nanoparticles depend on method of synthesis, it comprises of nanospheres, nanorods, nanowires, nanocrystals, nanotubes and 3D nanostructure. The ability to mold into different structure has led to wide application of ZnO nanoparticles.

The orientation and size of ZnO nanorod determine its photovoltaic characteristics (Mwankemwa *et al.*, 2022). Power conversation efficiency is low in ZnO nanorods if they are aligned vertically and have sensitization of N179 (Wibowo *et al*., 2020,). Pure ZnO nanostructures have weak optical properties as a result of point defect such as oxygen vacancy or interstitial Zn, these factors limit its pure uses in the industry.

2.9.2 Crystal Structure

The ZnO have different structures for example zinc blende, rock salt and wurtzite ; at normal condition it exist as wurtzite having ionicity between ionic and covalent semiconductors (Rai & Kondal, 2022). The unit cell for zinc oxide has Zn^+ encircled by four oxygen ions forming a tetrahedral each having two formula units (Van Embden *et al*., 2023). Non-centrosymmetric coordination in tetrahedral ZnO bring about defects and crystal growth since they produce piezoelectric properties and crystals polarity (Goel & Kumar, 2020). The ZnO lattice properties are measured by x-ray diffraction (Bindu & Thomas, 2014). The parameter ranges from 3.2475 to 3.2501 a, for c parameters the values range from 5.2042 to 5.2075 Å, with difference in lattice parameters depending on defects, external strain and temperature (Wu *et al.*, 2019).

2.10 Doped Zinc Oxide Nanoparticles

Doping involves the addition of new material into the crystal structure of the metal oxide (not originally present in the starting material (Carofiglio *et al*., 2020). Doping of ZnO enables the approach to tune in various zinc oxide properties. The sensing ability of zinc oxide is determined by several factors such as oxygen vacancies. Dopants can improve sensors' performance reducing activation energy connecting the sensing material and the target analyte.

Singh *et al*. (2019) employed several metals to create metal doped zinc oxide nanoparticles and found out that metal doping reduces temperature and increase the sensing efficiency as a result of decrease in activation energy. The concentration of metallic dopant affect the morphology of material improving its sensing efficiency (Sarkar *et al*., 2015). Figure 2.5 shows a typical wurtzite hexagonal shape of pure ZnO; Ce-ZnO composite morphology changes to nanoparticles as the concentration increases (2.5b) and further to flocculent structure (Figure 2.5 c), agglomeration occurs when the concentration of dopant Ce is increased (2.5d) (Flores-Carrasco *et al.,* 2021).

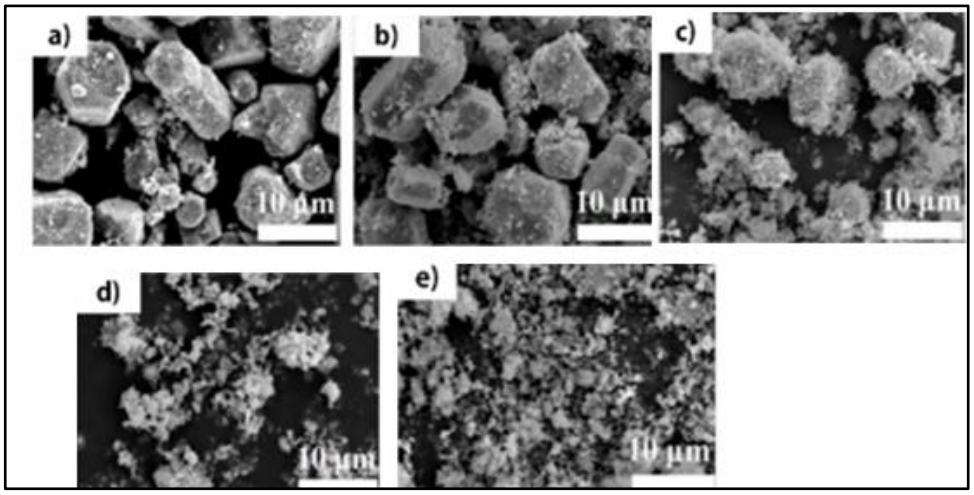


Figure 2.5: (a-e) SEM images of Ce-ZnO at different concentration of Ce loaded: (a) ZnO NPs, (b) 2.02 %, (c) 3.24 %, (d) 6.24 % and (e) 8.24 %

Source: (Flores-Carrasco *et al.,* 2021)

When dopant concentration of less than 10% is introduced to semiconductor the absorption edge of photo catalyst shift to visible range (Murashkina *et al*., 2015). The interaction of ZnO valence band with metal cations result in formation of intra-band gap level which induces narrowing of band gap. When metal ions are doped with p-

type, the p type serves as electron acceptor and introduce level below the original gap, while n-type when used as electron donors act oppositely by creating a level above the valence (Samadi *et al*., 2016).

Masoumi *et al.*, 2018 analyzed the properties of Ag-doped ZnO with first principles calculation. From the results they obtained, they concluded that Ag was acting as electron acceptor in the zinc oxide nanoparticle structure. When silver is introduced inside ZnO it creates acceptor level resulting in decrease of E_g value. Silver is used to create p type of conductor at the same can be used to introduce n type conductivity. In their calculation they used a concentration of 2.08% silver dopant, which had only one Ag substitution at an interstitial site, oxygen site and Zn site (Masoumi *et al*., 2018). In each formation energy for a single Ag dopant were calculated; the result showed AgZn substitution has the lowest formation energies which, means that the dopant will prefer to substitute at Zn site in presence of O rich and Zn site.

Visible light absorption edge occurs when electrons are promoted from valence band to conduction band. Increasing concentration of silver dopant causes a significant increase in red-shift absorption edge since more impurities increase mid-gap states(Samadi et al., 2016). Incorporation of silver ions in zinc oxides lattice structure has been confirmed by x-rays and spectroscopy techniques. The Ag^{+} radius is larger than Zn^{2+} radius, thus the unit cell volume is high (Surib *et al*., 2017). Low XRD 2θ values are observed when Ag is substituted in ZnO as shown in Figure 2.6 (Chitradevi *et al*., 2020).

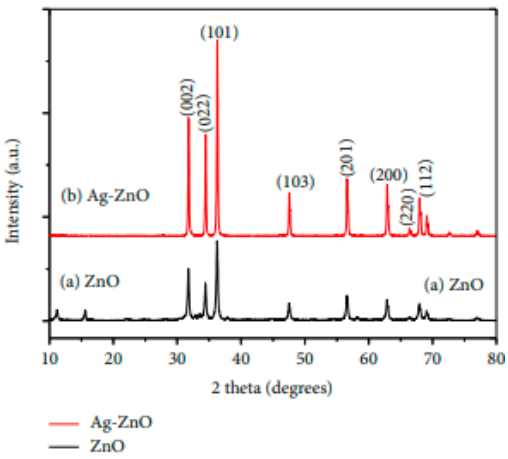


Figure 2.6: The XRD pattern of Ag-ZnO

Source: (Chitradevi *et al.,* 2020)

When Ag is doped in ZnO the Raman spectra shift to higher wave number indicating lattice expansion due to doping as shown in Figure 2.7 (Lefatshe *et al.*, 2021).

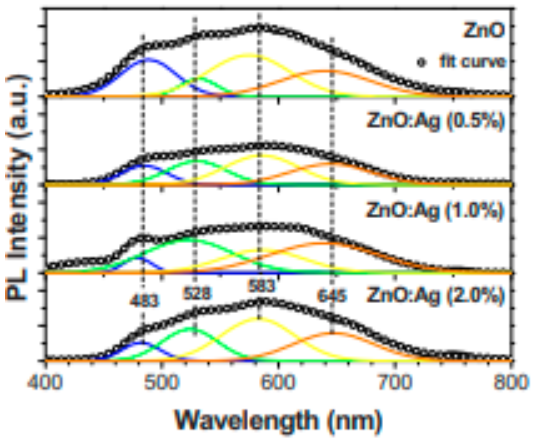


Figure 2.7: Visible PL band for the ZnONPs with: (a) undoped (b) 0.5%, (c) 1.0%, and (d) 2.0% of Ag

Source: (Lefatshe *et al.,* 2021).

Since Zn^{2+}radius is smaller than Ag^{+} radius (sharwani *et al.,* 2022). Kaningini *et al.* (2022) use precipitation method to prepare Ag-ZnO using different concentration of Ag at low temperature and the observation was that when equal or less than 0.5 mol% of Ag is introduced, the Ag will occupy the lattice site via the substitution of Zn^{2+}. When the concentration of silver ions was increased above 0.5 mol %, Ag atoms agglomerate at the ZnO grain boundary. Thabit *et al.* (2022) showed that if the concentration of silver dopant is above the optimum there is a decrease in the mobility of ZnO thin film causing film disorder.

2.11 Synthesis of Nanoparticles

Several techniques have been employed to prepare nanoparticles. These methods are categorized into three; physical, chemical and biological methods. The most extensively used methods include; chemical precipitation, sol gel methods and biological /green synthesis methods.

2.11.1 Chemical Precipitation

When synthesizing zero valent nanoparticles chemical precipitation method is used (Dandge *et al.*, 2021). The crystal size of nanoparticles is controlled by arrested precipitation technique (Rajput, 2015). The precipitation reaction process involves the reaction of precursor material and the suitable solvent. If the reaction involves doping,

dopant must be added before chemical precipitation. Surface active agents are used to prevent agglomeration from taking place, nanocrystals are centrifuged, washed and vacuum dried.

2.11.2 Sol gel techniques

This method is used in industrial production of nanoparticles having the same size and of high quality (Bokov *et al.*, 2021). It uses bottom up approach whereby nanoparticles are formed from simple components (Tripathy *et al.*, 2023). Salts with different compositions and reaction rates are used (Bokov *et al*., 2021).When the cavities of polymer gel formed are joint, a 3D structure is obtained which is then dried to get a rigid solid due to volumetric shrinkage (Danks *et al.*, 2016). When drying condition is controlled the porosity of nanoparticles can be achieved and the products are of high quality (Bokov *et al*., 2021). Figure 2.8 below show the steps involved in the sol-gel synthesis of nanoparticles. The cryogel, xerogel and aerogel obtained are calcined to obtain the final products.

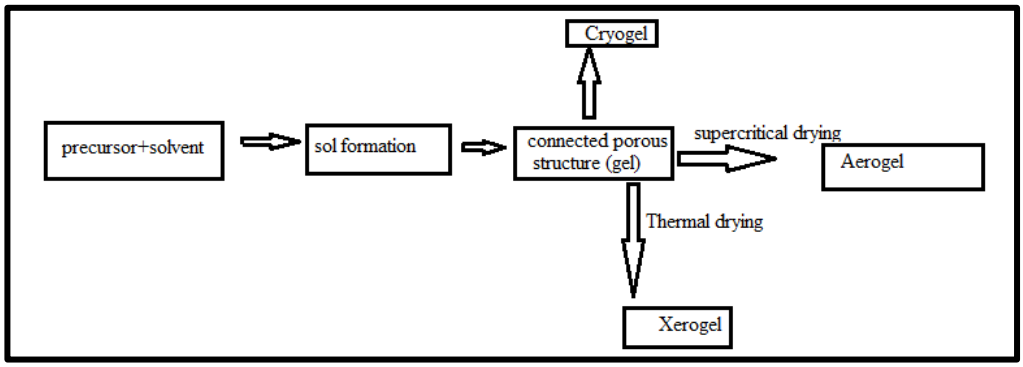


Figure 2.8: Stages of sol-gel synthesis

Source: (Bokov *et al.,* 2023)

2.11.3 Biological/green Synthesis Method

Nanoparticles are widely applied in areas where they come in contact with human therefore, there is need to develop process of synthesis without using harmful chemicals. Green synthesis is rapidly gaining importance over the other methods, since the process of production is of low cost and it produces limited amount of waste. Chemical precipitation and green synthesis both uses bottom-up approach to prepare nanoparticles but in green synthesis the surface reducing agent used is plant extract such as peel extract, fruits and leave. The term green synthesis is used because the

harmful chemicals are replaced with plant extract which are friendly to the environment.

Green synthesis was used to synthesize metal oxides such as titanium oxide and the plant extract that was used as capping agent was an extract of *Aloe vera* (Rao *et al.*, 2015). The concentration of plant extract affect the size of nanoparticles formed. The properties of nanoparticles synthesized via green synthesis methods differ from those synthesized by chemical methods for example the biocidal activity of green synthesized ZnO nanoparticles is high compared to that prepared by chemical precipitation (Elumalai & Velmurugan, 2015).

Citrus reticulata is a fruit obtained from citrus tree which belong to genus *Citrus*, they are mainly associated with oranges and lemons. They produce their own seeds within the fruits, and the peel contains phytochemicals compounds that have been used in medical, cosmetics and scientific applications (Apraj & Pandita, 2016). A. K. Ibrahim et al., 2024) observed from the analysis of *Citrus reticulata* peel extract that it contained n-hexacosanoic acid (CH_3 $(CH_2)_{24}COOH$) based on the spectra analysis of data. The other compounds that were obtained include reticulataursenoside, citrusteryl and citruslanosteroside which gave positive tests on triterpenic glycosides. These chemical components play key roles as capping agents when synthesizing nanoparticles. Other citrus plants that have been used to synthesize nanoparticles include lemons used to synthesize TiO_2 (Nabi *et al*., 2022) and citron (*Citrus midica*) leaf extract which was used to synthesize cobalt oxide (Siddique *et al*., 2021). The current study utilized *Citrus reticulata* peel extract for the synthesis of Ag-ZnONPs.

2.12 Analytical Techniques used to Characterize Nanoparticles

Various techniques are employed to characterize nanoparticles for different applications. Characterization is the study of materials properties such as structure, composition, magnetic electrical, chemical and physical properties. Most of the techniques can analyze more than one property but some are used to analyze only one property. They are classified into microscopy for example TEM and SEM, spectroscopy (FT-IR and UV-vis), X-ray techniques.

2.12.1 Fourier Transform Infrared Spectroscopy

It measures electromagnetic radiation absorbed at a wavelength of (400-4000 cm^{-1}) in the mid IR region. Molecule is said to be IR active if it absorbs the IR radiation. The FT-IR identify the molecular structure of compound by showing the functional groups through spectrum which shows the position and strength of bonds (Blanco 2014). If organic acids are used to synthesize nanoparticles the spectra will show the presence of characteristic groups such as -HC=CH- on the surface of nanoparticle. In the mid infrared region there are two types of vibration observed: the stretching and bending vibrations. Stretching vibration mainly involve the change in bond length whereas bending vibration is more of change in the bond angles. The vibration frequencies depend on bond strength with triple and double bond having the highest frequency as compared with single bond. Chemical groups have specific vibration frequencies that depends on atoms involved and the type of chemical bond.

The FT-IR works on the principle that detector receive the absorbance of all wavelength simultaneously when light is passed through the sample. Fourier transform which is a mathematical computerized manipulator performed the data so that absorption of every wavelength is obtained. The FT-IR contained two mirrors which provide interference of light that help to performed mathematical manipulation. Among the two mirrors, one is fixed while the other is flexible and beam splitter is positioned between the two mirrors. Blank scanning is required before any sample is scanned. Figure 2.9 shows the Shimadzu FT-IR at Murang'a University of Technology.



Figure 2.9: Shimadzu IR spirit FT-IR model

2.12.2 Ultra Violet Visible Spectroscopy

It is relatively cheap technique used to analyze nanoparticles. It correlates the intensity of light reflected from the sample to that reflected from the reference material. The UV-vis analyze the transmittance or absorbance used to determined optical bandgap energies of nanoparticles. The absorbance mode measures the quantity of light absorbed by compound as a function of wavelength and a graph of absorbance against wavelength is obtained. This graph is referred to as an absorption spectrum. In transmittance mode, the intensity of light transmitted through the sample is evaluated as a function of wavelength and the graph obtained is transmission spectrum. These properties are influenced by size and shape of nanoparticle (Blanco Andujar, 2014). Metallic nanoparticles like Ag and Au interact strongly with certain wavelength of light, these distinctive properties enable them to be used in plasmonic. Besides characterizing NP it can also quantify zero valent elements such as gold and silver. Bindhu *et al.,* 2020 synthesized Ag NP via green synthesis using the flowers extract of *Moringa oleifera*. The UV-vis analysis confirmed the presence of localized surface plasmon resonance (LSPR) in the particles and the spectra showed a blue shift as the crystal size of nanoparticle decrease with an increase in concentration of flower extract. Figure 2.10 shows the evolution one plus model UV-vis spectroscopy at Murang'a University of Technology.



Figure 2.10: Evolution one plus UV-Vis spectroscopy

The bandgap energy values of nanoparticles were estimated by plotting a graph of $(\alpha hv)^2$ versus energy (eV) then extrapolated according to Tauc's equation (2.5)

$$(\alpha hv)^{\gamma} = A(hv - E_g) \quad (2.5)$$

Where Eg is the bandgap energy, A is a constant, h is the plank's constant, v is the photon frequency,α symbolize absorption coefficient and γ designate the electronic transition and can be 2 or ½ for direct and indirect allowed transition respectively. It can also denote direct or indirect forbidden transition if its 2/3 and 1/3 respectively. If Taucs equation is compared to the equation of straight line shown in 2.6 such that

$$\mathbf{Y=m(x)} \quad (2.6)$$

Putting the y axis equal to zero then, equation 2.7 will be obtained

$$\mathbf{0=A\,(hv-Eg)} \quad (2.7)$$

Thus, the bandgap extrapolated will be equal to energy obtained as shown in equation 2.8

$$\mathbf{hv=Eg} \quad (2.8)$$

2.12.3 Photoluminescence Spectroscopy

Photoluminescence (PL) spectroscopy monitors molecules that have absorbed or emitted light. It is useful in characterizing quantum dots and metal nanocluster. The presence of near infrared localized surface plasmon (NIR LSP) resonances in nanoparticles have major impact on the exciton recombination. Addition of impurities such as transitional metals into semi-conductors materials makes the luminescence centers, Some metal oxides such as ZnO nanoparticles are active photo luminescent (Rodrigues *et al.*, 2020). PL has the ability to measure band gap directly as a function of carrier concentration. It is convenient for detection of low level impurities, and to determine the major defects in samples (Ungula, 2018).

In this work, the photoluminescence data were collected using Infitek SP-LF97 model shown in Figure 2.1. It uses xenon flash lamp for superior sensitivity.



Figure 2.11: SP-LF97 model PL spectroscopy

2.12.4 The X-ray Diffraction

The X-ray diffraction provides details regarding the structure and size of crystal and lattice parameters of nanoparticles. Lattice parameter d-spacing are estimated using Bragg's equation. The samples to be analyzed by XRD are commonly in thin films and powder form. XRD cannot be used to analyze amorphous materials and nanoparticles with grain size of less 3 nm. The XRD methods depend on the ability of crystals to diffract X-rays in a characteristics way that allow study of crystalline phases. Figure 2.12 shows the ARL EQUINOX X-ray diffractometer.



Figure 2.12: The ARL EQUINOX X-ray diffractometer

The intensity of the peak is used to obtained details on the crystal structure and texture of material (Epp, 2016). Radiation sources such as sealed tubes, synchrons and rotating units are generally used to generate X-rays. When crystalline materials are analyzed, the principle of the method depend on diffraction of X-ray atomic planes. Bragg's explained the geometrical interpretation of XRD using Bragg's law. Bragg's law is given in equation 2.5 below.

$$n\lambda = 2d_{hkl}sin\theta \quad (2.5)$$

In equation 2.5 n is diffraction order, λ is the wavelength in (nm) of incident beam, θ is the angle of diffracted beam in degrees and $d_{hkl}$is the lattice spacing. Figure 2.13 shows how the lattice planes at different miller indices diffract from different planes.

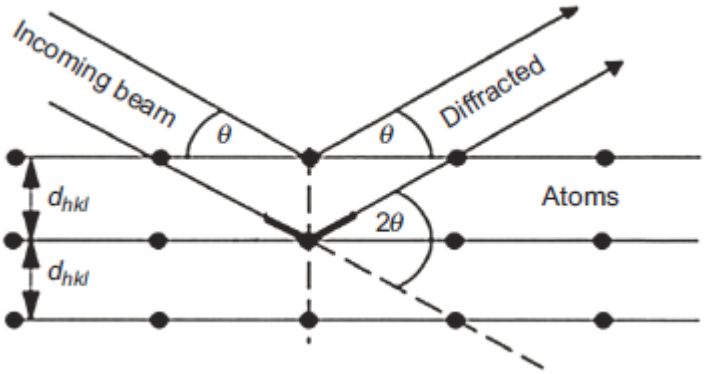


Figure 2.13: Geometrical condition for diffraction from lattice planes

Once the diffraction pattern has been obtained qualitative phase analysis is carried out to identify the type of phase. The diffraction pattern is compared with that of standard obtained from International Center for Diffraction Data (ICDD) other standard can be obtained from Joint Committee on powder Diffraction Standards (JCPDS) where peak information is compared manualy for the purpose of identifying the phases present. The crystallite size was calculated from the peak broadening of diffraction peak using Debye Scherrer formula shown in equation 2.9. (Mustapha *et al.*, 2019)

$$D = \frac{K\lambda}{\beta cos\theta B} \quad (2.9)$$

Where λ is wavelength of X-ray radiation, β is width at half maximum of diffraction and θB the Bragg's angle. Lattice parameters was calculated using equation 2.10

$$a = \sqrt{\frac{n^2\lambda^2}{4sin^2(\theta)}}(h^2 + k^2 + l^2) \quad (2.10)$$

Where a is lattice parameter and h, k, l are miller indices

The length of dislocation line was measured using dislocation density $\delta$and the number of dislocations per unit volume of the crystal was calculated using equation 2.11 (Al-Ansari, 2016)

$$\boldsymbol{\delta = \frac{1}{D^2}} \quad (2.11)$$

D is a grain size from the Scherrer formula.

2.12.5 Microscopy Techniques

The most common microscopy techniques used to analyze nanoparticles are SEM and TEM. These microscopes have primary electrons that provide high energy and electron gun which act as a creator of electrons at a controlled energy. Fine beam of electrons are generated from the gun, precisely controlled energy. The TEM operate on the principle that when electron beam hit the sample some are transmitted while the excess electrons are scattered (Akhtar *et al.*, 2018). The TEM provides the most accurate estimation of nanoparticles homogeneity and the nanoparticles size and shape. For these reasons TEM are used to analyze nanoparticles aggregation of various applications for example the sensing and diagnostic (Shrestha *et al*., 2020), where the aggregations depend on the analyte. Nevertheless, this technique has some limitations that have to be considered such as orientation effect which leads to production of misleading images.

Scanning electron microscope (SEM) uses electrons for imaging, cathode generates electrons that are forwarded to anode. Compared to light microscope, SEM images are of higher magnification, the image are 3D produced by electrons. The SEM images of ZnO has been reported to influence by synthesis condition and treatment phase. The ZnO nanoparticles has been reported to be spherical in shape by (Javed *et al.,* 2016)

Scanning electron microscope (SEM) equipped with energy dispersive X-ray spectroscopy (EDS) VEGA3 (TESCAN) model was use to study the morphological properties and elemental analysis of *Citrus reticulata* capped Ag-ZnONPs.

2.13 Summary

This chapter detailed the literature of zinc oxide properties (ZnO), solar cells, doping, application, synthesis methods and characterization techniques employed during the

research. Zinc oxide has either hexagonal wurtzite structure or zinc blende structure with optical bandgap energy of 3.37 eV. Adding foreign atoms in the lattice crystal structure has proved that it improve the sensor's performance and as a results decreased the activation energy.

CHAPTER THREE
MATERIALS AND METHODS

3.1 Introduction

This chapter outlines the materials and methodology that was applied in the synthesis of ZnO nanoparticles using Citrus reticula peel extract, doped with silver at different concentration and varying the growth temperature. Green synthesis method was used for the synthesize Ag-ZnO.

3.2 Materials

All the chemicals that were used were of analytical grade and were used without any form of purification. All chemicals were purchased from Sigma Aldrich & A.B Chem. Co., Ltd. They include zinc acetate dihydrate (Zn $(CH_3COO)_2.2H_2O$) (>98%), ammonia hydroxide (NH_4OH) (>99%), silver nitrate ($AgNO_3$) (>99.9%), ethanol (CH_3CH_2OH) (>99%). The deionized water was prepared in the Murang'a University of Technology Research Laboratory. *Citrus reticulata* was obtained from the Murang'a market sourced from Makueni County, Kenya.

3.3 Preparation of *Citrus reticulata* peel extract

Citrus reticulata (tangerine) was washed with deionized water to remove surface pollutants then hand peeled. To obtain the peel extract, the peels were dried in air in the absence of sunlight at temperatures of about 27 to 28 ℃. The dried peels were milled using an electric mill and sieved to powder. Fifty grams of the sample was introduced to 500 mL of deionized water and heated at a temperature of 80 ℃ for 15 minutes (Ehrampoush *et al.*, 2016). After cooling to ambient temperature, it was filtered with 1mm Whatman filter paper and stored in a refrigerator to be used as capping agent in the analysis.

3.4 Synthesis of Zinc oxide (ZnO) nanoparticles using *Citrus reticulata* peel extract

A 3.84 g of zinc acetate dihydrate was dissolved in 50 mL of deionized water and stirred for 5 minutes at room temperature. *Citrus reticuata* peel extract 20 mL was added to the solution and stirred, followed by 10 mL of ammonia hydroxide. The mixture obtained was stirred at a temperature of 40 ℃ for 3 hours then allowed to settle for 24 hours before being washed with analytical ethanol. The NPs formed were

dehydrated in hot air oven at 100 ℃ for 2 hours then annealed in a muffle furnace at a temperature of 450 ℃ for 3 hours.

3.5 Synthesis of Zinc oxide nanoparticles without *Citrus reticulata* peel extract

A 3.84 g zinc acetate dihydrate was dissolved in 50 ml of deionized water and stirred for 5 minutes at an ambient temperature to allow the salt to fully dissolve. Ammonium hydroxide (10 mL) were then added to the solution and stirred for 3 hours at 40 ℃ till they formed a precipitate. The precipitate formed was allowed to settle for 24 hours then washed with analytical ethanol, dried at 100 ℃ for 2 hours in an oven, then annealed in a muffle furnace for 3 hours at a temperature of 450 ℃.

3.6 Synthesis of *Citrus reticulata* capped silver-doped zinc oxide nanoparticles

Zinc acetate dihydrate solution was prepared by dissolving 3.84 g in 50 mL of deionized water and stirred for 5 minutes at ambient temperature. Peel extract (20 mL) was added to act as capping agents leading to formation of zinc ions. The mixture was then stirred for 20 minutes (Anon *et al.* 2021)

$$\mathbf{Zn}(\boldsymbol{CH_3COO})_{\mathbf{2}}.\boldsymbol{2H_2O_{(s)}} + \mathbf{2}\boldsymbol{C_6H_8O_{7(Aq)}} \rightarrow \boldsymbol{Zn^{2+}_{(Aq)}} + \mathbf{2}\boldsymbol{CH_3COO^-_{(Aq)}} + \mathbf{2}\boldsymbol{H_2O_{(Aq)}} + \boldsymbol{C_6H_8O_{7(Aq)}} \quad (3.1)$$

Zinc ions formed were reacted with 10 mL of ammonium hydroxide to form zinc hydroxide nanoparticles.

$$\boldsymbol{Zn^{2+}_{(Aq)}} + \mathbf{2}\mathbf{NH_4}\mathbf{O}\boldsymbol{H_{(Aq)}} \rightarrow \mathbf{Zn}(\mathbf{O}\boldsymbol{H})_{\mathbf{2}(\boldsymbol{Aq})} + \mathbf{2}\mathbf{N}\boldsymbol{H^+_{4(Aq)}} \quad (3.2)$$

Silver nitrate (0.75 mol%) was added and stirred at a temperature of 40 ℃ for 3 hours to form silver doped zinc oxide nanoparticles. The Ag-ZnONPs formed were washed with analytical grade ethanol and allowed to settle for 24 hours before being dried at 100 ℃ for 2 hours in the oven and annealed at 450 ℃.

3.7 Synthesis of silver-doped zinc oxide nanoparticles without *Citrus reticulata*

A 3.84 g zinc acetate dihydrate was dissolved in 50 mL of deionized water and stirred for 5 minutes at room temperature, followed by 10 mL of ammonium hydroxide and the solution was stirred. After which 0.75 mol% of silver was added and stirred at 40 ℃ for 3 hours. The nanoparticles formed were allowed to settle for 24 hours before

being washed with analytical ethanol and dried at 100 ℃ in hot air oven for 2 hours and annealed in a muffle furnace for 3 hours at a temperature of 450 ℃.

3.8 Synthesis of different concentration of silver mol % doping concentration on the optical and structural properties of ZnO nanoparticles

A 3.84 g zinc acetate dihydrate was dissolved in 50 mL of deionized water and stirred for 5 minutes at room temperature, followed by 20 mL of *Citrus reticulata* peel extract and the solution was stirred. After 5 minutes 10 mL of ammonium hydroxide was added. Different concentrations of silver ions (0.1, 0.25, 0.5, 0.75, 1.0, 1.5 and 2.0 mol %) were added and stirred at 40 ℃ for 3 hours. The nanoparticles formed were allowed to settle for 24 hours then washed with analytical ethanol and dried in hot air oven for 2 hours at 100 ℃ and annealed at 450 ℃ for 3 hours in the hot air furnace.

3.9 Synthesis *Citrus reticulata* capped silver-doped zinc oxide nanoparticles at different growth temperature on the structural and optical properties of Ag-ZnO nanoparticles

Citrus reticulata capped silver-doped zinc oxide were synthesized at varying growth temperatures:

A 3.84 g of zinc acetate dihydrate was dissolved in 50 mL of deionized water and stirred for 5 minutes to ensure the salt dissolved completely. A 20 mL of *Citrus reticulata* peel extract was introduced to a solution of zinc acetate dihydrate followed by 10 mL of ammonia hydroxide. Silver nitrate was added (0.75 mol %) to the solution and stirred at a temperature of (25, 30, 40, 50, 60, 65 and 70 ℃) for 3 hours, then allowed to settle for 24 hours, then washed with analytical grade ethanol and dried at 100 ℃ for 2 hours in the oven and annealed at 450 ℃ for 3 hours in the hot air furnace. The nanoparticles obtained were then ground to powder using a mortar and pestle.

3.10. Characterization of the synthesized nanoparticles

3.10.1 UV-Vis characterization

The UV-Vis was turned on and calibrated using the standard reference material (material of known absorbance at specific wavelength); an appropriate wavelength was selected (200-1100 nm). *Citrus reticulata* capped Ag doped ZnO sample was dissolved in deionized water. The solution obtained was placed in a sample holder (a cuvette with a path length of 1 cm), and its absorbance spectrum was generated. The

position of the peaks corresponding to the electronic transition and the bandgap were also obtained from the wavelength at which the absorption edge occurred. Thermo Scientific Evolution One plus UV-Vis spectrophotometer was used.

3.10.2 FT-IR Characterization

The instrument was first turned on and allowed to warm up; it was then calibrated using standard reference, and the background scanning was obtained by scanning an empty sample holder to account for atmospheric interference. The nanoparticles were placed in a sample holder then scanned at a wavelength of 400-4000 cm^{-1} to obtain the spectrum, which was analyzed to determine the functional group present in the fingerprint and functional group regions. The data obtained was analyzed with the help of a standard library to identify the functional groups present in the sample. The Shimadzu IR spirit model was used for analysis.

3.10.3 XRD Characterization

The nanoparticles were grounded into fine powder using a pestle and mortar. The fine powder of nanoparticles was loaded into the XRD sample holder. X-ray beams were directed onto the sample. Spectrum of intensity against 2 theta shows the crystallographic reflection orientation of the X-ray on the nanoparticles. The data obtained was analyzed with Origin software and compared with JCPDS data base card. The crystal size of nanoparticles was computed using the Debye Scherrer equation. The XRD data were obtained from ARL EQUINOX 100 at 40 V, 0.9 mA, at a scanning range of 20 º-100 º for 240 seconds.

3.10.4 Morphological and EDS Characterization

The sample was loaded onto a carbon stick and run at 20 kV and 50 kV. The images obtained were analyzed to determine the distribution of size and surface morphology of Ag-doped ZnO nanoparticles. The elements present in the nanoparticle sample and their atomic absorption percentages were analyzed with Energy Dispersive Spectroscopy (EDS). The surface morphology of nanoparticles were analyzed using SEM Phenom VEGA3 TESCAN model.

3.10.5 PL Characterization

The solid Ag-doped ZnO was dissolved in deionized water. The dissolved nanoparticles were loaded in a cuvette for scanning. An excitation wavelength of 300

nm was selected and laser lamp was used to excite nanoparticles. The spectrometer disperses the emitted light onto a detector. The light emitted by NPs after excitation was measured. A photoluminescence spectrum was recorded showing the strength of emitted light as a function of a wavelength.

3.11 Validation

Citrus reticulata capped ZnO and Ag-ZnO nanoparticles were successfully synthesized. The nanoparticles obtained were in powder form as shown in figure 3.1.



Figure 3.1: The Ag-ZnONPs synthesized using green synthesis method

The powder nanoparticles were characterized to determine the optical, structural, morphological and luminescence properties.

3.12 Research design

This research used experimental design to investigate the effects of capping agents, different concentration of dopant (0.1, 0.25, 0.5, 0.75, 1.0, 1.5 and 2% of Ag dopant) and effects of growth temperature at 25, 30, 40 50,60 and 70 ℃ on structural, optical and morphological properties of ZnONPs and Ag-ZnONPs. Green synthesis method was use to synthesized nanoparticles.The powder nanoparticles obtained were then characterized using XRD, FT-IR, UV-Vis, PL and SEM. Data obtained was analyzed by comparing the average crystal size, bandgap energy and particle size at varying concentration and growth temperature.

3.13 Summary

This chapter extensively discussed the materials used, the synthesis method as per the objectives and the characterization techniques employed to analyze data. The

nanoparticles was synthesized via green synthesis method and the characterization techniques employed include FT-IR, UV-Vis, XRD, PL and SEM.

CHAPTER FOUR
RESULTS AND DISCUSSION

4.1 Introduction

This chapter discuss the results obtained from FTIR, XRD, UV-vis, PL and SEM of ZnO and Ag-ZnONPs prepared using *Citrus reticulata* peel extract. The results have been discussed according to the specific objectives

4.2. Effects of *Citrus reticulata* peel extract on silver- doped zinc oxide nanoparticles

Chemicals methods for synthesizing nanoparticles are sol-gel, chemical precipitation, thermal decomposition, micro emulsion and polyol method (Dhand *et al.,* 2015). Despite being able to achieve the desired properties of nanoparticles, these methods are considered harmful to the environment due to wastes generated and many toxic chemicals used in the synthesis process such as sodium borohydride ($NaBH_4$), which has been extensively exploited in chemical methods as a reducing agent. Alternative methods have been developed to ensure the nanoparticles are synthesized without the risk of harming the environment. The synthesis method involve the use of plant extracts such as leaves (Shafey, 2020), fruits (Ahmed *et al*., 2018) and stems (Karthiga, 2018). The plant extract acts as a capping and reducing agent for the development of nanoparticles. The following are the characterization of citrus reticulate capped Ag-ZnONPs.

4.2.1 The FT-IR Analysis

The FT-IR spectra of the plant extract capped and uncapped ZnO is shown in Figure 4.1. It was recorded in the range of 400-4000 cm^{-1}. The main bands were observed in both fingerprint and functional groups region. In both spectra, the carbonyl group dominated due to the fact that the precursor used was zinc acetate dihydrate.

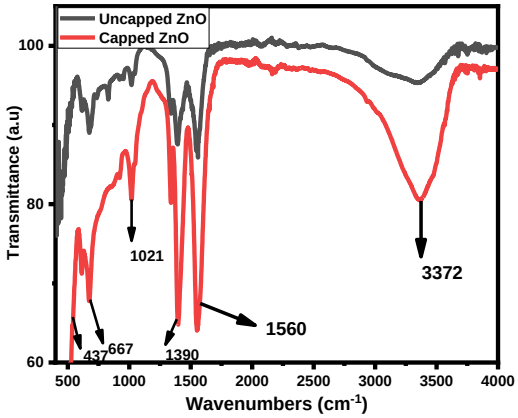


Figure 4.1: The FT-IR spectra of Plant extracts capped ZnONPs and uncapped ZnONPs nanoparticles

The stretching frequency of O-H for uncapped ZnONPs were broader compared to capped ZnONPs and were observed at 3370 and 3372 cm^{-1} respectively. The peak at 2081 cm^{-1} that was only observed in uncapped ZnONPs was attributed to asymmetric and symmetric stretching NO_2. The typical FT-IR peaks for ZnO were observed at 476 and 437cm^{-1}, due to the optical transverse mode of ZnO. The stretching vibration belonging to C=O of acetate group was observed at range of 1560 to 1390 cm^{-1}. The FT-IR spectrum for uncapped ZnONPs had a lot of noise and the peaks were not as sharp compared to that of capped ZnO. When ZnO was prepared by biological methods the stretching vibration between 450-540cm^{-1} confirmed the presence of metal oxide nanoparticles (Anbuvannan *et al.*, 2015)

Figure 4.2 shows the FTIR spectra obtained when ZnO was doped. The peaks were sharp, narrow, high intensities and shift slightly to lower frequencies compared to those of undopped ZnONPs.

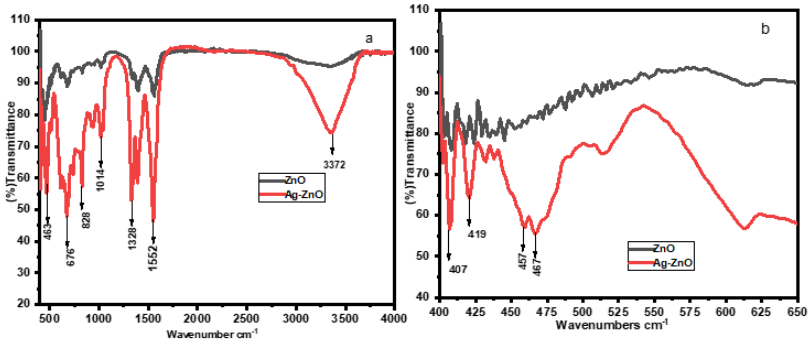


Figure 4.2: FT-IR spectra of ZnO and Ag-ZnO at (a) 400-4000 cm^{-1} and (b) 400-650 cm^{-1}

The broad peak at 3372cm^{-1} shows the stretching frequency of O-H which was at a lower frequency than that of uncapped ZnO. The peaks at 1552 and 1328 cm^{-1} showed the presence of stretching frequencies of carboxylic groups mainly C=C and C-O respectively. The stretching phase of C-O was observed at 1014 cm^{-1} and a bending phase of C-H at 828 cm^{-1}. The stretching frequency of metal oxide was observed at 463 cm^{-1} which was slightly lower than what was observed in uncapped ZnO. Minor and major shift were observed when ZnONPs were doped with transitional metals (Sagadevan *et al.*, 2017).When Ag is incorporated into ZnO structure it induces distortion due to the alteration of local bonding environment, this was observed when Ag-ZnO and ZnO were synthesized via hydrothermal and co-precipitation (Ali *et al.*, 2024). The FT-IR spectra showed more prominent vibration mode with Ag-ZnO than for ZnO which clearly indicates that strong doping occurred.

4.2.2 The XRD analysis

Figure 4.3 shows the XRD pattern of pure zinc oxide synthesized with and without *Citrus reticulata* peel extract. In both cases, the pattern depicts peaks of ZnO nanoparticles only, indicating that there were no impurities in the sample.

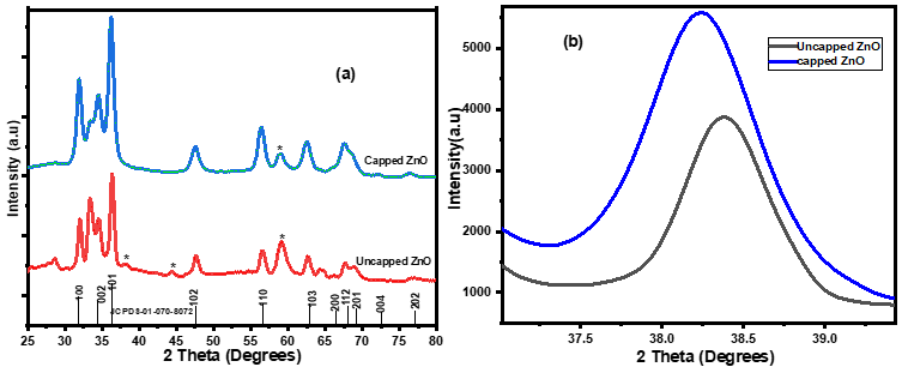


Figure 4.3:(a) XRD pattern of capped and uncapped ZnONPs and (b)peak (101) of capped and uncapped ZnONPs

When ZnO was doped with silver, the structure of ZnO was maintained in the capped sample. The additional peaks of low intensity were observed at 2θ at 40.28º, 44.43º and 62.34º which corresponded to (111) and (200) in JCPDS card number 84-1108 as shown in Figure 4.4.

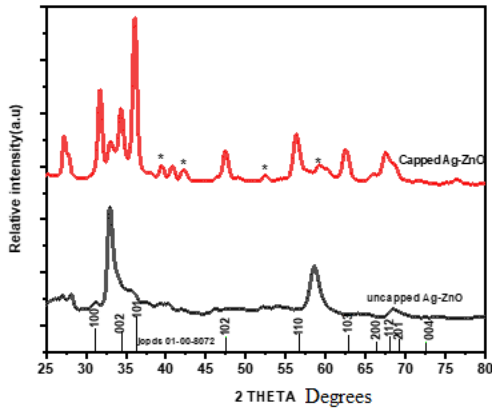


Figure 4.4: The XRD pattern of capped and uncapped Ag-ZnO nanoparticles

The other two peaks were likely as a result of impurities from citrus peel extract. These peak are associated with a face centered cubic phase of metallic silver (Phan & Nguyen, 2017). Crystalline silver luster was formed as indicated by the appearance of Ag peak in the XRD pattern of the nanoparticle (Khosravi-Gandomani *et al.*, 2014). The same pattern was observed when 1% and 0.75% silver were added to ZnONPs and two extra peaks appeared at angles of 38.28˚ and 38.46˚ respectively (Jobe *et al.*, 2022). The XRD pattern for Ag-ZnO prepared without peel extract changed. This can be associated with local strain or defects. This also shows the importance of using capping agents when preparing doped nanoparticles. The doping element has larger ionic radius (1.22Å) than Zn^{2+} (0.74 Å). Therefore Zn^{2+} is replaced at the substitution sites of ZnO crystal lattice and results in a decrease in peak position (Kareem *et al.*, 2022). Ag^{+} ions have the ability to occupy both the lattice and interstitial sites of ZnO just like other monovalent dopants.

Bragg's law equation, shown in equation 4.1 was used to calculate the d spacing

$$\boldsymbol{n\lambda = 2dsin\theta} \quad (4.1)$$

Where n is diffraction order, λ is wavelength and d is the spacing between miller indices h, k, l. In the hexagonal wurzite structure of ZnO the d spacing is related to a and c lattice constants and miller indices. Equation 4.2 shows the relationship between lattice constant a,c and d.

$$\frac{\mathbf{1}}{\boldsymbol{d_{hkl}^2}} = \frac{\mathbf{4}}{\mathbf{3}}\left(\frac{\boldsymbol{h^2+hk+k^2}}{\boldsymbol{a^2}}\right) + \frac{\boldsymbol{l^2}}{\boldsymbol{c^2}} \quad (4.2)$$

The lattice constant a=b in hexagonal wurzite, at plane [100] it is given by equation 4.3

$$\boldsymbol{a = \frac{\lambda}{\sqrt{3}\,\sin\theta}} \qquad (4.3)$$

The lattice constant c is given by equation 4.4 at plane [002] (Cullity, 1956)

$$\boldsymbol{c = \frac{\lambda}{\sin\theta}} \qquad (4.4)$$

Table 4.1 summarizes the interplanar spacing (d_{hkl}) calculated from XRD and are compared with JCPDS data card corresponding (h k l) planes and full width at half maximum values.

Table 4.1: **Calculated d-spacing and the standard JCPDS d-spacing of capped and uncapped ZnO with their FWHM**.

h k l		**100**	**002**	**101**	**102**	**110**	**103**
2θ uncapped ZnO		31.902	34.53	36.42	47.83	56.62	62.61
2θ Capped ZnO		31.81	34.47	36.29	47.44	56.53	62.32
d_{xrd} Uncapped ZnO in Å		2.8029	2.5954	2.4649	1.9001	1.62427	1.48250
d_{xrd} capped ZnO in Å		2.81087	2.5998	2.47348	1.91489	1.62664	1.48870
d_{JCPDS}		2.81155	2.6015	2.47352	1.90948	1.62325	1.47609
% Contraction	Uncapped ZnO	0.30516	0.2348	0.34849	0.48662	-0.0632	0.43462
	Capped ZnO	0.02418	0.0653	0.00167	0.28327	0.20933	0.85442
FWHM	Uncapped ZnO	0.5755	0.7149	0.61073	0.7133	0.80383	0.77955
	Capped ZnO	0.74037	0.7916	0.82459	0.9943	0.95741	0.9999

The lattice constant a=b for ZnO was 3.2365 Angstroms and c=5.1908 Angstroms, c/a=1.6038 and the diffraction peaks obtained from XRD corresponding planes (100), (002), (101), (102), (110), (103) are consistent with the JCPDS data of ZnO. The lattice constant for ZnO synthesized with *Citrus reticulata* peel extract was a=b= 3.2457Å and c= 5.1996Å, c/a=1.602. The values for FWHM for pure ZnO were varying when

compared to that of ZnO prepared with peel extract. Similar results were observed when different methods are used to synthesize ZnO nanoparticles and it matched with JCPDS card number 01-070-8072 (Srithar *et al*., 2017).

Table 4.2 shows the summarized lattice parameter d and FWHM of Ag- doped ZnO nanoparticles.

Table 4.2: Calculated d-spacing and FWHM (Å) of Ag-ZnO nanoparticles.

h k l	**100**	**002**	**101**	**111**	**200**	**102**	**110**	**103**
2θ (º)	32.14	34.78	36.52	41.913	43.214	47.87	56.79	63.86
d_{xrd}	2.782	2.577	2.458	2.153	2.091	1.8987	1.6198	1.4564
FWHM	0.5778	0.6467	0.6062	0.99682	0.99597	0.77067	0.90331	0.97709

The Crystallite sizes were calculated using Derby-Scherrer equation 4.5:

$$\boldsymbol{D = \frac{K\lambda}{\beta hkl cos\theta}} \quad (4.5)$$

Where λ is the wavelength of the radiation, (1.54060Å for Cu Kα radiation) K is the constant equal to 0.9, and β_{hkl} is the peak width at half maximum intensity, $\theta$is the peak position, and D is the crystalline size in angstroms. The values obtained are summarized in Table 4.3.

Table 4.3: Calculated crystal sizes (D) of uncapped ZnO and capped ZnO & Ag-ZnO nanoparticles

h k l	**100**	**002**	**101**	**102**	**110**	**103**
D ZnO	14.36nm	11.64nm	13.69nm	12.18nm	11.28nm	11.93nm
D Capped ZnO	11.16nm	10.51nm	10.19nm	8.73nm	9.42nm	9.29nm
D Ag-ZnO	14.31nm	12.87nm	13.80nm	11.28nm	10.00nm	9.53nm

The average crystallite size for pure ZnO was 12.51 nm, for capped ZnO was 9.88 nm and for capped Ag-ZnO was 11.97 nm. Crystallite size is different from particle sizes and is presumed to be the size of diffraction domain (Khosravi-Gandomani *et al.*, 2014). Capping of nanoparticles leads to reduction in size making them more stable (Bindu & Thomas, 2014).

When samples were annealed the XRD pattern became smooth and there was no noise indicating that there was no impurity and all the hydroxide that might have been present in the 'as-prepared' samples were all removed during annealing. Figure 4.5 shows the XRD pattern obtained.

.

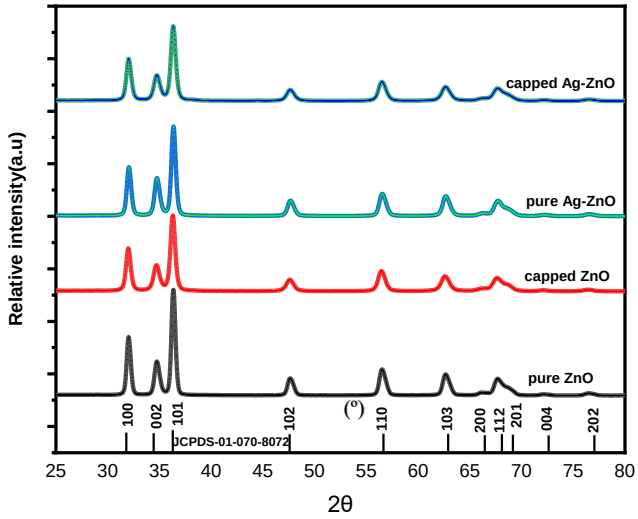


Figure 4.5: The XRD pattern of annealed pure and Ag-ZnONPs at 450°C

The peaks were sharp and strong compared to 'as- prepared', indicating that the annealed samples were of higher crystalline than the 'as-prepared'. The crystal size increase from 13.69 to 18.65 nm at plane [101] for the pure ZnONPs. The increase in grain size after annealing indicates a significant growth of grain size due to displacement of atoms to the suitable position to unite with the adjacent particles thus large grain (Javed *et al*., 2016). The XRD pattern for both pure and capped ZnO nanoparticles maintained the hexagonal wurzite structure of ZnO and Ag-ZnO nanoparticles. Figure 4.5 shows the XRD pattern of annealed pure and Ag-ZnO nanoparticles. The Ag patterns disappeared when the samples were annealed; at high temperatures, any impurities, mainly the hydroxides are vaporized. The pure ZnO pattern observed indicates that effective doping took place and all the Ag^{+} ions occupied the interstitial sites or were segregated into the non-crystalline region and the ZnO lattice structure was conserved (Kim *et al*., 2011).

Figure 4.6 shows the XRD peaks at plane (101). It can be noted that citrus extract had a major effect on structural properties of both pure and doped ZnO nanoparticles.

When citrus was used to prepare ZnO nanoparticles the intensity of the peak decreased.

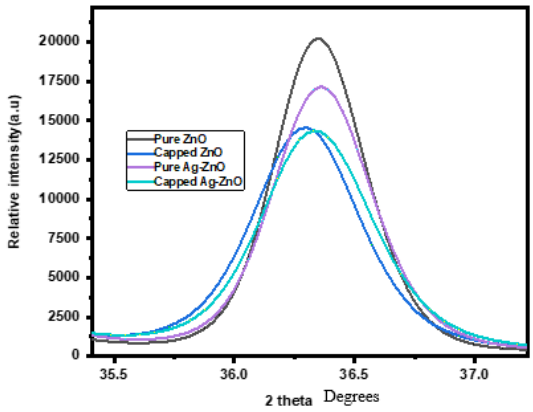


Figure 4.6: The XRD pattern of peak (101)

Doping ZnO with silver decreases the crystalline properties of ZnO due to low peak intensity when compared to that of pure ZnO. The Ag-ZnO and ZnO NPs capped with peel extract patterns were broad when compared to other patterns. The patterns also tend to shift to lower angle, those uncapped shift to a higher angle. The FWHM was higher for capped nanoparticles than those for uncapped, Table 4.1 and 4.2.

Capping agents are expected to lower the crystal size of nanoparticles. Javed *et al*.(2016) synthesized ZnO using polyethlene glycol and polyvinyl pyrrolidone as capping agents and in both cases, the crystal size reduced when compared with uncapped nanoparticle (Javed *et al.*, 2016). This might be because the capping agents diffused onto the surface of ZnO therefore inhibiting the diffusion of growth species and forming the surrounding solute atom onto the surface of growth.

The dislocation density δ represents the quality of defects in the sample. It is defined as the length of dislocation lines per unit volume of the crystal and is calculated using equation 4.6.

$$\boldsymbol{\delta = \frac{1}{D^2}} \quad (4.6)$$

Where D is the crystal size. The dislocation for each nanoparticle was calculated, Table 4.4 shows the dislocation density of the ZnO and Ag-ZnO nanoparticles.

Table 4.4: **Dislocation density ($\times 10^{-3}$ nm^{-2}) of uncapped ZnO and capped ZnO & Ag-ZnO nanoparticles**

h k l	**100**	**002**	**101**	**102**	**110**	**103**
δZnO	4.84	7.38	5.34	6.74	7.86	7.03
$\delta ZnO\ capped$	8.03	9.05	9.63	13.12	11.27	11.59
$\delta Ag - ZnO$	4.88	6.04	5.25	7.86	10.00	11.01

The dislocation density of pure ZnO nanoparticles was 6.53×10^{-3} (nm)$^{-2}$. The ZnO nanoparticles that were prepared with *Citrus reticulata* peel extract had dislocation density of 10.44×10^{-3} (nm)$^{-2}$ and that of Ag-ZnONP's was 7.50×10^{-3} (nm)$^{-2}$. Dislocation density increased when the nanoparticles were doped with Ag. When capped with *Citrus reticulate* the dislocation density increased tremendously. Rabell *et al.* (2021) observed a similar pattern of dislocation density when pure ZnO was doped with silver for photo-electrocatalysis process (Rabell *et al.*, 2021).

To estimate the lattice strain, Williamson and Hall equation was used.The XRD pattern of as prepared Ag-ZnONP's without *Citrus reticulata* peel extract deviated from the standard and this can be associated with the stress and strain. When the nanoparticle was annealed at 450℃ the pattern matches that of standard. The strain was calculated using equation (4.7)

$$\boldsymbol{\varepsilon = \frac{\beta_{hkl}}{4\,tan\theta}} \quad (4.7)$$

Where ε is the strain and β_{hkl} is the FWHM and θ is the peak position. The XRD pattern had only two peaks that were used to calculate crystal size using equation (4.5) and lattice strain using equation (4.7). Table 4.5 summarizes the crystal size, FWHM and strain obtained from the pattern.

Table 4.5: **Calculated strain of uncapped Ag-ZnO nanoparticles**

2θ degrees	**FWHM(Å)**	**D(nm)**	**ε**
33.057	0.72306	11.46	0.01063
58.638	1.33202	6.84	0.010348
68.673	1.5411	6.24	0.009844

The crystal size was directly proportional to strain, this result from atomic movement when agglomeration takes place for large grain to be obtained.

4.2.3 Photoluminescence spectroscopy

Figure 4.7 shows the PL spectra of pure and *Citrus reticulata* capped ZnO and Ag-ZnO nanoparticles. The PL measurements were performed at standard temperature at an excitation energy of 320 nm. PL spectrum of ZnO nanoparticles has two emission bands, near band edge (NBE) which is located at the UV region between the collision process of exciton-exciton. The second emission originates from the ZnO defects that lead to electron- hole recombination and is normally observed in the visible region. In Figure 4.7 it was observed that pure ZnO nanoparticles had the highest emission.

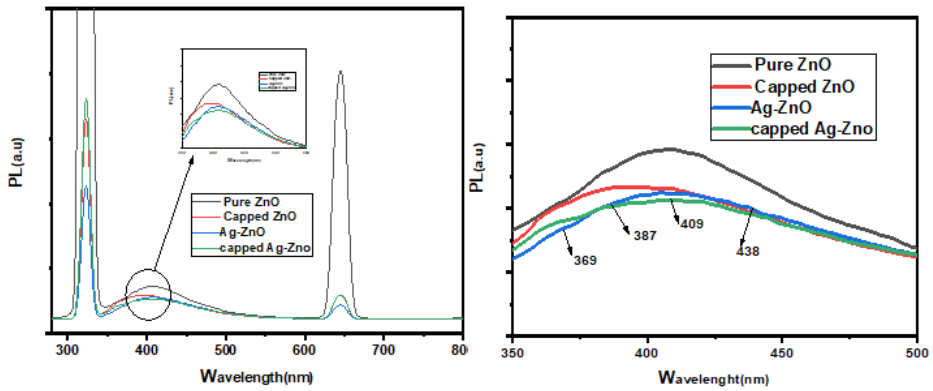


Figure 4.7: The PL spectra of pure and capped ZnO and Ag-ZnO nanoparticles

When nanoparticles were doped, the emission band decreased and shifted towards the near band edge. The emission band for capped ZnO was observed at 383 nm and that of pure ZnO was observed at 409 nm. When doped with Ag the intensity of the peaks decreased, and enhanced UV emission was observed at 369 nm as compared to that of pure ZnO, this is as a result of silver enhancing the exciton recombination thus improving the optical properties of ZnO. Doping ZnO nanoparticles with Ag, leads to the growth of grain which then results in smaller non radiative relaxation rates over the surface states hence better exciton diffusion through the crystal and higher UV PL intensities.

4.2.4 UV-Vis Analysis

The bandgap energy of pure and *Citrus reticulata* capped ZnO and Ag-ZnO nanoparticles was determined with Evolution One Plus UV-vis in the range of 200-800 nm at an ambient temperature. Figure 4.8 shows the UV-vis spectra of capped and pure ZnO.

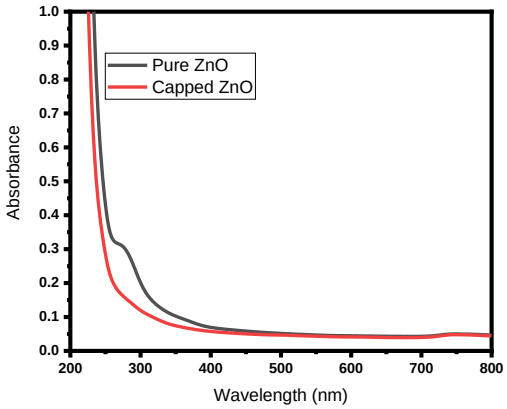


Figure 4.8: UV-vis spectra of pure and capped ZnO nanoparticles

The capping agents increased the bandgap energy from 3.34 to 3.52 eV.The same observation was also made by when ZnO was capped with polyvinyl pyrrolidone and polyethylene glycol (Javed *et al*., 2016). Capping agents interfere with electronic and structural properties of material thus altering the energy levels of the conduction and valence bands. The optical properties of nanoparticles are greatly influenced by the size of nanoparticles. Bandgap increases with a decrease in particle size (Campisi *et al.*, 2016). This can be explained using quantum mechanics; the thickness of the band becomes thinner when the number of overlapping energy levels decreases as the particle size reaches a nanoscale (M. Singh et al., 2018).

Tauc's equation (4.8) was used to estimate the optical bandgap of the sample.

$$(\boldsymbol{\alpha h v})^{\boldsymbol{\gamma}} = \boldsymbol{A}(\boldsymbol{h v} - \boldsymbol{E_g}) \quad (4.8)$$

Where α is the absorption coefficient, h is the planks constant, v is the frequency of the incident photon's, A is proportionality constant, γ denote the nature of electronic transition and can be ½ or 2 indirect and direct transition respectively, E_g is the bandgap energy. The Tauc's equation is compared with straight-line equation where Y= m(x), when y is equal to zero then 0=A(hv- E_g), the bandgap energy is obtained directly from extrapolating the linear region of the plot onto the x-axis. The bandgap

energy of nanoparticles increased due to quantum effect when compared with bulk ZnO.

When Ag was added to ZnO the bandgap energy increased from 3.34 to 3.85 eV for uncapped nanoparticles and from 3.52 to 3.68 eV for *Citrus reticulata* capped Ag-ZnO nanoparticles as shown in Figure 4.9.

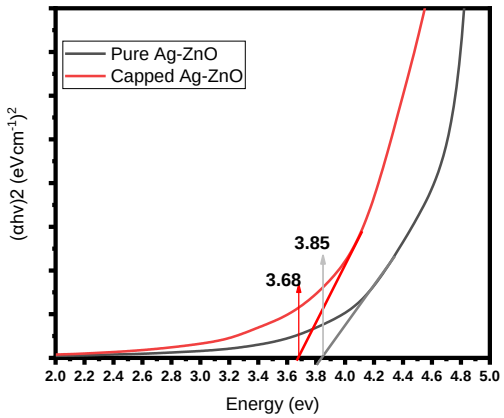


Figure 4.9: Tauc's plot of pure and capped Ag-ZnO nanoparticles

When capping agent was added to doped ZnO nanoparticles, the bandgap energy tend to decrease as compared to uncapped doped nanoparticles. Nanoparticles are also known to provide discrete energies instead of continuous energy, thus, the increase in band gap energies.

The refractive index of semiconducting material plays a key role in their optical and electrical properties. Equation 4.9 was used to calculate the refractive index of capped and uncapped ZnO and Ag-ZnO nanoparticles.

$$\boldsymbol{n = \frac{1}{T} + \sqrt{\frac{1}{T-1}}} \quad (4.9)$$

Where T is the transmittance, semiconductors material with high refractive index traps incident ray (Bolorinwa *et al* 2017). A plot of refractive index against photon wavenumber was obtain as shown in Figure 4.10.

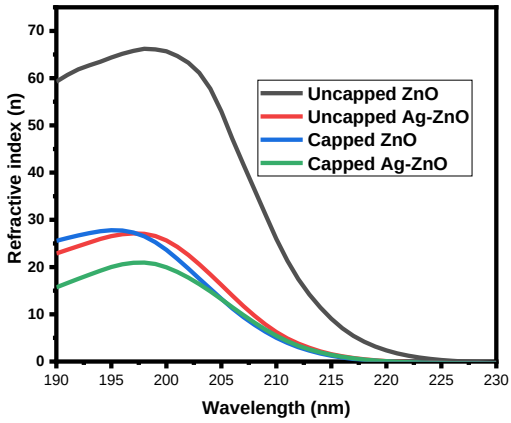


Figure 4.10: Refractive index of capped and uncapped ZnO and Ag-ZnO nanoparticles

The refractive index decrease drastically from shorter to longer wavelength (190 to 230 nm), similar results were obtained by (Kayani *et al*., 2020).Uncapped ZnO nanoparticles had the highest refractive index at a wavelength of 199 nm, the presence of capping agents mainly plant extract tends to bind on the surface of nanoparticle and create dielectric shell which reduces the overall refractive index.

Real and imaginary parts of dielectric constant were calculated using equation 4.10 and 4.11 respectively. The data obtain were plotted against wavelength and a plot in Figure 4.11(a) and (b) were obtained.

$$\boldsymbol{\varepsilon_r = n^2 - k^2} \quad (4.10)$$

$$\boldsymbol{\varepsilon_i = 2nk} \quad (4.11)$$

Where n is the refractive index and k is the extinction coefficient which describe how strongly a material absorbed light at certain wavelength. The dielectric constant around the bandgap energy of ZnO increase and this can be attributed to strong interaction between an electron and a photon. Both real and imaginary dielectric constants follow the same pattern. The values of real dielectric constant was high compared to imaginary dielectric constant. The results obtain are in agreement to those previous reported by (Kayani *et al*., 2020). Real dielectric constant measure the amount of energy stored in material when exposed to electric fields, while imaginary measure the amount of energy lost or converted to heat. Capped Ag-ZnO nanoparticles

have the lowest imaginary dielectric constant and medium real dielectric constant making it suitable for potential applications in optoelectronics equipment.

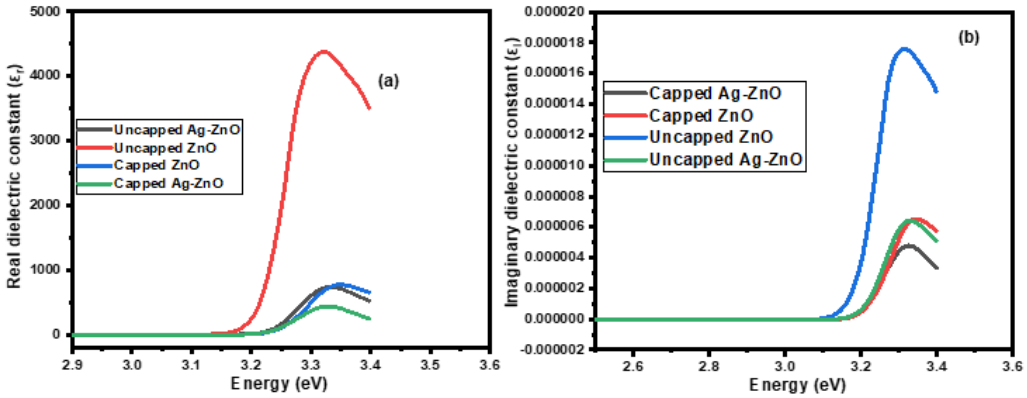


Figure 4.11: (a) Real and (b) Imaginary dielectric constant

4.2.5 Morphology

Figure 4.12 show the SEM images of pure and capped ZnO nanoparticles, having similar scale bar of 1μm equals to 1000 nm, accelerating voltage of 20.0 kV and magnification of 4000x and different view field. Capping agents often leads to irregular and aggregated morphologies (S. Chen et al., 2020). The SEM image obtained from *Citrus reticulata* capped ZnO nanoparticle was opposite of the expected results. Capped ZnONPs displayed a more defined, rod-like morphology with smooth surface. This means that *Citrus reticulata* peel extract used as capping and reducing agent played a role in directing crystal growth. The presence of polyphenols and flavonoids may have suppress random aggregation. In contrary the uncapped ZnONPs showed significant aggregation and less define polyhedral like shape nanoparticles due to absence of stabilizing organic molecules during preparation. This suggest that capping agent influence the morphology and orientation of nanoparticles which then affects its application. Uncapped nanoparticles cluster forming large particles. The increase in particle size is consistent with data obtained in XRD.

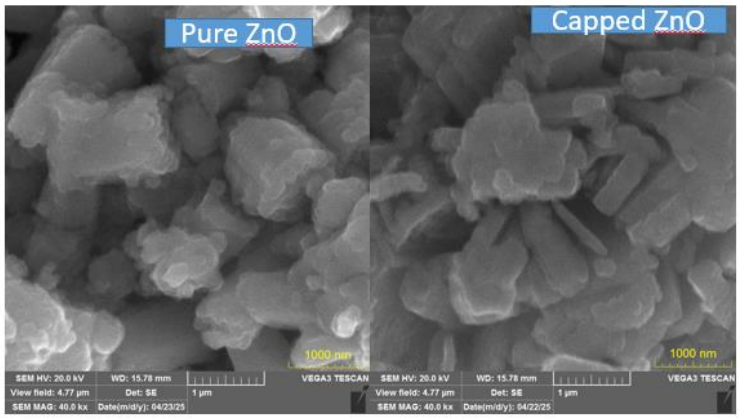


Figure 4.12:The SEM images of pure and capped ZnONPs

When pure and capped ZnO was doped with silver and analyzed under the same condition the SEM images obtained is shown in Figure 4.13. Uncapped Ag-ZnO had loosely agglomerated, irregular and roughly spherical shape nanoparticles. Visible gaps between clusters are observed this might have result from insufficient capping causing uncontrolled growth (S. Chen *et al*., 2020). Contrary to this, capped Ag-ZnONPs had partially fused, more continuous and less void space images which suggest that high reactivity during the synthesis process.

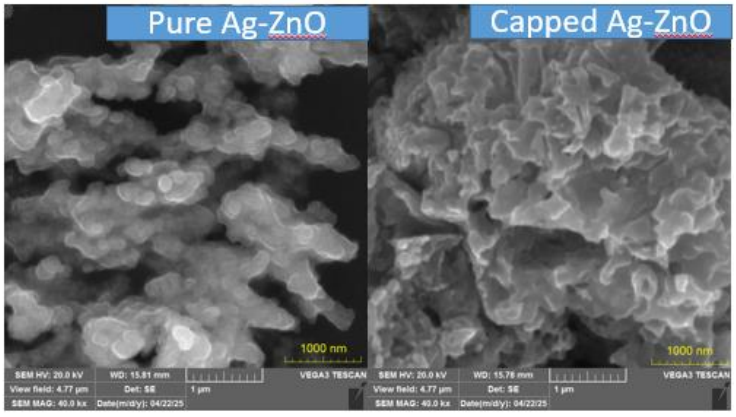


Figure 4.13: SEM images of capped and uncapped Ag-ZnONPs

4.2.6 Elemental and chemical analysis

The EDS analysis of capped and uncapped ZnO is shown in Figure 4.14. It is evident that the spectra contained the desired elements of Zn and O. The presence of carbon and silicon can be attributed to glass substrate. The traced amount of sodium was at high concentration in capped ZnO which might have results from the elemental composition of *Citrus reticulata* peel extract. The traced sodium has negligible structural and optical properties of nanoparticles.

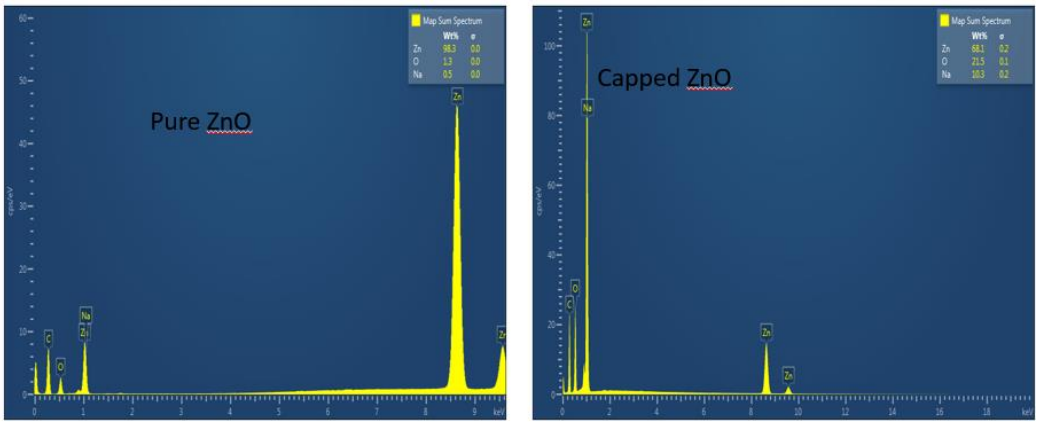


Figure 4.14: EDS spectra of capped and uncapped ZnO nanoparticles

4.3 Effects of Ag doping concentrations on structural and optical properties of *citrus reticulata* capped ZnO nanoparticles

The ZnO is a semiconductor compound used in making the photoanode of solar cells as a result of its large bandgap of 3.37 eV and excitonic binding energy of 60 meV (Sáenz-Trevizo *et al.*, 2016). The impurity content, shape and size affect the optoelectronic behavior of nanostructured semiconductors and thus there is a need for an in-depth understanding of the fabrication of efficient materials. In recent years, doping has been reported to alter the luminescence properties of ZnO. This has led to either blue or red shift at near band edge (NBE) emission and in their visible emission (Wang *et al*., 2016). Dopants like silver are known to have a great impact on the luminescence properties of nanostructured semiconductors (Hosseini *et al*., 2015).

This study reports a low cost, facile, green, one pot method for synthesizing Ag-ZnONPs using *Citrus reticulata* peel extract without any additional reducing agent, acids or organic solvents. The effects of different Ag doping concentrations on the material properties of *Citrus reticulata* capped ZnONPs was studied in details to obtained the optimum conditions for the growth of the Ag-ZnONPs for photovoltaic applications.

4.3.1 The X-ray diffractions (XRD) analysis

The XRD pattern for Ag-ZnO is shown in Figure 4.15 and it exclusively displays the hexagonal wurtzite structure of ZnO which matches that of JCPDS file (no. 01-070-8072).

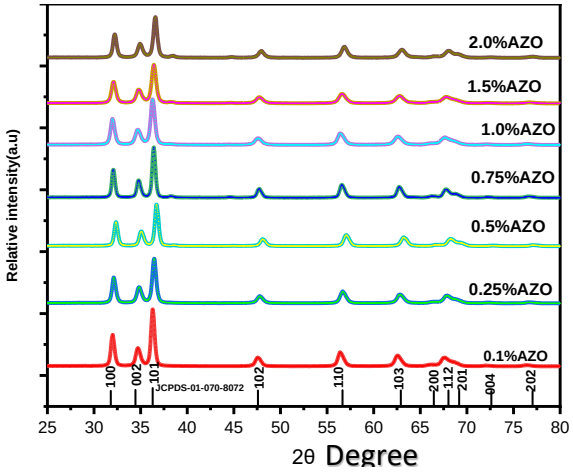


Figure 4.15: XRD pattern of different mol % concentration Ag-doped ZnONPs

The pattern depicts only ZnO peaks. This means that successful doping was achieved with hydroxyl-free *Citrus reticulata* peel extract. There were no peak patterns for Ag, all were incorporated into the ZnO structure. They all occupied the interstitial site of the ZnO nanoparticles or were partitioned into the nano crystalline region within the grain boundaries at the same time conserving the original ZnO lattice structure (Ko *et al*., 2012). The cell parameter a and c were calculated from peak (100) and (002) respectively. The results matches that obtained by (Ranjithkumar *et al.*, 2021)

The crystallite size and d spacing were calculated using the Debye-Scherrer formula (Bett & Kiprotich, 2024) and Bragg's equation (Abdulrahman & Haddad, 2020) respectively for the planes [100,002,101,102,110,103] and the results were summarized in Table 4.6.

The Bragg's equation is given by equation 4.12.

$$\boldsymbol{n\lambda = 2dsin\theta} \quad (4.12)$$

With λ being the wavelength, n is interger normally 1 and θ is the reflected angle, d is the crystal spacing. The Scherrer formula was used to calculate the crystal size of the Ag-ZnONPs. Crystal size characterization is important in determining the nature of particles as either small crystalline (soft), thermal behavior, diffusion and large crystalline which indicates hard materials (Akbari *et al.*, 2011).

The Scherrer equation 4.13 was used to calculate the crystal size

$$\boldsymbol{D = \frac{K\lambda}{\beta COS\theta}} \quad (4.13)$$

D is the crystal size, K Scherrer constant (0.9), β denotes full width at half maximum for each plane peak and λ is the wavelength which was (1.5406 Å) for Cu anode x-ray tube.

In Table 4.6, it was observed that the d-spacing increased when silver was introduced to ZnO structure. When dopants were added, the d-spacing increased rapidly, and on addition of higher mol % of silver dopant, the spacing decreased gradually.

Table 4.6: Effects of different concentration of silver dopant on the d-spacing and lattice parameters a and c.

Sample (mol % of Ag)	**2θ degrees for different planes**						**Average d-spacing**	**a**	**c**
	100	002	101	102	110	103			
0.0	31.52	34.52	36.17	47.48	56.36	62.49	2.129	3.084	5.192
0.1	31.79	34.54	36.12	47.42	56.29	62.41	2.162	3.247	5.198
0.25	31.10	34.72	36.33	42.67	56.59	62.73	2.191	3.318	5.163
0.5	31.81	34.96	36.61	47.98	56.95	62.93	2.134	3.245	5.129
0.75	31.93	34.67	36.29	47.60	56.51	62.65	2.142	3.233	5.129
1.0	31.85	34.59	36.17	47.48	56.36	62.49	2.151	3.242	5.182
1.5	31.92	34.66	36.27	47.49	56.49	62.63	2.147	3.235	5.172
2.0	31.78	34.82	36.45	47.81	56.73	62.89	2.141	3.248	5.149

The fluctuation in d-spacing can be associated with a strain defect from varying the concentration of silver. The d- spacing at plane (002) decreases with an increase in concentration of silver. The d-spacing effects were directly proportional to the effects encountered by lattice parameters. The c lattice parameter change from 5.192 Å for undoped ZnO to 5.198 Å when doped with 0.1% of silver. This indicates that doping increases the lattice parameters. When different concentrations were added, it was noted that the lattice parameter c decreased and the smallest value observed was for 0.75%. This stipulates that all the Ag ions had occupied the interstitial site of ZnONPs. The shift in peak position towards the higher 2 theta degree was also observed as the concentration of Ag was added. This is in concurrence with what Sampath *et al.*

observed when ZnO was doped with Ag prepared using Neem leaf extract, Hibiscus and Tulsi (Sampath *et al.*, 2022). This factor is set down to the fact that Ag^{+} has a larger ionic radius (0.126 nm) compared to Zn^{+} (0.074 nm).

The crystal size was calculated using the Debye Scherrer formula (equation 4.10). The average crystal size of nanoparticles is summarized in table 4.7.

Table 4.7: Calculated crystal size (D) and obtained FWHM of varying mol % of silver dopant in Ag-ZnONPs.

	FWHM in degrees at plane						
Ag mol %	**100**	**002**	**101**	**102**	**110**	**103**	**D(nm)**
0.0	0.512282	0.59797	0.52914	0.75748	0.73448	0.87554	15.294
0.1	0.43686	0.57062	0.43902	0.67911	0.66488	0.78343	17.505
0.25	0.45721	0.58684	0.46139	0.69371	0.69204	0.80245	16.77
0.5	0.43651	0.5378	0.45781	0.65871	0.67289	0.77519	17.562
0.75	0.38866	0.47395	0.40253	0.56972	0.58283	0.65679	19.8672
1.0	0.4947	0.6345	0.4903	0.79876	0.73629	0.89034	15.617
1.5	0.52598	0.5920	0.52401	0.79177	0.79402	0.92176	15.239
2.0	0.44006	0.54466	0.47248	0.67631	0.66495	0.77333	17.268

It was noted that the size increased from 15.294 nm to 17.505 nm when pure ZnO was doped with 0.1% Ag. The largest crystal size was found to be 19.867 nm with 0.75% Ag dopant. The crystal size in peak (103) was small in all the samples with peak (100) having the largest crystal size. The crystal sizes were calculated from the average of the first three peaks [100], [002], and [101].

Figure 4.16 shows the variation in crystal size with FWHM for Ag-ZnONPs. From the pattern it was observed that the crystal size was inversely proportional to the FWHM: crystal size$\propto \frac{1}{FWHM}$. When crystal size increased the FWHM decreased.

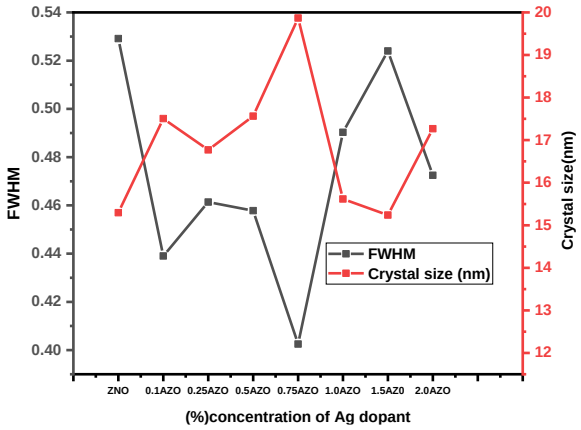


Figure 4.16: Variation of FWHM and crystal size of pure and doped Ag-ZnONPs

These variations were not constant with variation in concentration, with 0.75% dopant having the highest FWHM and lowest crystal size. The increase in crystal size is associated with a decrease in strain. The sudden decrease in crystal size indicates that the addition of silver dopant had reached its maximum level and could not occupy the interstitial sites of ZnO (Amit *et al.,* 2015).

Figure 4.17(a) shows the enlarged diffraction pattern of plane [101] at varying concentration of silver. The plane was used because it had the highest peak as compared to all the other mol% concentrations of the dopant. From the pattern, it was observed that when 0.5% Ag was used, the peak shifted to the higher angle compared to other concentrations.

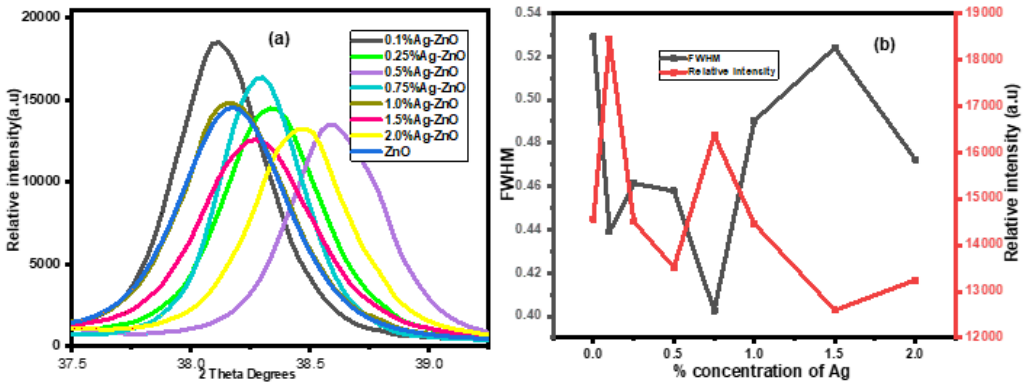


Figure 4.17: (a) **Enlargement image of diffraction plane [101] for pure ZnO and doped Ag-ZnONPs. (b) Variation in FWHM and relative intensity of peak [101] for pure ZnO and various concentration of Ag dopant.**

The highest peak observed was for 0.1% Ag; this showed that the most crystalline particles were observed, when lower concentrations of silver were used. As the concentration of Ag was increased, the peak position shifted towards the lower values. The shift indicates partial substitution of Ag^{+} at the lattice sites of ZnO, which leads to an increase in lattice parameters a and c as expected, but from the results obtained, the c character decreased as the concentration of Ag was added until 0.75%. The c parameter started increasing then decreased; this can be associated with many aspects such as the formation of silver nano-collection and strains depending on how the ZnO interacted with the dopant (Hosseini *et al.*, 2015).The peak intensity increased with a decrease in FWHM, this suggests that the crystallinity of nanoparticles improved (Ungula, 2018). 1.0% had a slight effect from that of undoped ZnO, the intensity of the peak and FWHM were almost similar. In Figure 4.17(b) the variation of concentration with FWHM and relative intensity at plane 101 is displayed. Estimation of strain**,** The Williamson-Hall method was used to calculate the strain. W-H plot was used to determine the crystal size. The broadening caused by crystallite was calculated using the Debye Scherrer equation in equation 4.13. The lattice strain was calculated using equation 4.14

$$\boldsymbol{\varepsilon = \frac{\beta_{hkl}}{4sin\theta}} \quad (4.14)$$

Where ϵ is the lattice strain, β is the FWHM of the XRD peak in radians, and θ is the Bragg angle. Equation (4.15) was used to calculate the strain induced by crystal imperfection and distortion (Bindu & Thomas, 2014)

$$\boldsymbol{\varepsilon = \frac{\beta}{4tan\theta}} \quad (4.15)$$

Where ε is the micro strain and β is the FWHM. Equation (4.16) which is a Williamson-Hall equation was used to calculate the crystal size

$$\boldsymbol{\beta cos\theta = \varepsilon(4sin\theta) + \frac{K\lambda}{D}} \quad (4.16)$$

The equation 4.17 is a function of data which is equal to equation of a straight line given by

$$y = mx + c \quad (4.17)$$

With c being the slope equal to $\frac{K\lambda}{D}$, y equal to $\beta cos\theta$ and ε is the slope. When a graph of $4sin\theta$ on the x-axis and $\beta cos\theta$ on the y-axis is plotted as shown in Figure 4.18, the slope obtained showed the microstrain and the crystal size was calculated from the y-intercept. The strain obtained might have been a result of reduction of lattice parameters observed from the calculation of lattice parameters. Table 4.8 shows the strain obtained by Williamson hall equation for different concentrations of silver.

Table 4.8: Variation of strain with concentration from W-H method

Ag (%)	Strain
0.1	0.00073236
0.25	0.00085902
0.5	0.00403
0.75	0.00348
1.0	0.01718
1.5	0.02881
2.0	0.00414

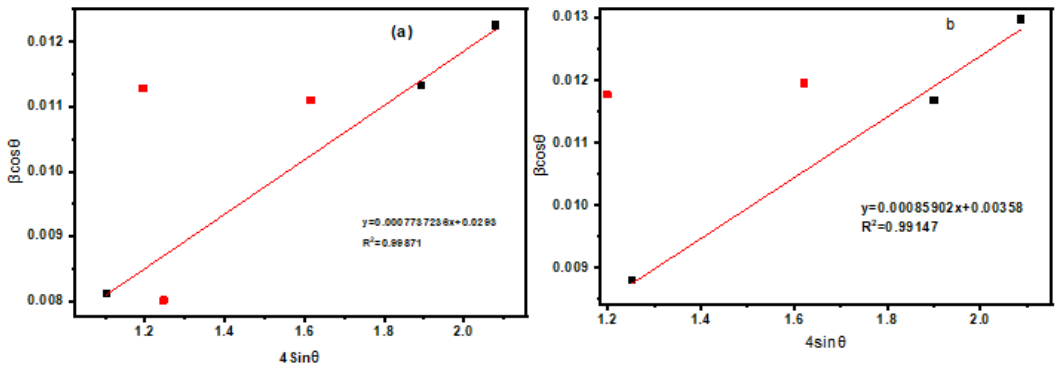


Figure 4.18: Plots of $\beta_{hkl}cos\theta$ versus 4sinθ for (a) 0.1% and (b) 0.25% Ag-ZnO

Figure 4.19 shows the variation of crystal size (D), strain and concentration. It can be observed that D was inversely proportional to strain. $D \propto \frac{1}{\varepsilon}$.

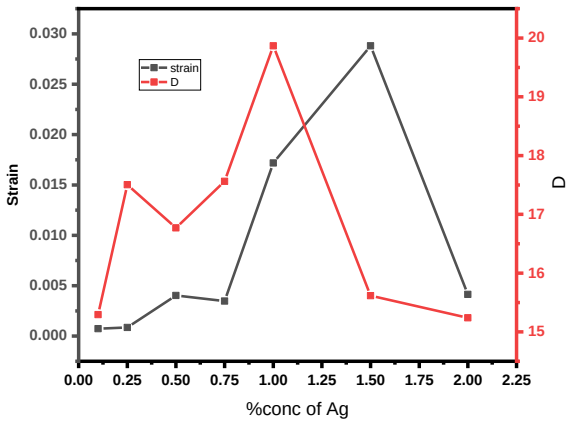


Figure 4.19: Plot showing the trend of crystal size (D) and strain of Ag-ZnONPs

The highest strain was at 1.5% and this can be associated with higher interaction of Ag and ZnO at higher concentration that leads to lattice mismatch and distortion of crystal structure. Nanoparticles with smaller crystal sizes have high surface energy, which caused higher strain, due to surface area to volume ratio. This leads to increase in crystal size with decrease in strain. In theory, if all the strain value agree, they form an angle of forty-five degrees with the x-axis, and they all lie in a straight line (Aly *et al.*, 2016). The strain increased with the concentration of dopant and was inversely proportional to crystal size. 0.1% Ag-ZnO had the smallest strain and 1.5% Ag-ZnO had the highest strain. This might be a result of increase in concentration of Ag caused stressed on the structure of ZnO thus higher strain with an increase in concentration.

4.3.2 The FT-IR analysis

From the pattern in Figure 4.20, the nanoparticles were absorbed in both the fingerprint region and the functional group regions. The pattern gives the details on the functional groups present in the capping, stabilizing and reducing agents used to synthesize nanoparticles.

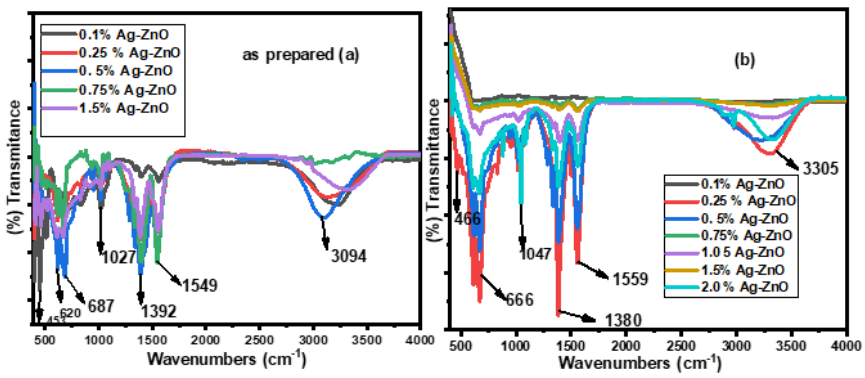


Figure 4.20: FT-IR spectra of annealed and as prepared samples

The pattern obtained showed that O-H was in all prepared samples, but when the samples were annealed, it was observed in 0.25, 0.5, 1.0 and 2.0 % Ag-ZnONPs only. This can be associated with the fact that at high temperature the O-H group could have been vaporized with other water molecules. The presence of O-H group was shown by its absorption peak observed in the range of 2978-3633 cm^{-1} in 0.25, 0.5, 0.75, 1.0, 1.5, and 2.0% Ag. The O-H group of the annealed samples 0.25% Ag-ZnONPs had a very intense and more pronounce peak than in other dopant. The peaks became less intense when the concentration of silver decreased; this is associated with partial substitution of silver ions in the ZnO lattice structure thus causing changes in the bond length (Murtaza *et al.*, 2014). Due to absorption of atmospheric CO_2 peaks were observed at 2968 cm^{-1}.The low absorption mode at 1557 cm^{-1} corresponds to C=C stretching modes. The elongated vibration at 1385 cm^{-1} reveal the O-H bending frequency. At 1042 cm^{-1} a sharp peak was observed which corresponds to C-O whereas, the sharp stretching frequencies at 667 and 619 cm^{-1} correspond to C-H bending deformation vibration. The strong bands at 472 and 410 cm^{-1} are related to the vibration elongation and deformation vibratory of Zn-O (Sorbiun *et al.*, 2018).The unannealed samples peaks shifted to higher wave numbers as compared to annealed samples. 0.1% Ag-ZnO had the strongest vibration elongation of Zn-O for unannealed samples and 0.25% for annealed sample.

4.3.3 Photoluminescence spectroscopy

Figure 4.21 shows the PL spectra of Ag-ZnONPs. ZnONPs were doped with different concentrations of silver from 0.1, 0.25, 0.5, 0.75, 1.0, 1.5 and 2.0%. The samples were analyzed at room temperature at an excitation energy of 300 nm. The study of photoluminescence of nanoparticles is important since it gives important details on the purity and value of material synthesized. The PL spectra of ZnO nanoparticles analyzed at standard temperature usually have two emission bands: at the UV regions which are normally associated with near band edge emission through exciton-exciton collision process and at the visible region. The emission at the visible region is affiliated with electron hole recombination from the deep level emission (DLE) in the band gap caused by intrinsic and extrinsic defects (Bandopadhyay & Mitra, 2015). The incorporation of hydroxyl and carboxylates into the crystal structure during the growth of nanoparticles also contributes to visible region emissions (Kozák *et al.*, 2016).

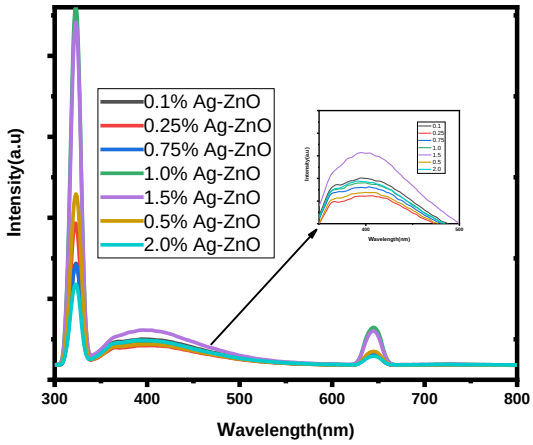


Figure 4.21: PL emission spectra of varying concentration of Ag-ZnO nanoparticles

The graph in Figure 4.21 shows that there was a strong emission in the UV region in all the samples, with a band centered at 323 nm which corresponds to excitonic emission when excited at 300 nm. The nanoparticles doped with 1.0% silver had the highest peak intensity and 2.0%Ag-ZnO nanoparticles had the lowest intensity. The emission peaks at 350-400 nm were also observed. The sample with the highest intensity in the emission spectra was 1.5% Ag-ZnO nanoparticles and 0.25% had the lowest intensity.

Burstein moss effect played a key role in shifting the PL emission spectra of Ag-ZnO nanoparticles to the UV region (Campbell *et al*., 2020). When ZnO is doped with metal, the Fermi level shift to the conduction band C_B. It can be confirmed that the transition moved from the valence band (V_B) to the conduction band (C_B) in the Fermi level instead of from V_B to the bottom of C_B (Saw *et al*., 2015). These changes in the transitions lead to band gap broadening, thus blue shift. The blue shift emission in the UV regions changes with doping concentration. In figure 4.22 it was observed that increase in Ag concentration shifted the emission to a higher wavelength of 364, 365, 364, 366, 368 and 370 nm for 0.1, 0.25, 0.5, 0.75, 1.0, 1.5 and 2.0% Ag-ZnONPs. Similar results were also observed by Ungula *et al*. (2022).

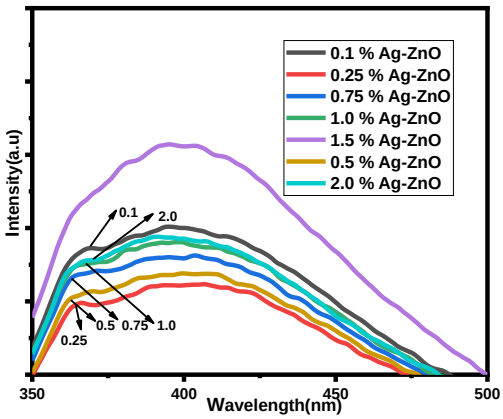


Figure 4.22: The PL emission spectra of Ag-ZnO at varying Ag % mol

4.3.4 Optical Properties

The absorption spectra of pure ZnO and silver doped ZnONPs are shown in Figure 4.23. The analysis was performed at standard temperature in the wavelength range of 200-800 nm. Strong absorption edge in the region between 200-400 nm (UV region) was observed. The absorption occurred as a result of charge transfer from the valence band (VB) to the conduction band (CB) (Wagh *et al*., 2022). Increase in concentration of silver dopant increases the rate of absorption. This change in the absorption peak with concentration of dopants confirms the change in the energy gap (Hosseini *et al*., 2015). The weak absorption starts from 500 and maximum absorptions are observed between 280-400 nm.

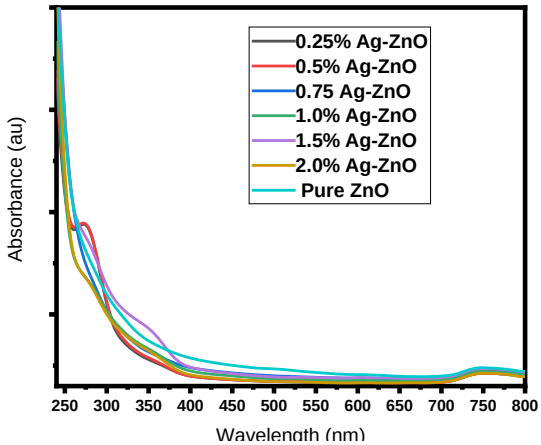


Figure 4.23: UV-vis spectra of pure and doped Ag-ZnONPs

The band gap energy was obtained by plotting a graph of $(\alpha hv)^2$ versus energy (eV) then extrapolated according to Tauc's equation (4.18)

$$(\alpha hv)^{\gamma}=A(hv-Eg) \quad (4.18)$$

Where Eg is the bandgap energy, A is a constant, h is the plank's constant, v is the photon frequency,α symbolize absorption coefficient and γ designate the electronic transition and can be 2 or ½ for direct and indirect allowed transitions respectively. It can also denote direct or indirect forbidden transition if its 2/3 and ⅓ respectively. If Taucs equation is compared to the equation of straight such that the Y in equation 4.19 is equal to zero then equation 4.20 is obtained

$$Y=m(x) \quad (4.19)$$

Putting the y axis equal to zero then

$$0=A(hv-Eg) \quad (4.20)$$

Thus **hv=Eg**

Figure 4.24 shows the bandgap energies of different concentrations of silver dopant in ZnONPs. The band gap energies decrease with an increase in silver concentration from 3.69, 3.61, 3.17, 3.10, 3.13, 3.03 and 3.30 eV for 0.25%, 0.5%, 0.75%, 1.0%, 1.5%, 2.0% and pure ZnO, respectively.

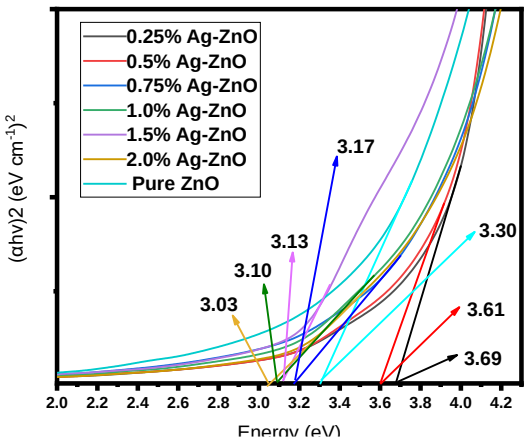


Figure 4.24: Tauc's plot showing estimated bandgap energies of pure and doped Ag-ZnONPs

Zinc oxide bandgap widen when doped with donors but decrease when doped with acceptors. The bandgap energy increases slightly when doped with lower percentage of Ag due to quantum effect. Increase in dopant concentration, weakens the

confinement effects by increasing the defect level, thus decreasing in bandgap (Amrute *et al*., 2024).

4.3.5 Morphology

Figure 4.25 shows the SEM images and particles size of 0.25, 1.5 and 2.0 % AgZnONPs. The nanoparticles obtained were displayed a notable changes when different concentration of silver dopant was used. At 0.25 %mol Ag-ZnO nanoparticles the distribution of nanoparticles were relatively uniform with minor distribution, this suggest that the growth and nucleation of nanoparticles were under controlled (Cartwright *et al* 2020). When the concentration of dopant was increased the rate of aggregation increased and the size of nanoparticles increase. At 2.0 % mol Ag-ZnONPs the nanoparticles were larger in size and more compacted as observed in Figure 4.25.

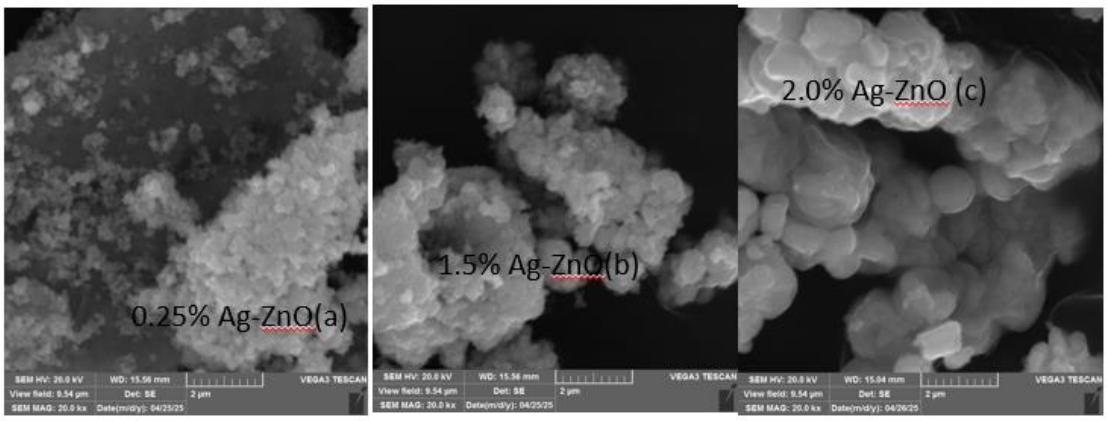


Figure 4.25: SEM images of (a) 0.25, (b) 1.5 and (c) 2.0% Ag-ZnONPs

The surface of nanoparticles also appeared to be smoother at higher concentration and this result from reduced repulsion forces in nanoparticles due excessive dopant ions or coalescence (Cartwright *et al* 2020). The nanoparticles average sizes were 27.42, 28.22 and 47.52 for 0.25, 1.5 and 2.0 % Ag-ZnONPs respectively. The data obtained showed that at higher concentration of silver dopant in ZnONPs it can hinders the homogenous particle formation and affects its surface area and active sites which are critical in application of ZnONPs.

The energy dispersive X-ray spectroscopy (EDS) was used to investigate the elemental composition of the synthesized Ag-ZnONPs. The EDS of all the samples prepared showed the presence of zinc (Zn), oxygen (O) and silver (Ag) only as shown in Figure 4.26. The absence of extra impurity peak in EDS spectra propose that the purity of

obtained nanoparticles with no sign of any additives left in the final obtained solid precipitate.

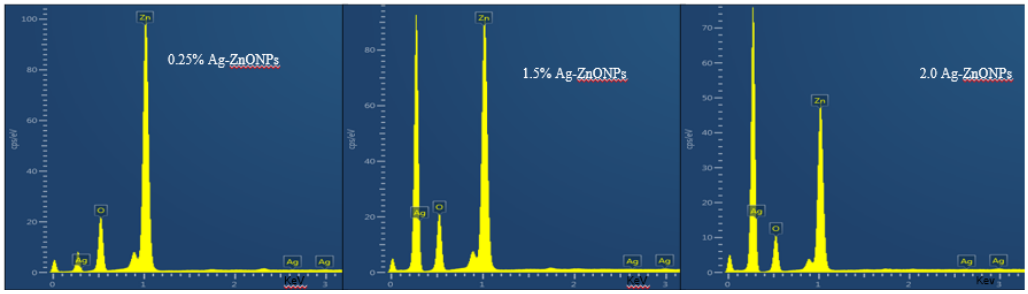


Figure 4.26: EDS spectra of 0.25, 1.5 and 2.0 Ag-ZnONPs

The atomic percentage of silver dopant increased as the concentration of dopant increased from 0.04 to 0.26 % for 0.25 and 2.0 % Ag-ZnONPs. Table 4.9, 4.10 and 4.11 summarizes the atomic percentage of elements present in 0.25, 1.5 and 2.0 % Ag-ZnO nanoparticles.

Table 4.9 Elemental analysis of 0.25 % Ag-ZnONPs

Element name	Element symbol	Element number	Weight %	Atomic %
Zinc	Zn	30	83.0	54.49
Oxygen	O	8	17.0	45.46
Silver	Ag	47	0.1	0.04

Table 4.10 Elemental analysis of 1.5 % Ag-ZnONPs

Element name	Element symbol	Element number	Weight %	Atomic %
Zinc	Zn	30	77.8	45.35
Oxygen	O	8	22.8	54.50
Silver	Ag	47	0.4	0.15

Table 4.11 Elemental analysis of 2.0 % Ag-ZnONPs

Element name	Element symbol	Element number	Weight %	Atomic %
Zinc	Zn	30	83.1	55.56
Oxygen	O	8	16.2	44.18
Silver	Ag	47	0.6	0.26

The distribution of this elements were observed using EDS layered image. Figure 4.27 shows the elemental distribution of 0.25, 1.5 and 2.0 % synthesized Ag-ZnONPs. An extensive signal of uniform distribution of Zinc and oxygen throughout the samples were observed confirming the formation of ZnO nanoparticles. Some region of the images had brighter colors such as in 2.0 % Ag-ZnONPs the bright red region indicates the possibility of zinc agglomeration. Silver dopant was uniformly distributed in all the images confirming that successful doping was achieved.

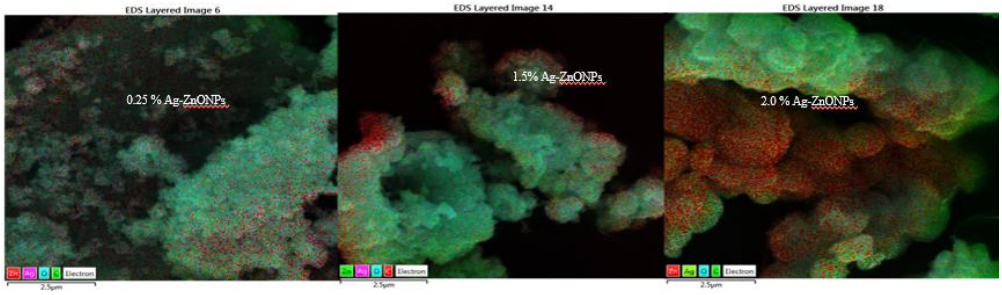


Figure 4.27: EDS layered images of 0.25, 1.5 and 2.0 % Ag-ZnONPs

4.4. Effects of growth temperature on *Citrus reticulata* capped Ag-ZnO nanoparticles

Growth temperature is one of the thermodynamic parameters that have an impact on the structural, optical, growth rate and size distribution of nanoparticles. The emission color and purity of nanoparticles are affected by crystal size and size distribution. When the growth temperature of nanoparticles is controlled, the size and size distribution of nanoparticles can be controlled to a certain extent. Good PL properties can be obtained when the surface structure of nanoparticles is controlled, and this will help in different applications of the nanoparticles (Kiprotich *et al*., 2018). The electrical, structural, physical, chemical and optical properties of nanoparticles depend on the size of the nanostructure due to quantum confinement effects (Lambora & Bhardwaj, 2023).

4.4.1 The XRD Analysis

The XRD pattern in Figure 4.28 shows that all the samples had hexagonal wurtzite structure of ZnO. The increase in temperature shift the peaks to higher 2 theta. As the temperature increases at 60, 65 and 70 ℃ a peak at 2θ:38.11, 38.17 and 38.30 ℃

respectively marked with (*) were observed which belongs to Ag, this indicates that there was clustering of silver at higher temperatures.

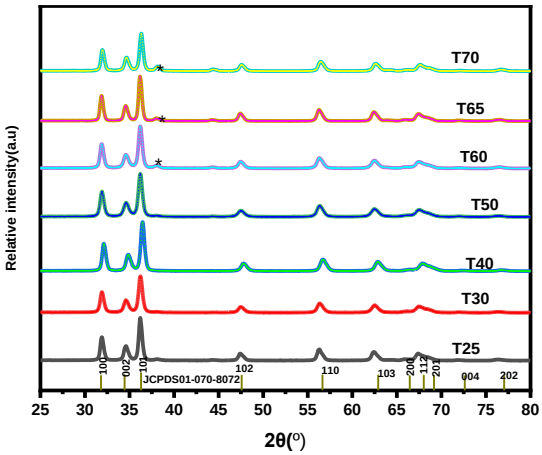


Figure 4.28: XRD pattern of Ag-ZnO prepared at different temperatures

The effects of growth temperature were examined by monitoring the peak position of Ag-ZnO diffraction. The vertical lines of JCPDS file no 01-070-8072 matches with all the XRD patterns of the samples. The XRD pattern of plane 101 was used to determine the effects of growth temperature on shift position and intensity.

In Figure 4.29 it was observed that at 40 ℃ the intensity of the peaks was very high compared to other peaks indicating that the samples prepared at this temperature had the best crystal structures.

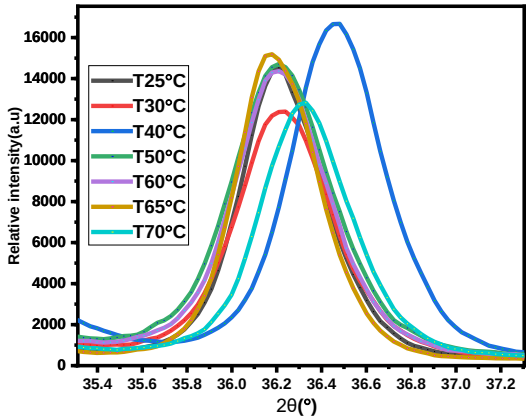


Figure 4.29: Enlarged image of diffraction plane [101] for capped Ag-ZnONPs prepared at different temperatures

The peak position was observed to shift towards the higher angle compared to other peaks. At a temperature of 25, 50, and 60 ℃ the intensity of the peaks were almost similar, nanoparticles prepared at 65 ℃ had slightly higher intensity. At 30 ℃ the intensity of the peak was the lowest, and the FWHM was also the smallest. The peaks shift towards the higher angle from 50, 60, 65, and 70 ℃. The plane [101] had the highest intensity and was used to calculate the d spacing and lattice parameters of Ag-ZnO.

Bragg's equation (4.21) was used to calculate the d-spacing, and Scherrer equation (4.20) was used to calculate the crystal size of nanoparticles synthesized at varying temperatures (Fatimah *et al*., 2022). Table 4.12 shows results obtained.

$$\boldsymbol{n\lambda = 2dsin\theta} \quad (4.21)$$

Where d is the spacing between atomic planes (the interplanar spacing), λ is the wavelength of the incident wave, n is the order of diffraction peak which was 1 and θ is the incidence angle. Equation 4.22 was used to calculate the crystal size of nanoparticles.

$$\boldsymbol{D = \frac{k\lambda}{\beta_{hkl}cos\theta}} \quad (4.22)$$

In the Debye Scherrer equation, D is the average crystal size (grain size), k is dimensionless shape factor typically 0.9, β is the full width at half maximum (FWHM), λ is the wavelength of Cu Ka (1.5406) and θ is the peak position. Table 4.12 summarized the calculated lattice parameters, crystal size and FWHM of Ag-ZnONPs synthesized at different growth temperature.

Table 4.12: Summarized calculated lattice parameters, crystal size and FWHM

Temperature	θ degrees			FWHM degrees			d-spacing	a	c	D	Strain ($\times 10^{-3}$)
	100	002	101	100	002	101					
25℃	15.92	17.28	18.08	0.4390	0.5384	0.4315	2.4781	3.2417	5.1865	17.87	6.678
30℃	15.96	17.32	18.11	0.4822	0.5688	0.4814	2.4774	3.2348	5.1748	16.37	7.2461
40℃	16.06	17.44	18.23	0.4794	0.6087	0.4909	2.4623	3.214	5.138	15.98	7.4077
50℃	15.96	17.32	18.10	0.5104	0.5954	0.5073	2.4787	3.2348	5.1748	15.54	7.6298
60℃	15.95	17.31	18.10	0.4700	0.5941	0.4682	2.4782	3.2368	5.1763	16.47	7.247
70℃	15.99	17.34	18.16	0.4500	0.5271	0.4532	2.4715	3.2289	5.1676	17.52	6.7488

The d spacing obtained from all the temperatures were close to that of standard 2.473520. The crystal size obtained decreased with an increase in temperature up to 50 ℃. At 60 ℃ the grain size started to increase in size this can be ascribed to the fact that at higher temperature the rate of nucleation is high and large crystals are stabilized. Liu *et a*l (2020) observed the same trend when Ag nanoparticles were synthesized at growth temperature above 80 ℃ where the grain sizes increased tremendously (Liu *et al*., 2020). It was concluded that growth temperature had significant influence on the grain size and interplanar spacing of nanoparticles.

Figure 4.30 shows the variation of crystal size with FWHM of nanoparticles prepared at different growth temperatures.

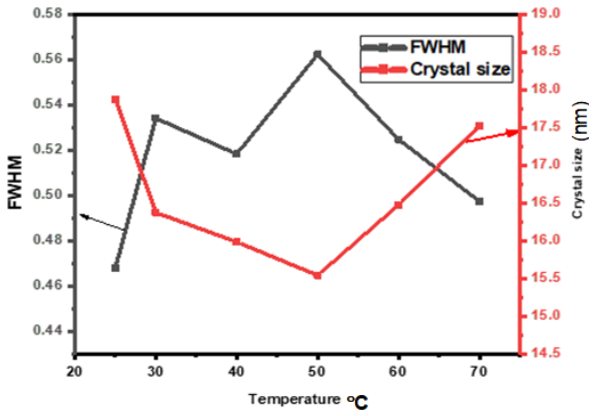


Figure 4.30: Variation of crystal size with FWHM at a temperatures

From the graph it can be noted that $D \propto \frac{1}{FWHM}$, the crystal size relatively decreases with an increase in temperature this might have result due to rearrangement of atoms at higher temperatures causing the nanoparticles to obtained irregular shape thus hindering the growth of the grain substitution took place instead of atoms occupying the interstitial site. After 50 ℃ the crystal size increase in size due to high temperature favoring rearrangement of atoms into a favorable position thus facilitating the growth in crystal size. Similar results was observed when ZnONPs were synthesized at growth temperature of 35 ℃ the crystal size obtained was 28 nm and it increased to 34.8 nm when growth temperature was increased to 75 ℃ (Shaba *et al., 2021)*

The lattice strain due to imperfection was calculated using equation 4.23.

$$\boldsymbol{\varepsilon = \frac{\beta_{hkl}}{4tan\theta}} \quad (4.23)$$

Where ε is the strain, β_{hkl} is the FWHM and θ is the peak position. Figure 4.31 shows the variation of crystal size with strain at different growth temperatures.

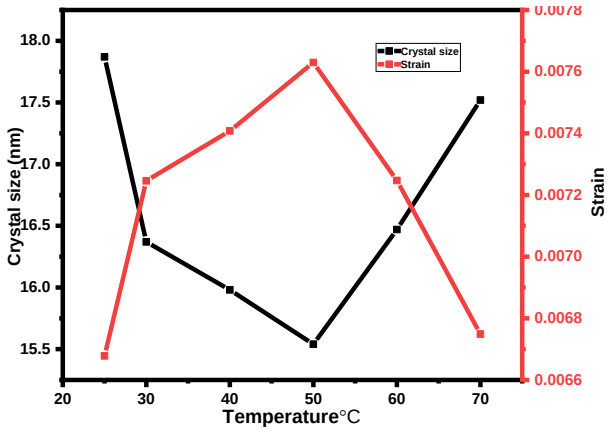


Figure 4.31: Plot of crystal size and strain of capped Ag-ZnO nanoparticles prepared at different temperature

The strain was inversely proportional to crystal size.$\varepsilon = \frac{1}{D}$. This can be associated with grain boundaries, as crystal size decreases the grain boundaries increases this results to misalignment of lattice parameters. Nanoparticles with smaller crystal size had high lattice strain and as the crystal size increase the lattice strain decreased. K. Li *et al*., 2018 observed similar results with ZnO nanorod having crystal size of 18 nm having high strain.

4.4.2 FT-IR analysis

Figure 4.32 shows the FT-IR spectra of Ag-ZnO prepared at different temperatures and recorded at the range of 400-4000 cm^{-1} at transmission mode.

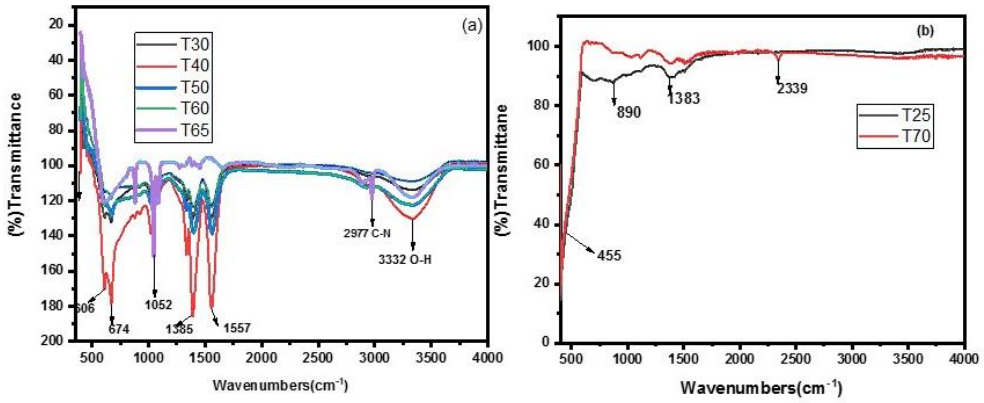


Figure 4.32: FT-IR spectra of Ag-ZnONPs at a growth temperature of (a) 30, 40, 50, 60, and 65 ℃ and (b) 25 and 70 ℃

From the data obtained, at 40 ℃ the bands were strong and intense, in Figure 4.32 the broad peak at 3332 cm^{-1} corresponds to stretching vibration of O-H. The 2977 cm^{-1} reveal the bending N-H which was very intense at 65 ℃. The sharp peaks at 1557 and 1385 cm^{-1} corresponds to stretching symmetric and asymmetric C=O of carboxylic acid group. Sharp peaks that were observed at 1052 and 878 cm^{-1} correspond to bending vibration of CO and CH. The sharp peaks observed between 410 and 520 cm^{-1} are due to stretching vibrational mode of Zn-O nanoparticles (H. Liu *et al.,* 2020). Increase in growth temperature lead to a decreased in peak intensity. At the growth temperature of 25 and 70 ℃ Figure 4.32(b) showed that in both graph there was no O-H group and the only peaks observed were at 2339, 1384, 890 and 455 cm^{-1} which

corresponds to asymmetric and symmetric C-H, C=O, C-O and metal-oxide (Zn-O) vibration.

4.4.3 Photoluminescence spectroscopy

The PL spectra of the samples prepared at varying growth temperature and measured at ambiant temperature at an excitation energy of 300 nm is shown in Figure 4.33 (a). The PL gives the insight of optical and photochemical properties of Ag-ZnO nanoparticles. From the results it was observed that the spectra exhibit a strong UV excitation at 320 nm.

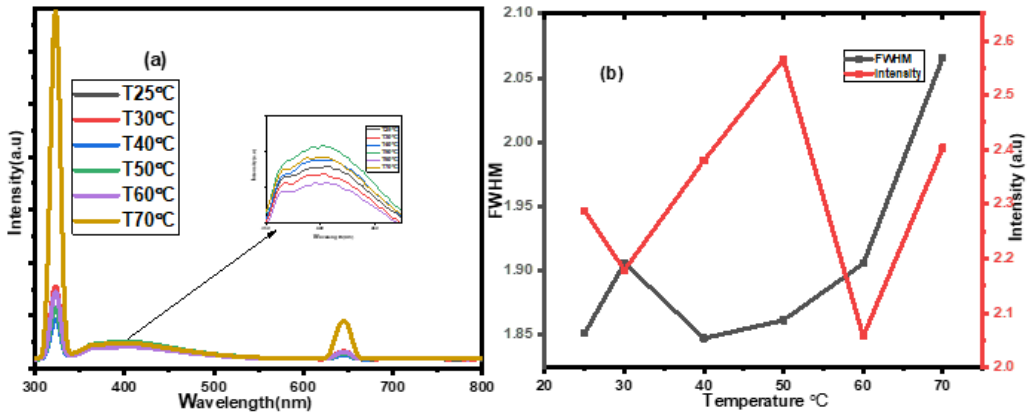


Figure 4.33: (a) PL spectra of Ag-ZnONPs (b) variation of PL FWHM and intensity at varying growth temperature

Emission was observed in the blue-green region in the near edge emission at 370, 367, 366, 370 and 360 nm for the 25, 30, 40, 50 and 60 ℃ respectively, when the samples were excited at 300 nm. There was no near band edge emission for the sample prepared at a growth temperature of 70 ℃. These emissions are associated with structural defects of material. These defects in ZnO nanoparticles can be neutral, singly or doubly charged Zn vacancies (Nadupalli *et al*., 2021). The peaks at 350-390 nm are assigned near band edge emission (NBE), this red emission is associated with singly defect which is a result of radiative recombination of electrons in the shallow donor level ($(Zni)^{\cdot\cdot}$) (C.-C. Wang *et al*., 2021), it is also associated with the Ostwald ripening process which happens when small particles dissolve as a results of higher surface energy to create larger particles (Kiprotich *et al*., 2016). It was clear that the intensity of the peaks increase with an increase in growth temperatures, given that at a growth temperature of 70 ℃, the strongest luminescence at 323 nm in the UV range was observed. At a growth temperature of 50 ℃ the highest emission was observed.

Higher growth temperatures improves the crystallinity of nanoparticles, this was verified by a decreased in defect level emission (DLE) with increase in growth temperature, suggesting there was a decreased in defects. Intrinsic and extrinsic defects are commonly associated with DLE. These defects include the anti-site oxygen (O_{Zn}), Zinc vacancies (V_{Zn}), oxygen vacancies (V_O), Zinc interstitial (Zn_i), interstitial oxygen (O_i) and substitution of oxygen at Zn position (O_{Zn}) (B. Wang *et al.,* 2024). Figure 4.33b shows the variation in full width at half maximum (FWHM) and the intensity of the emission peaks as the growth temperature varies. The FWHM was inversely proportional to intensity of the peaks and directly proportional to growth temperature $\propto \frac{\boldsymbol{TEMPERATURE}}{\boldsymbol{INTENSITY\ OF\ THE\ PEAK}}$.

4.4.4 Optical properties

To determine the effects of growth temperature on optical properties of Ag-ZnONPs, UV spectroscopy was used at standard temperature based on absorbance spectra. Figure 4.34 shows the absorbance spectra of Ag-ZnONPs synthesized at 25, 30, 40, 50, 60 and 70 ℃. The spectra displayed major absorption at 350-400 nm, with 50 ℃ growth temperature having the highest intensities. The intrinsic bandgap absorption of Ag-ZnONPs caused by electronic transition from valence band to conduction band induced absorption at 390-400 nm as shown in Figure 4.34.

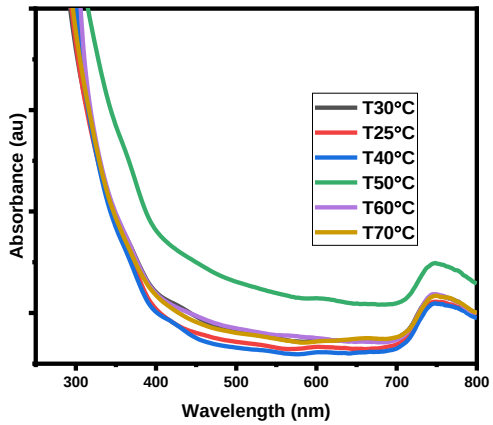


Figure 4.34: UV-vis spectra of Ag-ZnONPs prepared at different growth temperatures

Taucs equation 4.24 was used to determine the bandgap energies of nanoparticles prepared at different growth temperature.

$$(\alpha h\nu)^{\gamma} = A(h\nu - E_g) \quad (4.24)$$

Where α is the absorption coefficient, h is the plank's constants, v is the photon frequency, E_g is the band gap energy and the factor γ denotes the nature of the electronic transition. Electronic transitions are categorized into four sets, they can be direct allowed transition if γ is 2, indirect allowed transition γ is ½, direct forbidden transition γ is 2/3 and indirect forbidden transition ⅓. A graph of $(\alpha hv)^2$ versus the energy is plotted and extrapolated to obtain the bandgap energies of nanoparticles. The results obtained in Figure 4.35 showed that the optical bandgap energies decrease with increase in growth temperature, this behavior is associated with crystal quality and larger crystal size at high temperature (Roza *et al.*, 2015).

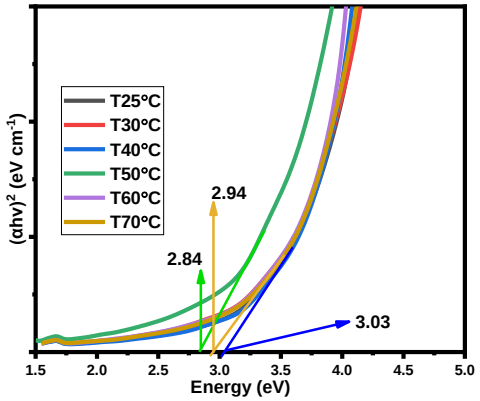


Figure 4.35: Tauc's plot $(\alpha hv)^2$ versus Energy (eV) of Ag-ZnONPs at different growth temperatures 25, 30, 40, 50, 60 and 70 °C

The bandgap energies decreased from 3.03 eV for growth temperature at 40 and 25 °C, 2.94eV for 70, 60 and 30 °C to 2.84 eV for 50 °C growth temperatures. Similar results were obtained by Abdulrahman *et al.* when ZnONPs were prepared by the chemical bath deposition method at varying growth temperature (Abdulrahman *et al.*, 2021).

4.4.5 Morphological analysis

To study the morphology of capped Ag-ZnONPs synthesized at different growth temperature, scanning electron microscope was used that is equipped with Energy dispersive X-ray spectroscopy. When different growth temperature was used to synthesized nanoparticles, the morphology and size of nanoparticles were affected as observed in Figure 4.36. At 30 °C the individual nanoparticle appeared to be round and some spherical in shape.

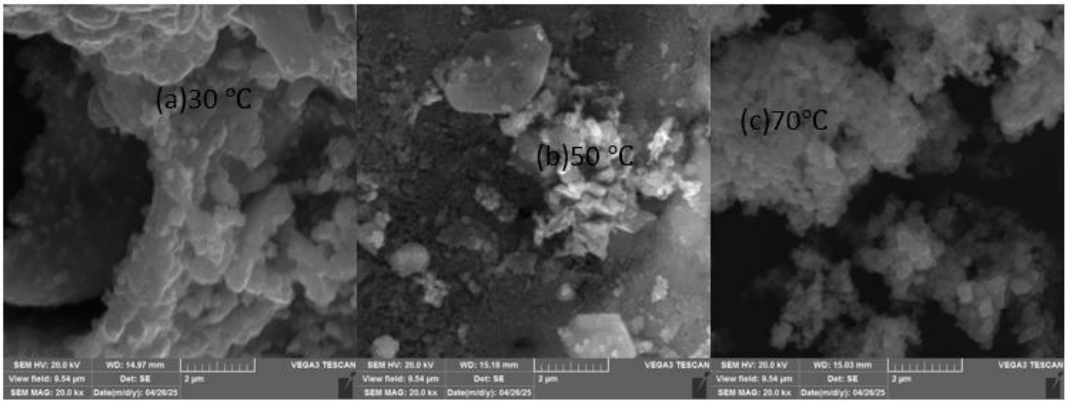


Figure 4.36 SEM images of Ag-ZnONPS synthesized at a growth temperature of (a) 30 (b) 50 and (c) 70 °C

The nanoparticles were unevenly distributed and others aggregate forming a cluster. The surface texture appears to be porous which could be as a results of presence of organic capping agents (Vishakha et al., 2023). The presence of phytochemicals such as polyphenols and flavonoid in *Citrus reticulata* which stabilize nanoparticles can also interlink nanoparticles (Sidhu *et al*., 2023). As the temperature increased as observed in Figure 4.36 (b) at 50°C the size of nanoparticles decreased and the rate of nucleation decreased. The size of nanoparticles were non-uniformly distributed as evidence by the presence of large flat faced grain at the top center which implies that nanoparticles obtained went through anisotropic growth (Zhao *et al.,* 2021). At a growth temperature of 70 °C the rate of aggregation increased and the nanoparticles obtained were spherical in shape and had no facet. Some of the nanoparticles appeared to be fused together and are densely packed with low porosity.

Growth temperature has significant impact on the morphology of nanoparticles and this affects the application of nanoparticles. Other factors that their morphology include the reaction time and annealing temperature used.

The elemental analysis of *Citrus reticulata* capped Ag-ZnONPs are shown in Figure 4.37. The EDS spectrum confirm the presence of Ag, Zn and O in the synthesized nanoparticles. The atomic percentage of the elements shows a slight shift based on their degree of strength, the presence of distinct silver peak confirm that doping occurred which is sufficient to influence structural, morphological, optical and

photoluminescence properties of ZnONPs. The absence of impurity peaks suggest that the nanoparticles obtained were pure.

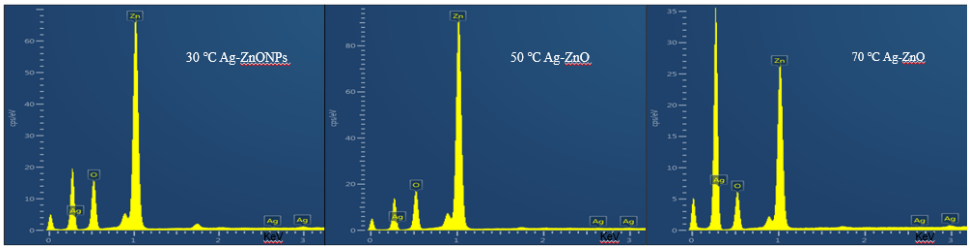


Figure 4.37: EDS spectra of synthesized Ag-ZnONPs at different growth temperature

Table 4.13, 4.14 and 4.15 summarized the elemental composition of Ag-ZnONPs synthesized at a growth temperature of 30, 50 and 70 ℃. The atomic percentage of Zn was high in all the samples followed by oxygen since the concentration of precursor material used was maintained throughout the synthesis process.

Table 4.13 Elemental analysis of Ag-ZnONPs synthesized at a growth temperature of 30 ℃.

Element name	Element symbol	Element number	Weight %	Atomic %
Zinc	Zn	30	83.6	56.14
Oxygen	O	8	15.9	43.42
Silver	Ag	47	0.6	0.44

Table 4.14 Elemental analysis of Ag-ZnONPs synthesized at a growth temperature of 50 ℃.

Element name	Element symbol	Element number	Weight %	Atomic %
Zinc	Zn	30	80.4	50.35
Oxygen	O	8	19.3	49.53
Silver	Ag	47	0.3	0.12

Table 4.15 Elemental analysis of Ag-ZnONPs synthesized at a growth temperature of 30 ℃.

Element name	Element symbol	Element number	Weight %	Atomic %
Zinc	Zn	30	85.7	60.0
Oxygen	O	8	13.4	38.92
Silver	Ag	47	0.9	0.37

The EDS layered images of Ag-ZnONPs synthesized at a growth temperature of 30, 50 and 70 ℃ is shown in Figure 4.38.

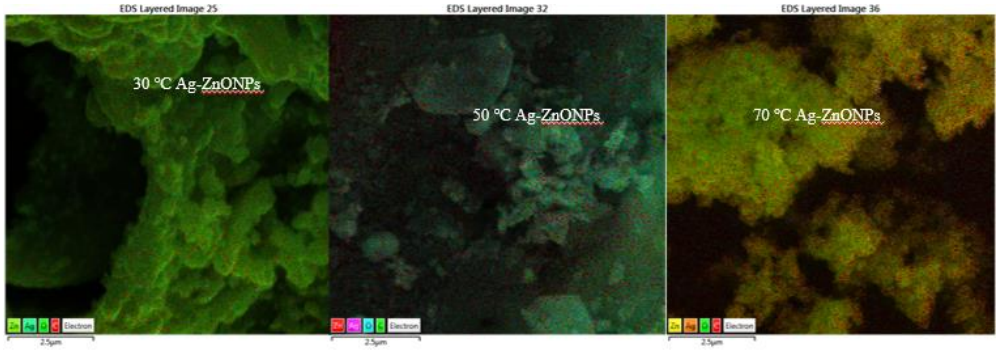


Figure 4.38 EDS images of Ag-ZnONPs synthesized at different growth temperatures

The image demonstrate the elemental distribution across the surface of synthesized nanoparticle. In all the images the zinc is uniformly distributed along with oxygen which confirms that ZnO was successfully synthesized. Silver dopant was sparsely distributed in all the samples suggesting effective incorporation of silver in trace amount without forming a separate aggregate. The presence of cyan or carbon coating (c) on the surface of the nanoparticles confirm the presence of organic material *Citrus reticulata* that was used as capping agents. The distribution pattern of the EDS layered images confirm both doping of ZnO with silver and the surface modification of organic species which influence material's optical, structural and morphological properties.

4.5 Summary

Citrus reticulate capped Ag-ZnO nanoparticles were successfully synthesized using green synthesis method, the FT-IR showed stretching vibration in both the functional group and fingerprint region. The fingerprint region showed metal oxide stretching vibration for doped and undoped nanoparticles. XRD confirmed the growth of nanoparticles and EDS showed the elements present in the nanoparticles. SEM analysis showed the morphology of nanoparticles that improved when dopant was

added and high growth temperature was used to synthesized nanoparticles. The PL emission showed the increase in emission peaks when higher concentration of dopant was used and lastly the UV-Vis results showed a relatively low bandgap energy at high growth temperature.

CHAPTER FIVE
CONCLUSION AND RECOMMENDATIONS

5.1 Conclusion

Nanoparticles of ZnO and Ag-ZnO were successfully synthesized using *Citrus reticulata* peel extract. The presence of capping agent, different mol % of silver dopant and growth temperatures enormously affects the properties of nanoparticles. XRD spectra verify that both capped and uncapped ZnONPs had hexagonal wurtzite structures. Crystal size calculated from Debye Scherrer equation showed that the use of capping agents to synthesize nanoparticles reduced the crystal size from 13.69 nm to 10.19 nm. The use of *Citrus reticulata* shift nanoparticles to a lower 2 theta as compared to uncapped nanoparticles. The FT-IR spectra confirms the presence of functional groups in both capped and uncapped ZnO nanoparticles. The peaks for ZnO were observed at 476 and 437 cm^{-1}, due to optical transverse mode of ZnO. The FT-IR spectrum for uncapped ZnONPs had significant spectral noise and the peaks were not as sharp compared to that of capped ZnO. Absorption spectra were obtained when samples were characterized using UV-vis spectroscopy. The samples were dissolve in deionized water and scan at a wavelength of 200 to 800 nm. Tauc's equation was plotted to obtain the bandgap energies of nanoparticles. The capped ZnONPs had a larger bandgap of 3.52 eV as compared to 3.4 eV of pure ZnONPs. Capping agents alters the structural and electrical properties of nanoparticles, and as a results it changes the energy level between the conduction and valence band. Other factors that might have contributed to increase in bandgap energy include the failure of ZnONPs to fully dissolve in the solvent. Only deionized water was used as a solvent to ensure that the chemical component of materials was no interfere and it had a absorption index of one. The PL spectra was used to study the electronic and defects in *Citrus reticulata* capped Ag-ZnONPs. The spectra of the samples were obtained at room temperature at an excitation energy of 300 nm. Pure ZnO nanoparticles had the highest emission when compared to capped ZnONPs. When ZnONPs were doped with silver, all the samples emit strongly in the UV region, with a band centered at 323 nm which correspond to excitonic emission when excited at 300 nm. Scanning electron microscope (SEM) equipped with energy dispersive X-ray spectroscopy (EDS or EDX) was used to study the morphological properties and elemental analysis of *Citrus reticulata* capped ZnONPs. The use of capping agents helped to reduce the agglomeration of nanoparticles and the particles obtained were in spherical like shape.

When ZnONPs were doped with varying concentration of silver, the hexagonal structure of ZnO was maintained. 0.1% Ag-ZnO displayed highest peak in XRD pattern at plane [101]. The crystal size of the nanoparticles ranged from 15.29-19.87nm. At 0.5% Ag-ZnONPs, the XRD peak shifted to higher 2 theta degrees compared to other doping concentrations. When the concentration of Ag was increased, the peak position shifted towards the lower 2 theta. The shift indicates partial substitution of Ag^{+} at the lattice sites of ZnO, which leads to an increase in lattice parameters a and c. When doped with 0.25, 0.5, 0.75, 1.0, 1.5, and 2.0 % Ag. The O-H was observed at 2978-3633 cm^{-1}. The peaks becomes less intense when the concentration of silver decrease, this can be associated with partial substitution of silver ions in the ZnO lattice structure thus causing changes in the bond length. The FT-IR spectra showed more prominent vibration mode with Ag-ZnO than for ZnO this clearly indicates that strong doping occurred. When ZnONPs were doped with silver, the bandgap energies decrease with an increase in silver concentration from 3.69, 3.61, 3.17, 3.10, 3.13, 3.03 and 3.30 eV for 0.25, 0.5, 0.75, 1.0, 1.5, 2.0 mol% and pure ZnO respectively. The bandgap energy increases slightly when doped with lower percentage of Ag due to quantum effect. Increase in dopant concentration, weaken the confinement effects by increasing the defects level thus decrease in bandgap. The nanoparticle doped with 1.0 mol% silver had the highest peak intensity and 2.0 mol%Ag-ZnO nanoparticles had the lowest intensity. The emission spectra at 350-400nm was also observed. The sample with the highest intensity in the emission spectra was 1.5 mol% Ag-ZnO nanoparticles and 0.25 mol% had the lowest intensity. When different concentration of dopant was added to capped ZnONPs the SEM images showed an increase in size of nanoparticles with increase in dopants and the rate of aggregation also increased. The surface of nanoparticles appeared to be smoother at higher concentrationsof 2.0% Ag-ZnONPs.

When nanoparticles were prepared at different growth temperature, the intensity of peaks at plane [101] showed that peaks shift towards the higher angle from 50, 60, 65, and 70 ℃. The crystal size obtained decreased with an increase in temperature up to 50 ℃, at 60 ℃ the grain size started to increase. As the temperature increases at 60, 65 and 70 ℃ a peak at 2θ:38.11, 38.17 and 38.30 ℃ respectively were observed which

belongs to Ag, this indicates that there was clustering of silver at higher temperatures. The crystal size and FWHM were inversely proportional to strain. The FT-IR spectra was used to determine the functional group present in the sample. As growth temperature was varied, broad and intense peaks were observed at 40 ℃. At a temperature of 25 and 70 ℃ there was no O-H vibration in the functional group region. When Tauc's equation was used to determine the bandgap energy, the bandgap energy decreased from 3.03 eV for growth temperature at 40 and 25 ℃, 2.94 eV for 70, 60 and 30 ℃ to 2.84 eV for 50 ℃ growth temperatures. Increase in growth temperature increases the intensity of the peaks, given that at a growth temperature of 70 ℃, the strongest luminescence at 323 nm in the UV range was observed. At a growth temperature of 50 ℃ the highest emission was observed. Higher growth temperatures improves the crystallinity of nanoparticles, this was verified by a decreased defect level emission (DLE) with increase in growth temperature, suggesting there was a decrease in defects.At different growth temperature of nanoparticles, the size of nanoparticles change and the rate of agglomeration also changed. At 50 ℃ the SEM image of nanoparticle showed a facet. The nanoparticles appeared to be round and other spherical. EDX spectra confirmed the atomic percentage of elements present in SEM images and in all the samples only silver, zinc and oxygen were present.

5.2. Recommendations

5.2.1 Recommendation for Policy

From the results obtained on the synthesis and characterization of silver doped zinc oxide nanoparticles using *Citrus reticulata* peel extract the following are recommended:

- *Citrus reticulata* capped Ag-ZnO to be tested in photoanode of solar cells.
- Other parts of *Citrus reticulata* be tested to determine their effects as capping agents
- The effects of other metals and non metal dopants on ZnO be assessed.

5.2.2 Recommendation for Future

Other transitional metal oxides such as titanium oxide can be doped with transitional metals and analyzed for potential application as photoanode.

This research recommend further research on doping ZnO with other dopants and co-doping with both transitional and p type elements for photoanode applications.

Different plant extracts can be used to synthesize nanoparticles and they are safe and readily available, further research is recommended to analyze the impacts of phytochemicals on properties of nanoparticles.

REFERENCES

Abass, N. K., Shanan, Z. J., Mohammed, T. H., & Abbas, L. K. (2018). Fabricated of Cu doped ZnO nanoparticles for solar cell application. *Baghdad Science Journal*, *15*(2), 0198–0198.

Abdulrahman, A. F., Ahmed, S. M., Hamad, S. M., & Barzinjy, A. A. (2021). Effect of Growth Temperature on Morphological, Structural, and Optical Properties of ZnO Nanorods Using Modified Chemical Bath Deposition Method. *Journal of Electronic Materials*, *50*(3), 1482–1495.

Abdulrahman, N. A., & Haddad, N. I. (2020). Braggs, Scherre, Williamson–Hall and SSP analyses to estimate the variation of crystallites sizes and lattice constants for ZnO nanoparticles synthesized at different temperatures. *NeuroQuantology*, *18*(1), 53.

Aguilar Jáuregui, M. E., Peredo Macías, C., Orantes Jiménez, S. D., Flores de los Rios, P. A., & San Martín Martínez, E. (2022). Luminescence Properties of Nanomaterials. *Computación y Sistemas*, *26*(3), 1137–1142.

Ahmad, I., Ahmed, E., Ullah, M., Rana, A. M., Manzoor, M. F., Rasheed, M. A., Malik, A. S., Khalid, N. R., Ahmad, M., & Mehtab, U. (2018). SYNTHESIS AND CHARACTERIZATION OF SILVER DOPED ZnO NANOPARTICLES FOR HYDROGEN PRODUCTION. *Journal of Ovonic Research*, *14*(6).

Ahmed, S., Kaur, G., Sharma, P., Singh, S., & Ikram, S. (2018). Fruit waste (peel) as bio-reductant to synthesize silver nanoparticles with antimicrobial, antioxidant and cytotoxic activities. *Journal of Applied Biomedicine*, *16*(3), 221–231.

Akbari, B., Tavandashti, M. P., & Zandrahimi, M. (2011). Particle size characterization of nanoparticles–a practical approach. *Iranian Journal of Materials Science and Engineering*, *8*(2), 48–56.

Akhtar, K., Khan, S. A., Khan, S. B., & Asiri, A. M. (2018). Scanning Electron Microscopy: Principle and Applications in Nanomaterials Characterization. In S. K. Sharma (Ed.), *Handbook of Materials Characterization* (pp. 113–145). Springer International Publishing.

Al-Ansari, R. A. (2016). Structural, Morphological and Optical Properties of CDO: Al Thin Films Prepared by Chemical Spray Pyrolysis Methode. *Journal of Applied Physics (IOSR-JAP)*, *8*, 06–15.

Al-Ezzi, A. S., & Ansari, M. N. M. (2022). Photovoltaic solar cells: A review. *Applied System Innovation*, *5*(4), 67.

Ali, I. O., Nady, H., Mohamed, M. I., & Salama, T. M. (2024). Fabrication and characterization of ZnO and Ag/ZnO nanoparticles for efficient degradation of crystal violet dye in aqueous solution. *Journal of the Indian Chemical Society*, *101*(12), 101480.

Aly, K. A., Khalil, N. M., Algamal, Y., & Saleem, Q. M. (2016). Lattice strain estimation for CoAl2O4 nano particles using Williamson-Hall analysis. *Journal of Alloys and Compounds*, *676*, 606–612.

Amit, Y., Li, Y., Frenkel, A. I., & Banin, U. (2015). From Impurity Doping to Metallic Growth in Diffusion Doping: Properties and Structure of Silver-Doped InAs Nanocrystals. *ACS Nano*, *9*(11), 10790–10800.

Amrute, V., Supin, K. K., Vasundhara, M., & Chanda, A. (2024). C. *RSC Advances*, *14*(45), 32786–32801.

Anbuvannan, M., Ramesh, M., Viruthagiri, G., Shanmugam, N., & Kannadasan, N. (2015). Synthesis, characterization and photocatalytic activity of ZnO nanoparticles prepared by biological method. *Spectrochimica Acta Part A: Molecular and Biomolecular Spectroscopy*, *143*, 304–308.

Apraj, V. D., & Pandita, N. S. (2016). Evaluation of skin anti-aging potential of Citrus reticulata blanco peel. *Pharmacognosy Research*, *8*(3), 160.

Arefeen, S., & Dallas, T. (2021). Low-cost racking for solar photovoltaic systems with renewable tensegrity structures. *Solar Energy*, *224*, 798–807.

Arya, S., Mahajan, P., Mahajan, S., Khosla, A., Datt, R., Gupta, V., Young, S.-J., & Oruganti, S. K. (2021). Influence of processing parameters to control morphology and optical properties of Sol-Gel synthesized ZnO nanoparticles. *ECS Journal of Solid State Science and Technology*, *10*(2), 023002.

Augusto, A., Herasimenka, S. Y., King, R. R., Bowden, S. G., & Honsberg, C. (2017). Analysis of the recombination mechanisms of a silicon solar cell with low bandgap-voltage offset. *Journal of Applied Physics*, *121*(20).

Bagher, A. M., Vahid, M. M. A., & Mohsen, M. (2015). Types of solar cells and application. *American Journal of Optics and Photonics*, *3*(5), 94–113.

Bandopadhyay, K., & Mitra, J. (2015). Zn interstitials and O vacancies responsible for n-type ZnO: What do the emission spectra reveal? *Rsc Advances*, *5*(30), 23540–23547.

Berehe, B. A., Assen, A. H., Kumar, A. S. K., Ulla, H., Duma, A. D., Chang, J.-Y., Gedda, G., & Girma, W. M. (2023). Highly efficient visible light active ZnO/Cu-DPA composite photocatalysts for the treatment of wastewater contaminated with organic dye. *Scientific Reports*, *13*(1), 16454.

Bett, K., & Kiprotich, S. (2024). *Effects of Stirring Speed of Precursor Solution on the Structural Optical and Morphological Properties of ZnO Al Ga CoDoped Nanoparticles Synthesized via a Facile Sol Gel Technique*.

Bindhu, M. R., Umadevi, M., Esmail, G. A., Al-Dhabi, N. A., & Arasu, M. V. (2020). Green synthesis and characterization of silver nanoparticles from Moringa oleifera flower and assessment of antimicrobial and sensing properties. *Journal of Photochemistry and Photobiology B: Biology*, *205*, 111836.

Bindu, P., & Thomas, S. (2014). Estimation of lattice strain in ZnO nanoparticles: X-ray peak profile analysis. *Journal of Theoretical and Applied Physics*, *8*(4), 123–134.

Blanco Andujar, C. (2014). *Sodium carbonate mediated synthesis of iron oxide nanoparticles to improve magnetic hyperthermia efficiency and induce apoptosis* [PhD Thesis, UCL (University College London)].

Bokov, D., Turki Jalil, A., Chupradit, S., Suksatan, W., Javed Ansari, M., Shewael, I. H., Valiev, G. H., & Kianfar, E. (2021). Nanomaterial by sol-gel method: Synthesis and application. *Advances in Materials Science and Engineering*, *2021*, 1–21.

Campbell, B., Kelly, P., Talamantes, A., & Kuznetsova, L. (2020). The interplay between bandgap renormalization and Burstein-Moss effect for multilayered Al: ZnO/ZnO metamaterial. *Metamaterials, Metadevices, and Metasystems 2020*, *11460*, 114600H.

Campisi, S., Schiavoni, M., Chan-Thaw, C. E., & Villa, A. (2016). Untangling the role of the capping agent in nanocatalysis: Recent advances and perspectives. *Catalysts*, *6*(12), 185.

Carvalho, P. M., Felício, M. R., Santos, N. C., Gonçalves, S., & Domingues, M. M. (2018). Application of light scattering techniques to nanoparticle characterization and development. *Frontiers in Chemistry*, *6*, 237.

Castro Alarcon, N., Herrera Arizmendi, J. L., Luis Alberto, M. C., Guzman Guzman, I. P., Perez Centeno, A., & Santana Aranda, M. A. (2016). *Antibacterial activity of nanoparticles of titanium dioxide, intrinsic and doped with indium and iron*.

Chavali, M. S., & Nikolova, M. P. (2019). Metal oxide nanoparticles and their applications in nanotechnology. *SN Applied Sciences*, *1*(6), 607.

Chen, S., Drehmel, J. R., & Penn, R. L. (2020). Facile Synthesis of Monodispersed Ag NPs in Ethylene Glycol Using Mixed Capping Agents. *ACS Omega*, *5*(11), 6069–6073.

Chen, Y., Du, C., Sun, L., Fu, T., Zhang, R., Rong, W., Cao, S., Li, X., Shen, H., & Shi, D. (2021). Improved optical properties of perovskite solar cells by introducing Ag nanopartices and ITO AR layers. *Scientific Reports*, *11*(1), 14550.

Chiang, T.-H., & Wager, J. F. (2017). Electronic conduction mechanisms in insulators. *IEEE Transactions on Electron Devices*, *65*(1), 223–230.

Chitradevi, T., Jestin Lenus, A., & Victor Jaya, N. (2020). Structure, morphology and luminescence properties of sol-gel method synthesized pure and Ag-doped ZnO nanoparticles. *Materials Research Express*, *7*(1), 015011.

Cojocaru, B., Avram, D., Kessler, V., Parvulescu, V., Seisenbaeva, G., & Tiseanu, C. (2017). Nanoscale insights into doping behavior, particle size and surface effects in trivalent metal doped SnO2. *Scientific Reports*, *7*(1), 9598.

Crouzier, L., Delvallée, A., Allard, A., Devoille, L., Ducourtieux, S., & Feltin, N. (2019). Methodology to evaluate the uncertainty associated with nanoparticle dimensional measurements by SEM. *Measurement Science and Technology*, *30*(8), 085004.

Crouzier, L., Delvallee, A., Ducourtieux, S., Devoille, L., Tromas, C., & Feltin, N. (2019). A new method for measuring nanoparticle diameter from a set of SEM images using a remarkable point. *Ultramicroscopy*, *207*, 112847.

Dandge, P. B., Garadkar, K. M., Dandge, P. B., & Kirdat, P. N. (2021). Suyog S. Synthesis of Zero Valent Silver Nanoparticles by Chemical Reduction Method and its Application: A Review. *International Journal of Nanomaterials and Nanostructures*, *7*(2), 8–17p.

Danks, A. E., Hall, S. R., & Schnepp, Z. (2016). The evolution of ‘sol–gel’chemistry as a technique for materials synthesis. *Materials Horizons*, *3*(2), 91–112.

De Melo, O. (2023). Introduction in II-VI Semiconductors. In G. Korotcenkov (Ed.), *Handbook of II-VI Semiconductor-Based Sensors and Radiation Detectors* (pp. 3–19). Springer International Publishing.

Desa, U. N. (2014). World urbanization prospects, the 2011 revision. *Population Division, Department of Economic and Social Affairs, United Nations Secretariat*.

Dhand, C., Dwivedi, N., Loh, X. J., Ying, A. N. J., Verma, N. K., Beuerman, R. W., Lakshminarayanan, R., & Ramakrishna, S. (2015). Methods and strategies for the synthesis of diverse nanoparticles and their applications: A comprehensive overview. *Rsc Advances*, *5*(127), 105003–105037.

Dorraj, M. (2018). *Enhanced Photocatalytic Activity of Copper-Doped Titanium Oxide Using Zinc Oxide Heterojunction and Iodide Co-Doping for Water Treatment Application* [PhD Thesis, University of Malaya (Malaysia)].

Dziubaniuk, M., Piech, R., & Paczosa-Bator, B. (2024). Electrochemical Impedance Spectroscopy Study of Ceria-and Zirconia-Based Solid Electrolytes for Application Purposes in Fuel Cells and Gas Sensors. *Materials*, *17*(21), 5224.

Ebhota, W. S., & Jen, T.-C. (2020). Fossil Fuels Environmental Challenges and the Role of Solar Photovoltaic Technology Advances in Fast Tracking Hybrid Renewable Energy System. *International Journal of Precision Engineering and Manufacturing-Green Technology*, *7*(1), 97–117.

Ehrampoush, M. H., Miria, M., Salmani, M. H., & Mahvi, A. H. (2016). *Cadmium removal from aqueous solution by green synthesis iron oxide nanoparticles with tangerine peel extract.*

Elumalai, K., & Velmurugan, S. (2015). Green synthesis, characterization and antimicrobial activities of zinc oxide nanoparticles from the leaf extract of Azadirachta indica (L.). *Applied Surface Science*, *345*, 329–336.

Endres, J., Egger, D. A., Kulbak, M., Kerner, R. A., Zhao, L., Silver, S. H., Hodes, G., Rand, B. P., Cahen, D., Kronik, L., & Kahn, A. (2016). Valence and Conduction Band Densities of States of Metal Halide Perovskites: A Combined Experimental–Theoretical Study. *The Journal of Physical Chemistry Letters*, *7*(14), 2722–2729.

Epp, J. (2016). X-ray diffraction (XRD) techniques for materials characterization. In *Materials characterization using nondestructive evaluation (NDE) methods* (pp. 81–124). Elsevier.

Fatimah, S., Ragadhita, R., Al Husaeni, D. F., & Nandiyanto, A. B. D. (2022). How to calculate crystallite size from x-ray diffraction (XRD) using Scherrer method. *ASEAN Journal of Science and Engineering*, *2*(1), 65–76.

Flores-Carrasco, G., Rodríguez-Peña, M., Urbieta, A., Fernández, P., & Rabanal, M. E. (2021). ZnO nanoparticles with controllable Ce content for efficient photocatalytic degradation of MB synthesized by the polyol method. *Catalysts*, *11*(1), 71.

Goel, S., & Kumar, B. (2020). A review on piezo-/ferro-electric properties of morphologically diverse ZnO nanostructures. *Journal of Alloys and Compounds*, *816*, 152491.

Green synthesis of silver doped zinc oxide nanoparticles... - Google Scholar. (n.d.). Retrieved 25 March 2024,

Gulati, S., Sachdeva, M., & Bhasin, K. K. (2018). Capping agents in nanoparticle synthesis: Surfactant and solvent system. *AIP Conference Proceedings*, *1953*(1).

Hasan, S. (2015). A review on nanoparticles: Their synthesis and types. *Res. J. Recent Sci*, *2277*, 2502.

Hassan, D., & El-mallul, A. (n.d.). *Characterization Techniques for Nanoparticles*. Retrieved 16 February 2025,

Hepburn, C., Qi, Y., Stern, N., Ward, B., Xie, C., & Zenghelis, D. (2021). Towards carbon neutrality and China's 14th Five-Year Plan: Clean energy transition, sustainable urban development, and investment priorities. *Environmental Science and Ecotechnology*, *8*, 100130.

Hossain, N., Mobarak, M. H., Mimona, M. A., Islam, M. A., Hossain, A., Zohura, F. T., & Chowdhury, M. A. (2023). Advances and significances of nanoparticles in semiconductor applications–A review. *Results in Engineering*, *19*, 101347.

Hosseini, S. M., Sarsari, I. A., Kameli, P., & Salamati, Hjj. (2015). Effect of Ag doping on structural, optical, and photocatalytic properties of ZnO nanoparticles. *Journal of Alloys and Compounds*, *640*, 408–415.

Hui, A., Ma, J., Liu, J., Bao, Y., & Zhang, J. (2017). Morphological evolution of Fe doped sea urchin-shaped ZnO nanoparticles with enhanced photocatalytic activity. *Journal of Alloys and Compounds*, *696*, 639–647.

Ibrahim, A. K., Abdelhameed, R. F., Habib, E. S., Ibrahim, A. K., & Badr, J. M. (2024). Chemistry of mandarin citrus reticulata. *Records of Pharmaceutical and Biomedical Sciences*, *8*(2), 134–147.

Ibrahim Khan, K. S., & Khan, I. (2019). Nanoparticles: Properties, applications and toxicities. *Arabian Journal of Chemistry*, *12*(7), 908–931.

Ibrahim, N. I., & Baher Edin Omer, M. M. (2020). The effect of wavelength of light on solar electrical performance. *ASME Power Conference*, *83747*, V001T08A003.

Iqbal, M., Ali, A., Ahmad, K. S., Rana, F. M., Khan, J., Khan, K., & Thebo, K. H. (2019). Synthesis and characterization of transition metals doped CuO nanostructure and their application in hybrid bulk heterojunction solar cells. *SN Applied Sciences*, *1*(6), 647.

Javed, R., Usman, M., Tabassum, S., & Zia, M. (2016). Effect of capping agents: Structural, optical and biological properties of ZnO nanoparticles. *Applied Surface Science*, *386*, 319–326.

Javed, R., Zia, M., Naz, S., Aisida, S. O., Ain, N. U., & Ao, Q. (2020). Role of capping agents in the application of nanoparticles in biomedicine and environmental remediation: Recent trends and future prospects. *Journal of Nanobiotechnology*, *18*(1), 172.

Jin, S.-E., & Jin, H.-E. (2019). Synthesis, characterization, and three-dimensional structure generation of zinc oxide-based nanomedicine for biomedical applications. *Pharmaceutics*, *11*(11), 575.

Jo, D. H., Kim, J. H., Lee, T. G., & Kim, J. H. (2015). Size, surface charge, and shape determine therapeutic effects of nanoparticles on brain and retinal diseases. *Nanomedicine: Nanotechnology, Biology and Medicine*, *11*(7), 1603–1611.

Jobe, M. C., Mthiyane, D. M., Mwanza, M., & Onwudiwe, D. C. (2022). Biosynthesis of zinc oxide and silver/zinc oxide nanoparticles from Urginea epigea for antibacterial and antioxidant applications. *Heliyon*, *8*(12).

Kaneko, R., Chowdhury, T. H., Wu, G., Kayesh, M. E., Kazaoui, S., Sugawa, K., Lee, J.-J., Noda, T., Islam, A., & Otsuki, J. (2019). Cobalt-doped nickel oxide nanoparticles as efficient hole transport materials for low-temperature processed perovskite solar cells. *Solar Energy*, *181*, 243–250.

Kaningini, A. G., Azizi, S., Sintwa, N., Mokalane, K., Mohale, K. C., Mudau, F. N., & Maaza, M. (2022). Effect of Optimized Precursor Concentration,

Temperature, and Doping on Optical Properties of ZnO Nanoparticles Synthesized via a Green Route Using Bush Tea (*Athrixia phylicoides* DC.) Leaf Extracts. *ACS Omega*, *7*(36), 31658–31666.

Kareem, M. A., Bello, I. T., Shittu, H. A., Sivaprakash, P., Adedokun, O., & Arumugam, S. (2022). Synthesis, characterization, and photocatalytic application of silver doped zinc oxide nanoparticles. *Cleaner Materials*, *3*, 100041.

Karthiga, P. (2018). Preparation of silver nanoparticles by Garcinia mangostana stem extract and investigation of the antimicrobial properties. *Biotechnology Research and Innovation*, *2*(1), 30–36.

Kavitha, S., Dhamodaran, M., Prasad, R., & Ganesan, M. (2017). Synthesis and characterisation of zinc oxide nanoparticles using terpenoid fractions of Andrographis paniculata leaves. *International Nano Letters*, *7*(2), 141–147.

Kayani, Z. N., Usman, A., Nazli, H., Sagheer, R., Riaz, S., & Naseem, S. (2020). Dielectric and magnetic properties of dilute magnetic semiconductors Ag-doped ZnO thin films. *Applied Physics A*, *126*(7), 559.

Khosravi-Gandomani, S., Yousefi, R., Jamali-Sheini, F., & Huang, N. M. (2014). Optical and electrical properties of p-type Ag-doped ZnO nanostructures. *Ceramics International*, *40*(6), 7957–7963.

Kim, M., Yim, K., Leem, J., Kim, S., Nam, G., Lee, D., Kim, J., & Kim, J. (2011). Effects of annealing temperature on the structural and the optical properties of ZnO thin films grown on porous silicon by using plasma-assisted molecular beam epitaxy. *Journal of the Korean Physical Society*, *59*.

Kiprotich, S., Dejene, F. B., Ungula, J., & Onani, M. O. (2016). The influence of reaction times on structural, optical and luminescence properties of cadmium telluride nanoparticles prepared by wet-chemical process. *Physica B: Condensed Matter*, *480*, 125–130.

Kiprotich, S., Onani, M. O., & Dejene, F. B. (2018). Effect of growth temperature on the structural, optical and luminescence properties of cadmium telluride nanoparticles. *Journal of Materials Science: Materials in Electronics*, *29*(7), 6004–6011.

Ko, Y.-D., Kim, K.-C., & Kim, Y.-S. (2012). Effects of substrate temperature on the Ga-doped ZnO films as an anode material of organic light emitting diodes. *Superlattices and Microstructures*, *51*(6), 933–941.

Kozák, O., Sudolská, M., Pramanik, G., Cígler, P., Otyepka, M., & Zbořil, R. (2016). Photoluminescent Carbon Nanostructures. *Chemistry of Materials*, *28*(12), 4085–4128.

Lambora, S., & Bhardwaj, A. (2023). Morphology Transition with Temperature and its Effect on Optical Properties of Colloidal MoS_2 Nanostructures. *ACS Omega*, *8*(30), 27725–27731.

Lee, K. M., Lai, C. W., Ngai, K. S., & Juan, J. C. (2016). Recent developments of zinc oxide based photocatalyst in water treatment technology: A review. *Water Research*, *88*, 428–448.

Lefatshe, K., Muiva, C., & Madhuku, M. (2021). Effect of low energy Ag+ ION implantation ON ZnO nanorods for enhanced visible light absorption-structural and optical analysis. *Optical Materials*, *122*, 111757.

Leilaeioun, M. A. (2018). *Fill factor loss mechanisms: Analysis and basic understanding in silicon hetero-junction solar cells* [PhD Thesis, Arizona State University].

Li, K., Wei, Z., Zhu, X., Zhao, W., Zhang, X., & Jiang, J. (2018). Microstructure and optical properties of ZnO nanorods prepared by anodic arc plasma method. *Journal of Applied Biomaterials & Functional Materials*, *16*(1_suppl), 105–111.

Li, S., Guo, N., Zhu, D., Jiang, D., Chen, Z., Chen, S., Sun, Z., & Wang, J. (2024). Enhanced CO_2 capture and stability of MgO modified with alkali metal nitrates and carbonates at moderate temperature. *Journal of Chemical Technology & Biotechnology*, *99*(11), 2289–2299.

Lin, H., Yang, M., Ru, X., Wang, G., Yin, S., Peng, F., Hong, C., Qu, M., Lu, J., & Fang, L. (2023). Silicon heterojunction solar cells with up to 26.81% efficiency achieved by electrically optimized nanocrystalline-silicon hole contact layers. *Nature Energy*, *8*(8), 789–799.

Liu, D., Li, C., Zhou, F., Zhang, T., Zhang, H., Li, X., Duan, G., Cai, W., & Li, Y. (2015). Rapid synthesis of monodisperse Au nanospheres through a laser irradiation-induced shape conversion, self-assembly and their electromagnetic coupling SERS enhancement. *Scientific Reports*, *5*(1), 7686.

Liu, H., Zhang, H., Wang, J., & Wei, J. (2020). Effect of temperature on the size of biosynthesized silver nanoparticle: Deep insight into microscopic kinetics analysis. *Arabian Journal of Chemistry*, *13*(1), 1011–1019.

Magdi, S., El-Rifai, J., & Swillam, M. A. (2018). One step fabrication of Silicon nanocones with wide-angle enhanced light absorption. *Scientific Reports*, *8*(1), 4001.

Mahlambi, M. M., Ngila, C. J., & Mamba, B. B. (2015). Recent Developments in Environmental Photocatalytic Degradation of Organic Pollutants: The Case of Titanium Dioxide Nanoparticles—A Review. *Journal of Nanomaterials*, *2015*(1), 790173.

Makuła, P., Pacia, M., & Macyk, W. (2018). How To Correctly Determine the Band Gap Energy of Modified Semiconductor Photocatalysts Based on UV–Vis Spectra. *The Journal of Physical Chemistry Letters*, *9*(23), 6814–6817.

Marschall, R., & Wang, L. (2014). Non-metal doping of transition metal oxides for visible-light photocatalysis. *Catalysis Today*, *225*, 111–135.

Masoumi, S., Nadimi, E., & Hossein-Babaei, F. (2018). Electronic properties of Ag-doped ZnO: DFT hybrid functional study. *Physical Chemistry Chemical Physics*, *20*(21), 14688–14693.

Mohar, R. S., Iwan, S., Djuhana, D., Imawan, C., Harmoko, A., & Fauzia, V. (2016). Post-annealing effect on optical absorbance of hydrothermally grown zinc oxide nanorods. *AIP Conference Proceedings*, *1729*(1).

Mugambi, N., Ngaruiya, J. M., & Mugo, S. W. (2023). Enhanced Electron Transport in Epitaxial Annealed Graphene Titanium Dioxide Heterojunction. *Path of Science*, *9*(5), 2001–2012.

Murashkina, A. A., Murzin, P. D., Rudakova, A. V., Ryabchuk, V. K., Emeline, A. V., & Bahnemann, D. W. (2015). Influence of the Dopant Concentration on the Photocatalytic Activity: Al-Doped TiO_2. *The Journal of Physical Chemistry C*, *119*(44), 24695–24703.

Murtaza, G., Ahmad, R., Rashid, M. S., Hassan, M., Hussnain, A., Khan, M. A., ul Haq, M. E., Shafique, M. A., & Riaz, S. (2014). Structural and magnetic studies on Zr doped ZnO diluted magnetic semiconductor. *Current Applied Physics*, *14*(2), 176–181.

Mustapha, S., Ndamitso, M. M., Abdulkareem, A. S., Tijani, J. O., Shuaib, D. T., Mohammed, A. K., & Sumaila, A. (2019). Comparative study of crystallite size using Williamson-Hall and Debye-Scherrer plots for ZnO nanoparticles. *Advances in Natural Sciences: Nanoscience and Nanotechnology*, *10*(4), 045013.

Mwankemwa, B. S., Malevu, T. D., Sahini, M. G., & Vuai, S. A. (2022). Effects of vertically aligned ZnO nanorods surface morphology on the ambient-atmosphere fabricated organic solar cells. *Results in Materials*, *14*, 100271.

Nabi, G., Ain, Q.-U.-, Tahir, M. B., Nadeem Riaz, K., Iqbal, T., Rafique, M., Hussain, S., Raza, W., Aslam, I., & Rizwan, M. (2022). Green synthesis of TiO_2 nanoparticles using lemon peel extract: Their optical and photocatalytic properties. *International Journal of Environmental Analytical Chemistry*, *102*(2), 434–442.

Nadupalli, S., Repp, S., Weber, S., & Erdem, E. (2021). About defect phenomena in ZnO nanocrystals. *Nanoscale*, *13*(20), 9160–9171.

Pan, J., Chen, J., Huang, Q., Khan, Q., Liu, X., Tao, Z., Zhang, Z., Lei, W., & Nathan, A. (2016). Size Tunable ZnO Nanoparticles To Enhance Electron Injection in Solution Processed QLEDs. *ACS Photonics*, *3*(2), 215–222.

Phan, C. M., & Nguyen, H. M. (2017). Role of Capping Agent in Wet Synthesis of Nanoparticles. *The Journal of Physical Chemistry A*, *121*(17), 3213–3219.

Pieniążek, A., Witkowski, B. S., Reszka, A., Godlewski, M., & Kowalski, B. J. (2016). Optical properties of ZnO microrods grown by a hydrothermal method–a cathodoluminescence study. *Optical Materials Express*, *6*(12), 3741–3750.

Rabell, G. O., Cruz, M. A., & Juárez-Ramírez, I. (2021). Hydrogen production of ZnO and ZnO/Ag films by photocatalysis and photoelectrocatalysis. *Materials Science in Semiconductor Processing*, *134*, 105985.

Radini, I. A., Hasan, N., Malik, M. A., & Khan, Z. (2018). Biosynthesis of iron nanoparticles using Trigonella foenum-graecum seed extract for photocatalytic methyl orange dye degradation and antibacterial applications. *Journal of Photochemistry and Photobiology B: Biology*, *183*, 154–163.

Rai, H., & Kondal, N. (2022). A review on defect related emissions in undoped ZnO nanostructures. *Materials Today: Proceedings*, *48*, 1320–1324.

Rajput, N. (2015). Methods of preparation of nanoparticles-a review. *International Journal of Advances in Engineering & Technology*, *7*(6), 1806.

Ranabhat, K., Patrikeev, L., Revina, A. A., Andrianov, K., Lapshinsky, V., & Sofronova, E. (2016). An introduction to solar cell technology. *Journal of Applied Engineering Science*, *14*(4).

Ranjithkumar, B., Kumar, E. R., Srinivas, M., Ramalingam, H. B., Srinivas, C., Magesh, G., Balamurugan, A., Rahale, C. S., & ChandarShekar, B. (2021).

Evaluation of structural, surface morphological and thermal properties of Ag-doped ZnO nanoparticles for antimicrobial activities. *Physica E: Low-Dimensional Systems and Nanostructures*, *133*, 114801.

Rao, K. G., Ashok, C. H., Rao, K. V., Chakra, C. S., & Tambur, P. (2015). Green synthesis of TiO2 nanoparticles using Aloe vera extract. *Int. J. Adv. Res. Phys. Sci*, *2*(1A), 28–34.

Rodrigues, J., Sedrine, N. B., Correia, M. R., & Monteiro, T. (2020). Photoluminescence investigations of ZnO micro/nanostructures. *Materials Today Chemistry*, *16*, 100243.

Roza, L., Rahman, M. Y. A., Umar, A. A., & Salleh, M. M. (2015). Direct growth of oriented ZnO nanotubes by self-selective etching at lower temperature for photo-electrochemical (PEC) solar cell application. *Journal of Alloys and Compounds*, *618*, 153–158.

Sáenz-Trevizo, A., Amézaga-Madrid, P., Pizá-Ruiz, P., Antúnez-Flores, W., & Miki-Yoshida, M. (2016). Optical band gap estimation of ZnO nanorods. *Materials Research*, *19*, 33–38.

Sagadevan, S., Pal, K., Chowdhury, Z. Z., & Hoque, M. E. (2017). Structural, dielectric and optical investigation of chemically synthesized Ag-doped ZnO nanoparticles composites. *Journal of Sol-Gel Science and Technology*, *83*(2), 394–404.

Samadi, M., Zirak, M., Naseri, A., Khorashadizade, E., & Moshfegh, A. Z. (2016). Recent progress on doped ZnO nanostructures for visible-light photocatalysis. *Thin Solid Films*, *605*, 2–19.

Sampath, S., Bhushan, M., Saxena, V., Pandey, L. M., & Singh, L. R. (2022). Green synthesis of Ag doped ZnO nanoparticles: Study of their structural, optical, thermal and antibacterial properties. *Materials Technology*, *37*(13), 2785–2794.

Sarkar, D., Xie, X., Kang, J., Zhang, H., Liu, W., Navarrete, J., Moskovits, M., & Banerjee, K. (2015). Functionalization of Transition Metal Dichalcogenides with Metallic Nanoparticles: Implications for Doping and Gas-Sensing. *Nano Letters*, *15*(5), 2852–2862.

Saw, K. G., Aznan, N. M., Yam, F. K., Ng, S. S., & Pung, S. Y. (2015). New insights on the burstein-moss shift and band gap narrowing in indium-doped zinc oxide thin films. *PloS One*, *10*(10), e0141180.

Sengupta, D., Das, P., Mondal, B., & Mukherjee, K. (2016). Effects of doping, morphology and film-thickness of photo-anode materials for dye sensitized solar cell application–A review. *Renewable and Sustainable Energy Reviews*, *60*, 356–376.

Sethi, V. K., Pandey, M., & Shukla, M. P. (2011). Use of nanotechnology in solar PV cell. *International Journal of Chemical Engineering and Applications*, *2*(2), 77.

Shaba, E. Y., Jacob, J. O., Tijani, J. O., & Suleiman, M. A. T. (2021). A critical review of synthesis parameters affecting the properties of zinc oxide nanoparticle and its application in wastewater treatment. *Applied Water Science*, *11*(2), 48.

Shafey, A. M. E. (2020). Green synthesis of metal and metal oxide nanoparticles from plant leaf extracts and their applications: A review. *Green Processing and Synthesis*, *9*(1), 304–339.

Shan, G., & Demopoulos, G. P. (2010). Near-Infrared Sunlight Harvesting in Dye-Sensitized Solar Cells Via the Insertion of an Upconverter-TiO_2 Nanocomposite Layer. *Advanced Materials*, *22*(39), 4373–4377.

Sharma, D. K., Shukla, S., Sharma, K. K., & Kumar, V. (2022). A review on ZnO: Fundamental properties and applications. *Materials Today: Proceedings*, *49*, 3028–3035.

Shrestha, S., Wang, B., & Dutta, P. (2020). Nanoparticle processing: Understanding and controlling aggregation. *Advances in Colloid and Interface Science*, *279*, 102162.

Siddique, M., Khan, N. M., Saeed, M., Ali, S., & Shah, Z. (2021). Green synthesis of cobalt oxide nanoparticles using *Citrus medica* leaves extract: Characterization and photo-catalytic activity. *Zeitschrift Für Physikalische Chemie*, *235*(6), 663–681.

Singh, M., Goyal, M., & Devlal, K. (2018). Size and shape effects on the band gap of semiconductor compound nanomaterials. *Journal of Taibah University for Science*, *12*(4), 470–475.

Singh, P., Kumar, R., & Singh, R. K. (2019). Progress on Transition Metal-Doped ZnO Nanoparticles and Its Application. *Industrial & Engineering Chemistry Research*, *58*(37), 17130–17163.

Singh, S., Gade, J. V., Verma, D. K., Elyor, B., & Jain, B. (2024). Exploring ZnO nanoparticles: UV–visible analysis and different size estimation methods. *Optical Materials*, *152*, 115422.

Sinha, A., Qian, J., Moffitt, S. L., Hurst, K., Terwilliger, K., Miller, D. C., Schelhas, L. T., & Hacke, P. (2023). UV-induced degradation of high-efficiency silicon PV modules with different cell architectures. *Progress in Photovoltaics: Research and Applications*, *31*(1), 36–51.

Siva Vijayakumar, T., Karthikeyeni, S., Vasanth, S., Ganesh, A., Bupesh, G., Ramesh, R., Manimegalai, M., & Subramanian, P. (2013). Synthesis of Silver-Doped Zinc Oxide Nanocomposite by Pulse Mode Ultrasonication and Its Characterization Studies. *Journal of Nanoscience*, *2013*, 1–7.

Sivaranjani, K., Priyadharsan, A., Handayani, M., Ansar, S., Dasha Kumar, K., Dharmaraja, J., & Sivakumar, S. (2024). Unveiling solar-powered efficiency for methylene blue photodegradation with Ag-doped CeO2/ZnO nanocomposites. *Journal of Materials Science: Materials in Electronics*, *35*(20), 1417.

Song, T., Gao, F., Guo, S., Zhang, Y., Li, S., You, H., & Du, Y. (2021). A review of the role and mechanism of surfactants in the morphology control of metal nanoparticles. *Nanoscale*, *13*(7), 3895–3910.

Sorbiun, M., Shayegan Mehr, E., Ramazani, A., & Taghavi Fardood, S. (2018). Biosynthesis of Ag, ZnO and bimetallic Ag/ZnO alloy nanoparticles by aqueous extract of oak fruit hull (Jaft) and investigation of photocatalytic activity of ZnO and bimetallic Ag/ZnO for degradation of basic violet 3 dye. *Journal of Materials Science: Materials in Electronics*, *29*(4), 2806–2814.

Sreeju, N., Rufus, A., & Philip, D. (2016). Microwave-assisted rapid synthesis of copper nanoparticles with exceptional stability and their multifaceted applications. *Journal of Molecular Liquids*, *221*, 1008–1021.

Srithar, A., Kannan, J., & Senthil, T. (2017). Preparation and characterization of Ag doped ZnO nanoparticles and its antibacterial applications. *J Adv Chem*, *13*, 6273–6279.

Surib, N. A., Sim, L. C., Leong, K. H., Kuila, A., Saravanan, P., Lo, K. M., Ibrahim, S., Bahnemann, D., & Jang, M. (2017). Ag+, Fe 3+ and Zn 2+-intercalated cadmium (ii)-metal–organic frameworks for enhanced daylight photocatalysis. *RSC Advances*, *7*(81), 51272–51280.

Thabit, H. A., Kabir, N. A., Ismail, A. K., Alraddadi, S., Bafaqeer, A., & Saleh, M. A. (2022). Development of Ag-doped ZnO thin films and thermoluminescence (TLD) characteristics for radiation technology. *Nanomaterials*, *12*(17), 3068.

Tian, W., Yu, W., Shi, J., & Wang, Y. (2017). The property, preparation and application of topological insulators: A review. *Materials*, *10*(7), 814.

Tripathy, S., Rodrigues, J., & Shimpi, N. G. (2023). Top-down and Bottom-up Approaches for Synthesis of Nanoparticles. *Nanobiomaterials Perspect. Med. Appl. Diagn. Treat. Dis*, *145*, 92–130.

Türkyılmaz, Ş. Ş., Güy, N., & Özacar, M. (2017). Photocatalytic efficiencies of Ni, Mn, Fe and Ag doped ZnO nanostructures synthesized by hydrothermal method: The synergistic/antagonistic effect between ZnO and metals. *Journal of Photochemistry and Photobiology A: Chemistry*, *341*, 39–50.

Umar, A., Akhtar, M. S., Al-Hajry, A., Al-Assiri, M. S., Dar, G. N., & Islam, M. S. (2015). Enhanced photocatalytic degradation of harmful dye and phenyl hydrazine chemical sensing using ZnO nanourchins. *Chemical Engineering Journal*, *262*, 588–596.

Ungula, J. (2018). *Formation and characterization of novel nanostructured un-doped and Ga-doped ZnO transparent conducting thin films for photoelectrode* [PhD Thesis, University of the Free State (Qwaqwa Campus)].

Ungula, J., Kiprotich, S., Swart, H. C., & Dejene, B. F. (2022). Investigation on the material properties of ZnO nanorods deposited on Ga-doped ZnO seeded glass substrate: Effects of CBD precursor concentration. *Surface and Interface Analysis*, *54*(10), 1023–1031.

Valiei, A., Lin, N., McKay, G., Nguyen, D., Moraes, C., Hill, R. J., & Tufenkji, N. (2022). Surface Wettability Is a Key Feature in the Mechano-Bactericidal Activity of Nanopillars. *ACS Applied Materials & Interfaces*, *14*(24), 27564–27574.

Van Embden, J., Chesman, A. S. R., & Jasieniak, J. J. (2015). The Heat-Up Synthesis of Colloidal Nanocrystals. *Chemistry of Materials*, *27*(7), 2246–2285.

Van Embden, J., Gross, S., Kittilstved, K. R., & Della Gaspera, E. (2023). Colloidal Approaches to Zinc Oxide Nanocrystals. *Chemical Reviews*, *123*(1), 271–326.

Vishakha, V., Abdel-Mohsen, A. M., Michalicka, J., White, P. B., Lepcio, P., Tinoco Navarro, L. K., & Jančář, J. (2023). Carboxymethyl starch as a reducing and capping agent in the hydrothermal synthesis of selenium nanostructures for use

with three-dimensional-printed hydrogel carriers. *Royal Society Open Science*, *10*(10), 230829.

Wagh, S. S., Jagtap, C. V., Kadam, V. S., Shaikh, S. F., Ubaidullah, M., Bidhan, P., Salunkhe, D. B., & Patil, R. S. (2022). Silver doped ZnO nanoparticles synthesized for photocatalysis application. *ES Energy & Environment*, *17*, 94–105.

Wagner, E. P. (2016). Investigating Bandgap Energies, Materials, and Design of Light-Emitting Diodes. *Journal of Chemical Education*, *93*(7), 1289–1298.

Wang, B., Xue, X., Gong, C., Wang, X., Wang, Q., & Li, J.-G. (2024). The Sr (La1-xTbx) AlO4 (x= 0–1) type layered perovskite: Full substitution of La site, restrained photoluminescence concentration quenching, and novel long afterglow luminescence. *Ceramics International*, *50*(7), 10982–10989.

Wang, C.-C., Shieu, F.-S., & Shih, H. C. (2021). Ag-nanoparticle enhanced photodegradation of ZnO nanostructures: Investigation using photoluminescence and ESR studies. *Journal of Environmental Chemical Engineering*, *9*(1), 104707.

Wang, J. T.-W., Wang, Z., Pathak, S., Zhang, W., deQuilettes, D. W., Wisnivesky-Rocca-Rivarola, F., Huang, J., Nayak, P. K., Patel, J. B., & Yusof, H. A. M. (2016). Efficient perovskite solar cells by metal ion doping. *Energy & Environmental Science*, *9*(9), 2892–2901.

Wang, Z., Lai, L., Zhang, T., Wu, S., Zhao, J., Zhao, Y., Jin, Y., Wang, J., Fan, S., & Li, Q. (2021). Enhanced Visible-Light Absorption and Photocurrent Generation of Three-Dimensional Metal–Dielectric Hybrid-Structured Films. *ACS Applied Energy Materials*, *4*(10), 10542–10552.

Wibowo, A., Marsudi, M. A., Amal, M. I., Ananda, M. B., Stephanie, R., Ardy, H., & Diguna, L. J. (2020). ZnO nanostructured materials for emerging solar cell applications. *RSC Advances*, *10*(70), 42838–42859.

Wu, Y., Chen, Z., Nan, P., Xiong, F., Lin, S., Zhang, X., Chen, Y., Chen, L., Ge, B., & Pei, Y. (2019). Lattice strain advances thermoelectrics. *Joule*, *3*(5), 1276–1288.

Yang, B., Cang, J., Li, Z., & Chen, J. (2024). Nanocrystals as performance-boosting materials for solar cells. *Nanoscale Advances*.

Yıldırım, Ö. A., Unalan, H. E., & Durucan, C. (2013). Highly Efficient Room Temperature Synthesis of Silver-Doped Zinc Oxide (ZnO: Ag) Nanoparticles:

Structural, Optical, and Photocatalytic Properties. *Journal of the American Ceramic Society*, *96*(3), 766–773.

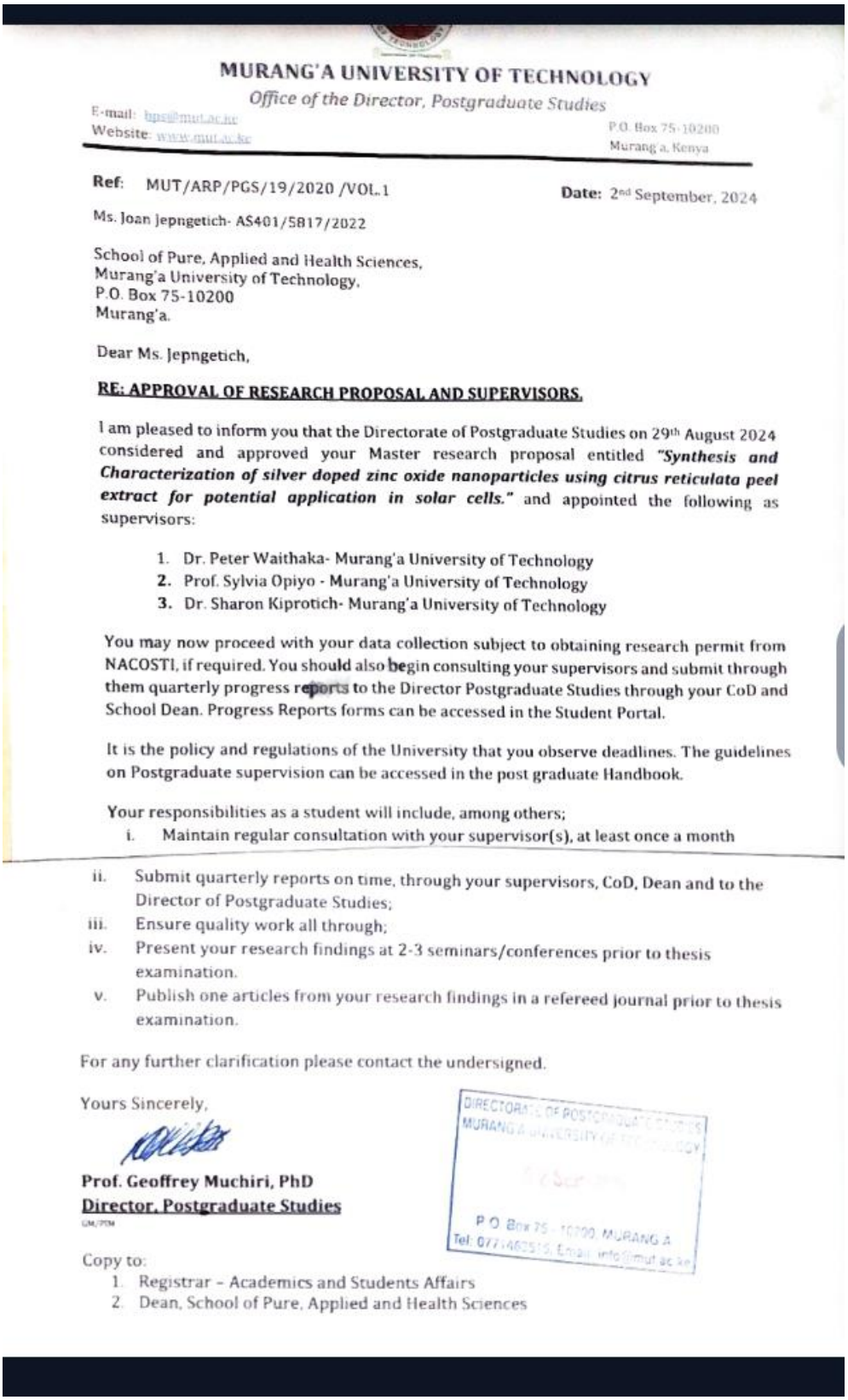
Yoon, Y., Truong, P. L., Lee, D., & Ko, S. H. (2022). Metal-Oxide Nanomaterials Synthesis and Applications in Flexible and Wearable Sensors. *ACS Nanoscience Au*, *2*(2), 64–92.

Zhang, C. (2014). *C*. Arizona State University.

Zhang, X., Qin, J., Hao, R., Wang, L., Shen, X., Yu, R., Limpanart, S., Ma, M., & Liu, R. (2015). Carbon-Doped ZnO Nanostructures: Facile Synthesis and Visible Light Photocatalytic Applications. *The Journal of Physical Chemistry C*, *119*(35), 20544–20554.

APPENDICES

Appendix 1: Research authorization



MURANG'A UNIVERSITY OF TECHNOLOGY

Office of the Director, Postgraduate Studies

E-mail: bpgs@mut.ac.ke
Website: www.mut.ac.ke

P.O. Box 75-10200
Murang'a, Kenya

Ref: MUT/ARP/PGS/19/2020 /VOL.1 **Date:** 2nd September, 2024

Ms. Joan Jepngetich- AS401/5817/2022

School of Pure, Applied and Health Sciences,
Murang'a University of Technology,
P.O. Box 75-10200
Murang'a.

Dear Ms. Jepngetich,

RE: APPROVAL OF RESEARCH PROPOSAL AND SUPERVISORS.

I am pleased to inform you that the Directorate of Postgraduate Studies on 29th August 2024 considered and approved your Master research proposal entitled ***"Synthesis and Characterization of silver doped zinc oxide nanoparticles using citrus reticulata peel extract for potential application in solar cells."*** and appointed the following as supervisors:

1. Dr. Peter Waithaka- Murang'a University of Technology
2. Prof. Sylvia Opiyo - Murang'a University of Technology
3. Dr. Sharon Kiprotich- Murang'a University of Technology

You may now proceed with your data collection subject to obtaining research permit from NACOSTI, if required. You should also begin consulting your supervisors and submit through them quarterly progress reports to the Director Postgraduate Studies through your CoD and School Dean. Progress Reports forms can be accessed in the Student Portal.

It is the policy and regulations of the University that you observe deadlines. The guidelines on Postgraduate supervision can be accessed in the post graduate Handbook.

Your responsibilities as a student will include, among others;

i. Maintain regular consultation with your supervisor(s), at least once a month
ii. Submit quarterly reports on time, through your supervisors, CoD, Dean and to the Director of Postgraduate Studies;
iii. Ensure quality work all through;
iv. Present your research findings at 2-3 seminars/conferences prior to thesis examination.
v. Publish one articles from your research findings in a refereed journal prior to thesis examination.

For any further clarification please contact the undersigned.

Yours Sincerely,

Prof. Geoffrey Muchiri, PhD
Director, Postgraduate Studies

DIRECTORATE OF POSTGRADUATE STUDIES
MURANG'A UNIVERSITY OF TECHNOLOGY
P.O. Box 75 - 10200, MURANG'A
Tel: 0717462515, Email: info@mut.ac.ke

Copy to:

1. Registrar – Academics and Students Affairs
2. Dean, School of Pure, Applied and Health Sciences

Appendix 2: Publications

The following papers have been published from this thesis.

Jepngetich, J., Njoroge, P. W., Opiyo, S., & Kiprotich, S. (2025). Effects of Ag Doping Concentrations on Structural and Optical Properties of Citrus Reticulata Capped ZnO Nanoparticles. *Journal of Nanosciences Research & Reports. SRC/JNSRR-207. J NanoSci Res Rep*, *7*(2), 2-7.

Jepngetich, J., Njoroge, P. W., Opiyo, S., & Kiprotich, S. (2025). Synthesis and characterization of Ag-ZnO using citrus reticulata peel extract. *Materials Research Express*, *12*(5), 055003.